Telescope Performance

A. Armada, O. Blanch, J. Cortina, F. Goebel, P. Majumdar,
M. Mariotti, D. Paneque, R. Paoletti, N. Turini

MAGIC TDAS 06-04

April 25, 2006

Contents

Chapter 1

Signal Propagation

Here we review how the PMT pulse propagates through the electronics all the way from the photocathode to the digitizers (Flash ADCs or FADC). We will extract the average conversion factors in the electronic chain.

1.1 Description of the readout

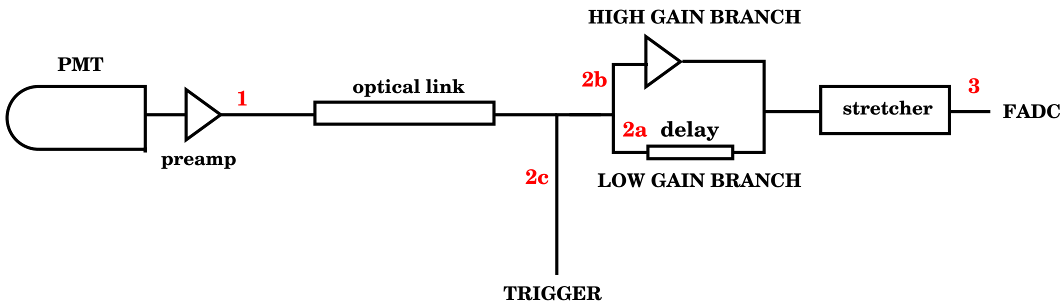

Figure 1.1: *Sketch of the telescope data readout chain.*

An overview of the readout electronic chain can be found in Fig. 1.1 The PMT electrical pulse that is generated at the PMT is amplified at the PMT base ("preamplifier") inside the telescope camera. The analog signal is transmitted over 162 m long optical fibers using Vertical Cavity Surface Emitting Laser drivers (VCSELs, 850 nm wavelength [10]). The signal is converted back into an electrical pulse in the control house and then duplicated. One part goes into a discriminator that generates a digital signal for the trigger, whereas a second one is again duplicated and sent to two branches. A first branch ("high gain", HG) is further amplified and a second branch ("low gain", LG) is delayed by 50 ns. If the signal exceeds a preset threshold the low gain signal is combined with the high gain signal using a GaAs fast switch. The combined signal is stretched to ~6 ns

FWHM and digitized by a FADC at 300 MHz sampling rate. More details can be found in reference [3].

For all the tests in this chapter we used a reference pulse of fixed amplitude and charge that was produced using the so-called “Pulpo generator” in the control house[3]. This pulse is split in 8 equal pulses that are sent over 8 independent optical fibers to the receiver boards. These reference Pulpo pulses have a FWHM that is similar to that of the pulses generated at the camera PMTs by Cherenkov pulses. The optical fibers are much shorter than 160 m but according to [10] their effect in the signal propagation should be practically independent of the fiber length.

We used a Tektronix 500 MSample/s (readout through GPIB) oscilloscope to measure the electrical pulse right before the optical transmission (point 1 in figure 1.1), after the optical link and before duplicating the trigger signal (point 2a, equivalent to points 2b and 2c), at the input of the FADCs (point 3). We finally compared these measurements with the signals that are digitized with the FADCs. Please note that the oscilloscope sampling rate was limited to 500 MS/s: this sampling rate is too low for the signal before the stretcher and biases the measurement of the pulse amplitude.

1.2 Signal at transmitter

The pulse at the output of the Pulpo generator and input of the optical transmission line (point 1 in figure 1.1) has the following features, that are common to all the output channels:

$$\begin{gathered}\text{Area} = 116 \pm 1\ \text{mV}\cdot\text{ns}\\ \text{Amplitude} = 28.59 \pm 0.01\ \text{mV}\\ \text{FWHM} = 2.704 \pm 0.001\ \text{ns}\\ \text{Rise Time} = 1.518 \pm 0.001\ \text{ns}\end{gathered}$$

1.3 Signal at receiver

Next we measured the signal at the eight LEMO outputs of the test receiver board. This corresponds to point 2 in the sketch of figure 1.1. Note that this is the signal that goes to the trigger discriminators. Only the test board was suitable for this test because it is the only one that is equipped with LEMO output connectors that probe the line before the trigger splitter. It is noteworthy that the eight channels are completely independent, that is, they have different VCSELs, fibers and receivers. This measurement suffers from the strongest uncertainty in this section: the pulse fluctuates strongly from channel to channel because the test board simply malfunctions for some channels.

AREA (Vs)	AMPLITUDE (V)	FWHM (s)	Rise Time (s)
-2.85203e-11 ± 3.6e-13	0.0139955 ± 0.00023	2.64695e-09 ± 2.9e-11	1.4954e-09 ± 2.6e-11
-1.23522e-10 ± 1.2e-12	0.0072304 ± 0.00016	2.94402e-09 ± 5.7e-11	2.2309e-09 ± 8.8e-11
-6.59612e-11 ± 5.5e-13	0.021806 ± 0.00027	2.87298e-09 ± 2.8e-11	1.98945e-09 ± 5.9e-11
-1.68137e-10 ± 1.3e-12	0.0241274 ± 0.00030	2.8957e-09 ± 3.2e-11	2.20273e-09 ± 6.9e-11
-7.19130e-11 ± 4.6e-13	0.022734 ± 0.00025	2.92642e-09 ± 2.9e-11	2.36388e-09 ± 7.2e-11
-1.72092e-10 ± 1.4e-12	0.024278 ± 0.00032	2.82314e-09 ± 3.0e-11	1.87258e-09 ± 5.4e-11
-9.56244e-12 ± 2.7e-13	0.00414922 ± 0.00013	2.33726e-09 ± 1.0e-10	1.26808e-09 ± 6.2e-11
-1.64835e-10 ± 1.0e-12	0.018506 ± 0.00024	2.87022e-09 ± 3.1e-11	2.22352e-09 ± 7.5e-11

Table 1.1: *Pulse area, amplitude, FWHM and rise time at the input of the receiver board (point 2), for the eight channels of the test receiver board.*

The results of these measurements can be found in table 1.1. There is a strong dispersion in pulse area and amplitude. The average of the eight channels would be:

$$\begin{gathered}\text{Area} = 100 \text{ mV} \cdot \text{ns} \\ \text{Amplitude} = 16 \text{ mV} \\ \text{FWHM} = 2.8 \text{ ns} \\ \text{Rise Time} = 1.95 \text{ ns}\end{gathered}$$

It is puzzling that, compared to the measurement at the input of the optical transmission line, the area and the FWHM stay practically constant, whereas the amplitude is smaller by almost a factor 2. This reduction in amplitude is not compatible with the previous detailed study in [10], where it is stated that the pulse suffers practically no deformation in the optical transmission. As we said above the test board is not completely trustworthy: it may be that some of the channels are simply faulty.

Lastly we calculated the ratio between the charge and the amplitude of the pulses at point 1 and 2 for all eight channels of the receiver board.

Table 1.2 shows the results. The average ratio of points 1 and 2 is 0.74 for the charges and 0.6 for the amplitudes. This is to say that the integrated charge reduces in the optical transmission by about 25%.

1.4 Signal at the FADC input

The next step was to measure the pulse after the HG amplifier and the stretcher: at the LVDS output of the optical receivers, which is also the input of the FADCs. It is labelled point 3 in figure 1.1. The measurement was done for one of the receiver boards that is routinely used in data taking (receiver board 37). One of the eight channels is defective and will not be considered in this measurement.

The measurements can be found in table 1.3. The average of the seven working channels in board 37 would be:

AREA	AMPLITUDE
0.245865 ± 0.00378794	0.489524 ± 0.00817741
1.06471 ± 0.0135989	0.252936 ± 0.00564767
0.568631 ± 0.00682375	0.762714 ± 0.00933477
1.45739 ± 0.0154654	0.847251 ± 0.00976588
0.619583 ± 0.00667432	0.79581 ± 0.00875808
1.47828 ± 0.0188065	0.848538 ± 0.0114557
0.0823713 ± 0.0024985	0.143257 ± 0.00476662
1.42097 ± 0.0151886	0.647513 ± 0.00867679

Table 1.2: *Ratio of area and amplitude of the pulse before the optical link (point 1) and at the input of the receiver board (point 2), for the eight channels of the test receiver board.*

AREA (Vs)	AMPLITUDE (V)	FWHM (s)	Rise Time (s)
2.49551e-09 ± 3.6e-12	0.509447 ± 0.00059	4.95478e-09 ± 5.9e-12	2.7624e-09 ± 4.3e-12
3.779e-09 ± 2.0e-11	0.520617 ± 0.0026	5.98706e-09 ± 3.1e-11	3.13761e-09 ± 1.7e-11
4.10648e-09 ± 7.9e-12	0.558789 ± 0.0010	FAILED	FAILED
3.93194e-09 ± 2.1e-11	0.512975 ± 0.0027	6.36542e-09 ± 3.2e-11	3.21836e-09 ± 1.7e-11
3.51632e-09 ± 1.8e-11	0.496896 ± 0.0025	5.81796e-09 ± 3.0e-11	2.96796e-09 ± 1.7e-11
DEFECTIVE	DEFECTIVE	DEFECTIVE	DEFECTIVE
3.42875e-09 ± 9.1e-11	0.492 ± 0.0088	5.91731e-09 ± 5.0e-11	2.9292e-09 ± 1.8e-11
3.74685e-09 ± 1.9e-11	0.522149 ± 0.0026	5.54124e-09 ± 2.8e-11	2.91498e-09 ± 1.6e-11

Table 1.3: *Pulse area, amplitude, FWHM and rise time after the HG amplifier (point 3) for the eight channels of the receiver board 37. Channel 6 is defective*

$$\begin{gathered}\text{Area} = 3560\ \text{mV} \cdot \text{ns}\\ \text{Amplitude} = 515\ \text{mV}\\ \text{FWHM} = 5.6\ \text{ns}\\ \text{Rise Time} = 2.98\ \text{ns}\end{gathered}$$

The pulse has been amplified by a factor ~30 (see below for a more detailed comparison) and stretched to ~6 ns. This fits the input voltage range and sampling rate of the digitizers.

We calculated the ratio of charge and amplitude at point 3 and 1 for all channels independently.

Table 1.4 shows the results. The dispersion is not as large as for the last measurements. The average ratio of points 3 and 1 is 30.8 for the charges and 18.0 for the amplitudes.

1.5 Digitized signal

We finally measured the ratio of the charge and amplitude of the pulse after the high gain amplifier and digitized at the FADCs, again for receiver board 37. The

AREA	AMPLITUDE
21.513 ± 0.18	17.8191 ± 0.021
32.5776 ± 0.33	18.2098 ± 0.094
35.4007 ± 0.31	19.5449 ± 0.037
33.896 ± 0.34	17.9425 ± 0.097
30.3131 ± 0.30	17.3801 ± 0.089
DEFECTIVE	DEFECTIVE
29.5582 ± 0.83	17.2088 ± 0.30
32.3004 ± 0.32	18.2633 ± 0.094

Table 1.4: *Ratio of area and amplitude of the pulse after the high amplification (point 3) and before the optical link (point 1) for seven channels in receiver board 37.*

signal in the FADCs was extracted by integrating in a 14-slice time window.

AREA	AMPLITUDE
12.35 ±0.26	4.78 ±0.47
13.56 ±0.42	4.07 ±0.35
14.69 ±0.5	4.24 ±0.38
13.38 ±0.6	3.82 ±0.35
13.13 ±0.37	4.16 ±0.81
14.81 ±0.4	4.47 ±0.89
13.17 ±0.48	3.52 ±0.92
14.23 ±0.55	4.14 ±0.42

Table 1.5: *Ratio of area and amplitude of the pulse after the high gain amplification (point 3) and digitized at the FADCs for all eight channels in receiver board 37. The units are respectively mV·ns divided by integrated charge FADC counts and mV divided by charge amplitude FADC counts.*

The results are quite constant over the channels. The average ratio is 13.7 mV·ns /FADC count for the charge and 4.15 mV/FADC count for the amplitude. That is, for the average pulse that we have been considering along this chapter, we have an integrated charge of 259 FADC counts and an amplitude of 124 FADC counts. The charge can be converted into photoelectrons using the conversion factor that is typical for the inner pixels and the fixed window 14-slice charge extractor (7.8 FADC counts/phe, adopted from [7] and used throughout this document). The Pulpo pulse that we consider here would typically correspond to 33 phe.

The same test was repeated for receiver board 31 with similar results (except for two channels that were probably faulty).

1.6 Summary

In the table below we summarize the results that we have obtained for an average pulse.

	AREA	AMPLITUDE	FWHM
Input optical link	116 mV·ns	29 mV	2.7 ns
Output optical link (lemo)	100 mV·ns	16 mV	2.8 ns
HG FADCs	3560 mV·ns	515 mV	5.6 ns
HG FADCs	259 FADC counts	124 FADC counts	-
HG FADCs	33 phe	-	-

Table 1.6: *Area, amplitude and width of the signal as it propagates thorugh the different stages of the electronic chain: at the input of the optical transmission line, at the output of the transmission line, at the input of the FADC (high gain branch) as measured by the oscilloscope in mV·ns, as measured by the FADC in digital counts and converted into phe using the standard conversion factor.*

The amplification between the output of the optical link and the input of the FADC is a factor 36 in charge. We know from the digitized signals that the ratio between the HG and LG signals is a factor 10. The remaining amplification factor is common to both branches and comes from the stretcher.

According to the summary table one photoelectron would have an amplitude of 0.5 mV at the output of the optical transmission line and at the trigger input. This is not what we assume at the MC. The measurement at the output of the optical line (lemo connectors) may be however not reliable.

Chapter 2

PMT Response

In this chapter we will try to evaluate the response of the camera photomultipliers to different levels of light for different high voltages. Next we will study the accuracy of our flatfielding and how this accuracy evolves with time.

The inner camera is composed by 396 0.1° FOV hemispherical photomultipliers of 1 inch diameter (Electron Tubes 9116A[12]) surrounded by 180 0.2° FOV PMTs of 1.5 inch diameter (ET 9116B). Each PMT is connected to an ultrafast low-noise transimpedance pre-amplifier. The 6-dynode high voltage system is stabilized with an active load. The photocathode quantum efficiency is enhanced up to 30% and extended to the UV by a special coating of the surface using wavelength shifter [9].

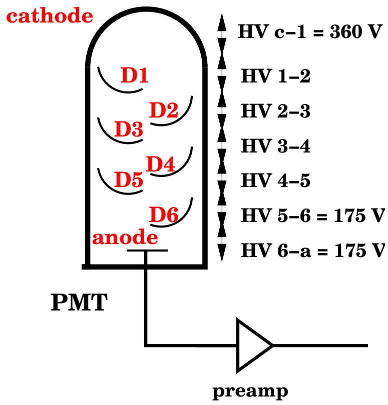

Figure 2.1: *Scheme of the HV distribution system in the PMT. D1 to D6 are the six dynodes. HV_{c-1} is the cathode to first dynode voltage, HV_{1-2} the first to second dynode voltage, etc, and HV_{6-a} is the sixth dynode to anode voltage.*

Figure 2.1 is a scheme of the HV distribution system in the PMT.

The first five amplification stages (HV_{c-1}, HV_{1-2}... HV_{4-5}) are powered through the main power supply. In fact HV_{c-1} is fixed to 360 V using a zener diode, and HV_{1-2}, HV_{2-3}, HV_{3-4} and HV_{4-5} are all equal and can be regulated individually for each pixel.

The voltage drop between D5 and the anode (HV_{5-6}+HV_{6-a}) is fixed actively using the so-called “active load” to ∼350 V.

The voltage drop between D6 and the anode is set with an independent power supply (HV175) to ∼175 V.

Both the active load and the 175V power supply are actually implemented as two hardware units that deliver power to only one side of the camera. Side A corresponds to sectors 1, 2 and 6, while side B corresponds to sectors 3, 4 and 5. Both sectors include inner and outer pixels.

In summary, the voltage drop in the four stages HV_{1-2} to HV_{4-5} is:

$$\begin{aligned} HV_{1-2} = \; HV_{2-3} = \; HV_{3-4} = \; HV_{4-5} \\ = \frac{HV_{applied} \; -HV_{c-1} \; -HV_{5-6}-HV_{6-a}}{4} \\ = \frac{HV_{applied} \; -710 \; V}{4} \end{aligned}$$

where $HV_{applied}$ is the high voltage that is applied to the PMT and can be regulated pixel by pixel from the camera control system.

The signal is amplified right after the PMT and sent over an optical transmission line to the control house as described in chapter 1.

At the end of this chapter figure 2.11 shows the schematics for the HV distribution system and figure 2.12 the schematics for the preamplifier.

2.1 Quantum efficiencies of the PMTs

The quantum efficiency (QE) of the PMTs was measured by the company and delivered in the usual manner, that is, in the so-called “passports” of the PMTs. The company measures the QE using two reference filters, a first one which transmits wavelengths longer than 650 nm and second one which peaks around 400 nm. The average QE at those reference wavelength bands are known respectively as “corning red” and “corning blue”[2].

Figure 2.2 shows the corning blue and corning red for all the pixels. There is a slow decrease of corning blue with pixel number in the inner pixels (by about 30%) up to pixel 332 (the first pixel in the outermost inner ring), and then this parameter stays constant in the outer pixels. The trend for the inner pixels is not surprising because they were assigned positions in the camera according to their corning blue. The higher the corning blue, the closer they were installed to the camera center, in order to maximize the sensitivity of the innermost part of the camera were most of the lowest energy showers (that is, those with the smallest charge) are expected. It must be noted that the outer PMTs show a much larger dispersion than the inner, about 10% relative RMS around an average value of 11% corning blue.

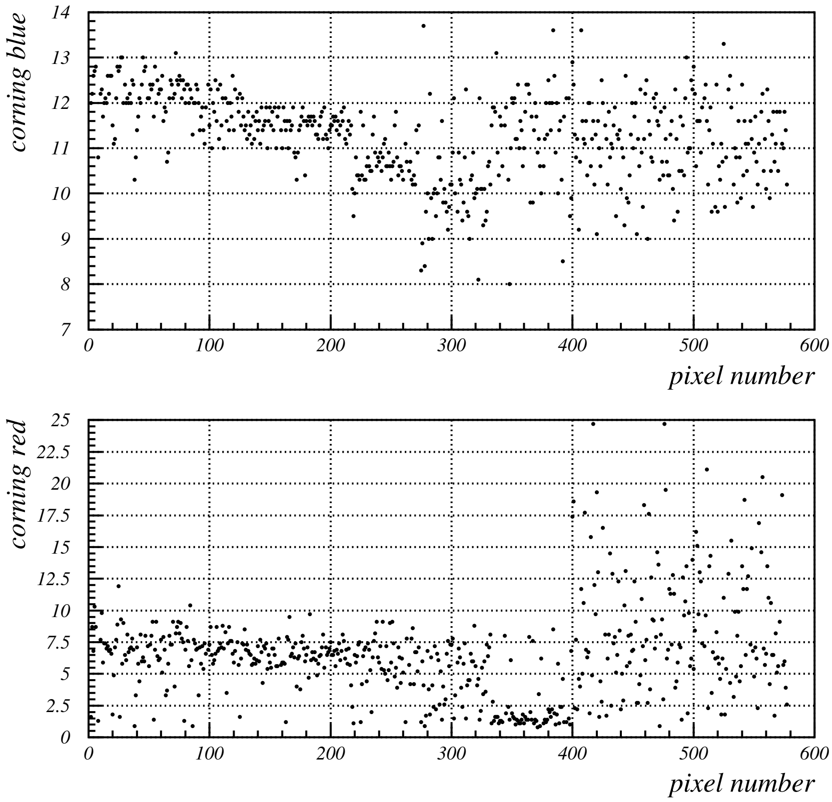

Figure 2.2: *Corning blue (top panel) and corning red (bottom) in percentage of all the pixels in the telescope camera.*

The corning red follows a different trend. It is around 7% for the innermost pixels and hardly depends on pixel number up to pixel ∼332 where it drops to less than 2.5%. Then it grows again in the outer pixels to about 7.5% average corning red but again with strong fluctuations. The corning red drops starting on the inner pixel 332 because the PMTs were delivered in two bunches by the company and the manufacturing process was different for the first and the second bunch.

Figure 2.3 displays the ratio of corning blue and corning red for all the pixels in the camera. Three populations are obvious, as could be expected from the discussion above:

- The inner pixels except the last ring (332-397), where the ratio is about 2.
- The inner pixels in the last ring, where the ratio jumps to about 10. These pixels are far more sensitive in the blue than in the red, i.e., there is a faster drop in the curve of QE between blue and red wavelengths.

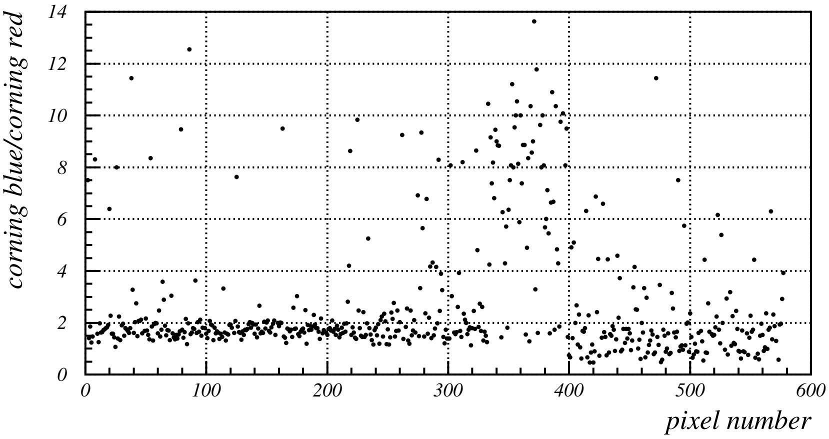

Figure 2.3: *Ratio of corning blue and corning red for all the pixels.*

- The ratio drops again to about 1.5 for the outer pixels, again with a larger dispersion.

The distribution of corning blue and red in the camera has consequences for the flatfielding. In general pixels with a lower corning blue will have to be compensated with a higher amplification gain, that is, a higher HV. Given the difference in ratio of corning blue and red we can also conclude that the choice of color for the calibration pulses that are used to flatfield the camera is critical: if we choose green instead of blue or UV, we will be more sensitive to the two bunches of PMTs. Green is anyway not recommendable since the maximum of the Cherenkov spectrum at ground level peaks at near UV-blue wavelengths.

We can also expect a small effect of the two different populations of inner pixels in the distribution of pedestal RMS. This is because the pedestal RMS is dominated by NSB that grows towards red wavelengths, so PMTs with higher red sensitivity are expected to have a larger DC and pedestal RMS.

2.2 Dependence of pulse charge on PMT HV

The gain in each of the stages of the PMT is proportional to the voltage drop to the power of a correction factor α that depends on the PMT and may vary between 0.7 and 0.9 (see [11] for more details). The gain of the total system G_{PMT} is a product of the gains in all the stages:

$$G_{PMT} \propto HV_{c-1}^{\alpha} \cdot HV_{5-6}^{\alpha} \cdot HV_{6-a}^{\alpha} \cdot \left(\frac{HV_{applied} - 710\ V}{4}\right)^{4 \cdot \alpha} \tag{2.1}$$

The first three voltages are fixed so we can conclude that:

$$G_{PMT} \propto (\frac{HV_{applied} \ - 710\ V}{4})^{4 \cdot \alpha} \tag{2.2}$$

It must be noted that the proportionality factor depends on the individual photomultiplier (page 1-12 of [11]).

Let us check if the total gain behaves as expected. We have performed a calibration run with the "CT1 pulser box" (a special calibration box with UV LEDs) of a fixed light intensity for each of a range of fixed pixel HV: all pixels set to 1000, 1100, 1200, 1300 and 1350 V. The data were taken on 2004_11_11 and the corresponding runs numbers are 43910-43922. The pulses were digitized in the FADCs as usual and the charge was then extracted by integration of the first 12 high gain amples.

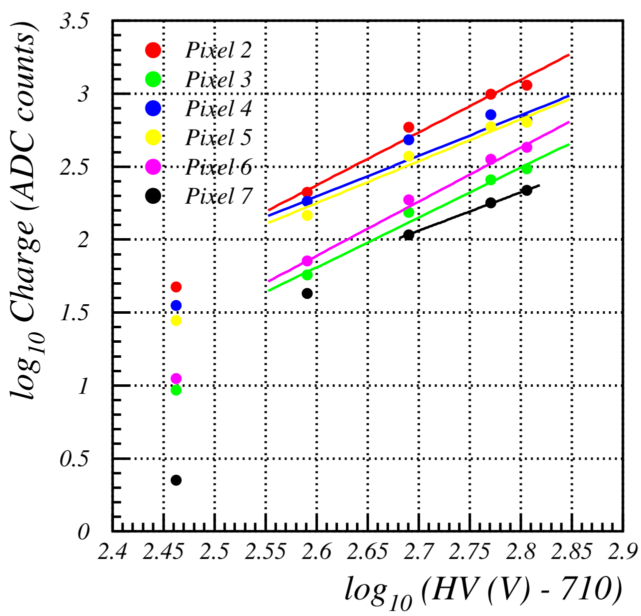

Figure 2.4: *Average charge in a calibration run (log) as a function of the HV minus 710 V (log) that has been applied on the PMTs for the innermost six pixels. The points have been fitted to a straight line.*

Figure 2.4 shows the logarithm of the mean charge in the calibration runs as a function of the logarithm of $HV_{applied}$-710 V for pixels 2 to 7 (hardware numbering). The dependence is only roughly linear: the points seem to slowly curve down and saturate for 1350 V. We have fitted the points individually for each pixel to a straight line. Only mean charges above 50 ADC counts were included in the fit (this number was rather arbitrary and meant to exclude not very well defined pulses). The resulting slopes are close to 3.2, as expected from equation 2.2 if we assume $\alpha \sim 0.8$. Note that the charge has been measured at the end of the electronic chain and the different channels may have different gains in the optical transmission system, in the high gain amplifier or in the stretcher (see chapter 6 for a detailed study of the variations of the total gain).

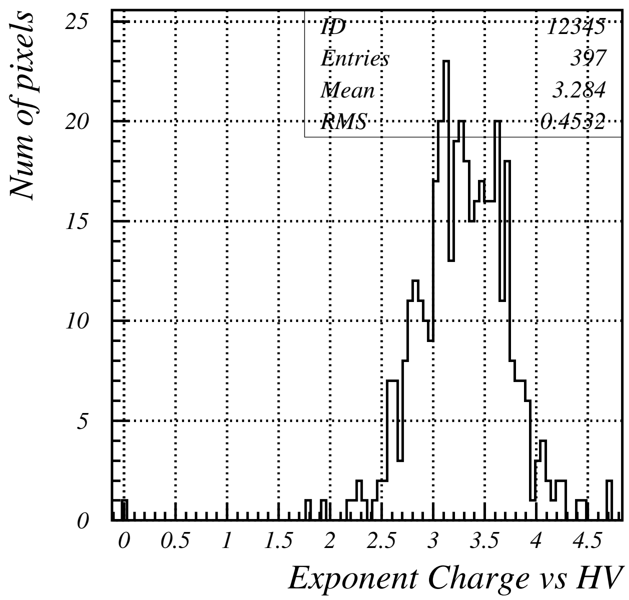

Figure 2.5: *Distribution of the fitted exponent in the charge vs voltage dependence only for pixels in the inner camera.*

The fit that is illustrated in figure 2.4 has been performed systematically for all pixels in the inner camera. The slope of the straight line, which is also the exponent of the power law in equation 2.2, follows the distribution that is displayed in figure 2.5. The mean of the distribution is 3.3, not far from the expected value 3.2. This number is however rather arbitrary since we have imposed an arbitrary cut on the mean charge. By changing this cut we can obtain slopes ranging between 3 and 4.

2.3 Camera flatfielding

In an ideal system the gain of all the camera channels is equal, what is to say that the digitized signal is the same for all pixels when they are flashed with the same light pulse. In a real system the gains are slightly different and must be corrected through calibration. We would anyway like to equalize the gains for two main reasons: (a) we would like all channels to have the same dynamic range in the digitizers and (b) the discriminator threshold levels are normally set at the same voltage level for all channels.

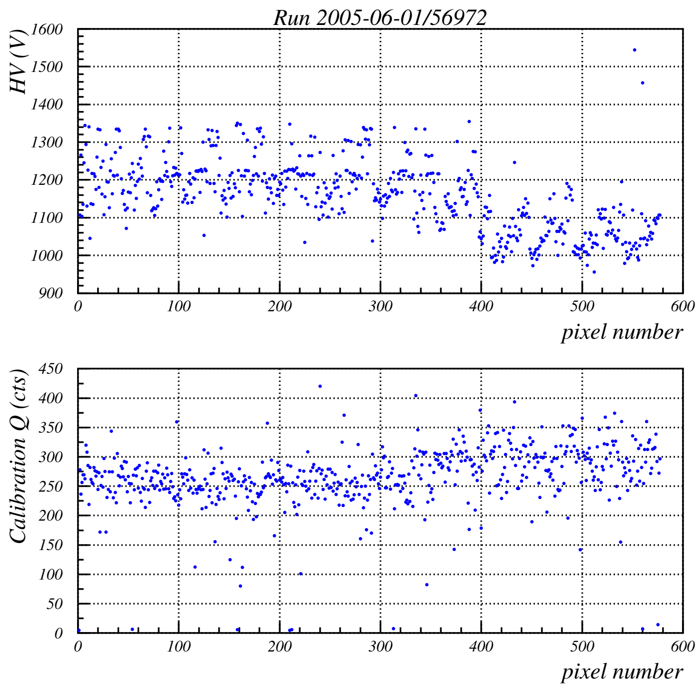

Figure 2.6: *HV (top) and mean calibration charge of a data run with interleaved 10LedUV calibration events (bottom) for all the pixels in the camera. The data run is 56972 (2005_06_01).*

The total gain in a channel is a product of the PMT quantum and collection efficiency, the gain of the PMT dynode system, the preamplifier, the optical transmission system, the different elements in the optical receivers and the FADC.

The hardware flatfielding of the gains is an iterative procedure. It proceeds as follows:

- We take a calibration run. The wavelength of the calibration light must be as close as possible to the wavelength where Cherenkov pulses generate most of the photoelectrons in our PMTs, that is, we will typically use UV pulses.

- We analyze the calibration run and extract the mean charge over the whole run for all the pixels. We also calculate the mean of all the pixel means ("camera mean").
- We increase the HV for pixels that show a mean charge below the camera mean. We decrease that of pixels with a mean charge above the camera mean. The new HV is estimated using equation 2.2.

And then we iterate up to the point when all the charges in the camera are equal roughly within a 5% RMS.

The second panel of figure 2.6 shows the status of the camera in June 2005, several months after the last flatfielding. The charge distribution in the inner camera has a dispersion of about 10%, that is, wider than the ideal one after a flatfielding. The outer pixels display an even wider distribution and their mean is also 20% above the mean of the inner camera. There is also a slight increase of the charge starting on pixel 332. These systematic shifts are most probably due to the fact that this calibration events were taken with UV light while the latest flatfielding was made with a combination of several colors that also involved longer wavelengths and we know that the ratio of corning blue and red (i.e. the ratio of QE at short and long wavelengths, see section 2.1) is different for the three population of pixels.

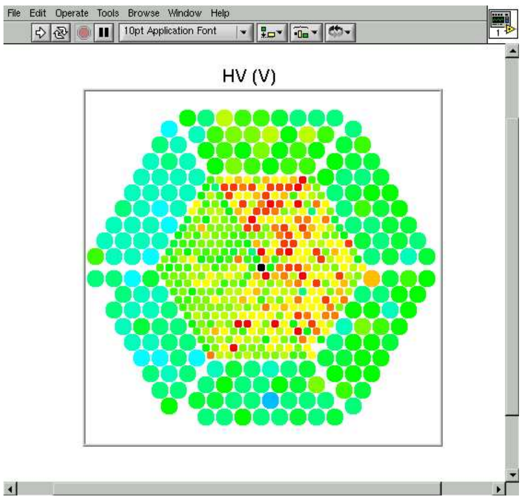

Figure 2.7: *Distribution of HV in the camera for data run 56972 (2005_06_01). The HV linearly ranges from 850 V (blue) to 1350 V (red).*

The same figure also shows how the pixel HV depends on the pixel number. The HV that is applied to the inner pixel is substantially higher than that applied to the outer pixels : in average 1200 V compared to 1050 for the outer pixels or ∼15%. This is simply because the outer PMTs collect more light and generate more charge at the anode for the same light flux density. If we want the charge and not the light density to be equal in the whole camera, we must reduce the amplification by a factor that is roughly the ratio of the angular size of both kind of pixels.

Apart from this general difference, the dispersion of HV is about 50 V or 5% RMS. According to equation 2.2, this corresponds to a dispersion of the PMT amplification gain of approximately 30%. It is noteworthy that the HV are not distributed in the camera randomly in the camera. This is obvious in figure 2.7 where we can see that the right side of the camera (sectors 1, 2 and 6) has systematically a HV that is higher than the left side, both for the inner and the outer pixels. THe shift is in the average 50 V or 5%.

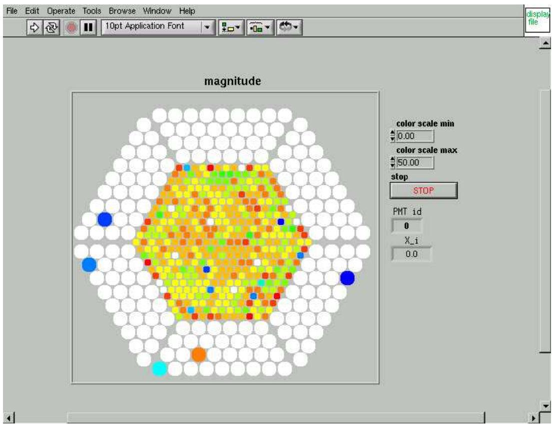

Figure 2.8: *Distribution of number of phe in calibration events for data run 56972 (2005_06_01). The number or phe linearly ranges from 0 (blue) to 50 (red). The outer camera is saturated in this scale.*

This is hard to understand on account of the different QEs, because the corning blue decreases with the distance to the camera center (see figure 2.2). The pixel QE can also be estimated through the number of photoelectrons in calibration events for which each pixel is illuminated with the same light flux. Figure 2.8 shows the average number of phe that are measured (using the F-Factor method) in the inner pixels for interleaved 10LedUV calibration events in run 56972. There is no systematic difference between both sides of the camera. This contradicts the hypothesis that pixels in the right side of the camera have an increased HV to compensate for a systematically lower QE.

The top panel of figure 2.9 shows again the number of photoelectrons but this time as a function of the pixel number. There is no strong dependence with the distance to the center. The number of phe only increases slightly for the last ring of the inner pixels.

A further possibility are the optical links but they were also selected so that the gain drops with distance to the center. Another parameter that could differ for the two sides is the HV of the active load or the 175V power supply that are used for the last two stages of the PMTs. As we shall see in chapter 6 (figure

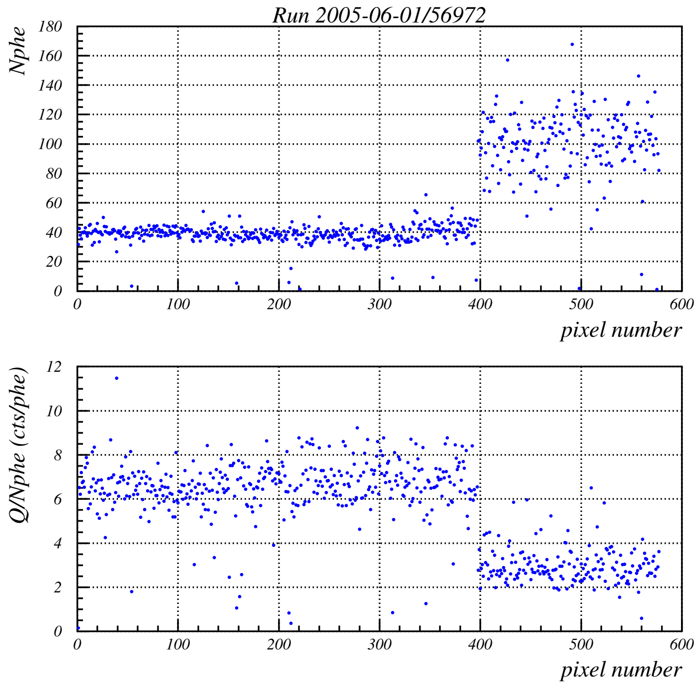

Figure 2.9: *Number of phe in calibration events (top) and conversion factor from number of photoelectrons to ADC counts for data run 56972 (2005_06_01) as a function of the pixel number.*

6.13) the HV that is set for both sides systematically differs in about 7-8 V. This is however too small to explain the disagreement in the pixel HV.

The most probable factor behind the distribution of HV in the camera is the fact that different PMTs have different amplification gains for the same HV (2.2). The amplification of the PMTs in the camera for a fixed HV were measured at IFAE and those with the highest amplification were installed in sector 3; the second best bunch of PMTs was installed in sector 4; the next in sector 5 and so forth[6].

2.4 Dependence of pulse arrival time on PMT HV

When we increase the pixel HV, we increase the voltage drop in four of the six dynodes. An increased voltage means that electrons suffer from a larger acceleration and it takes them shorter to move from dynode to dynode. The final results is that the pulse gets narrower and arrives faster at the anode.

We can check for this effect by looking at the arrival time of the calibration pulses. The trigger time for this kind of pulses is fixed, so we expect the pulses to move in the FADC window with HV. We actually do not need to change the pixel HV to check this effect, since the pixels in the camera are set to very different voltages, so we can check how the arrival time depends on the pixel number and then look for a correlation with its HV.

For this analysis we have used the interleaved calibration events in data run 54547 (2005_05_04). For each event and each pixel the arrival time is calculated using the “sliding window” signal extractor. We have finally calculated for each pixel the average of the arrival times over all the events in the run. Actually the whole procedure is implemented in the DAQ program and we rely on the data summary that this program outputs at the end of each run.

The top panel of figure 2.10 shows the HV that is applied to each pixel of the camera. The well known difference between inner and outer pixels is evident in this plot. The central panel shows the average arrival time as a function of the pixel number. Inner and outer pixels also differ strongly. The bottom panel displays the arrival time versus the pixel HV. There is a clear correlation. The arrival time behaves as expected, that is, the pulse arrives earlier for a larger voltage. The effect is however not huge: about one FADC time slice for the whole range of pixel HV, that extends from 950 to 1350 V. The discrepancy of arrival times between inner and outer pixels can be easily explained by their different HVs.

2.5 Schematics

In the figure below are the schematics of several of the camera electronic components. These and many other schematics can be found in acrobat PDF format in the web address:
http://atlas.ifae.es/∼cortina/performance/Camera_Drawings_PDF/

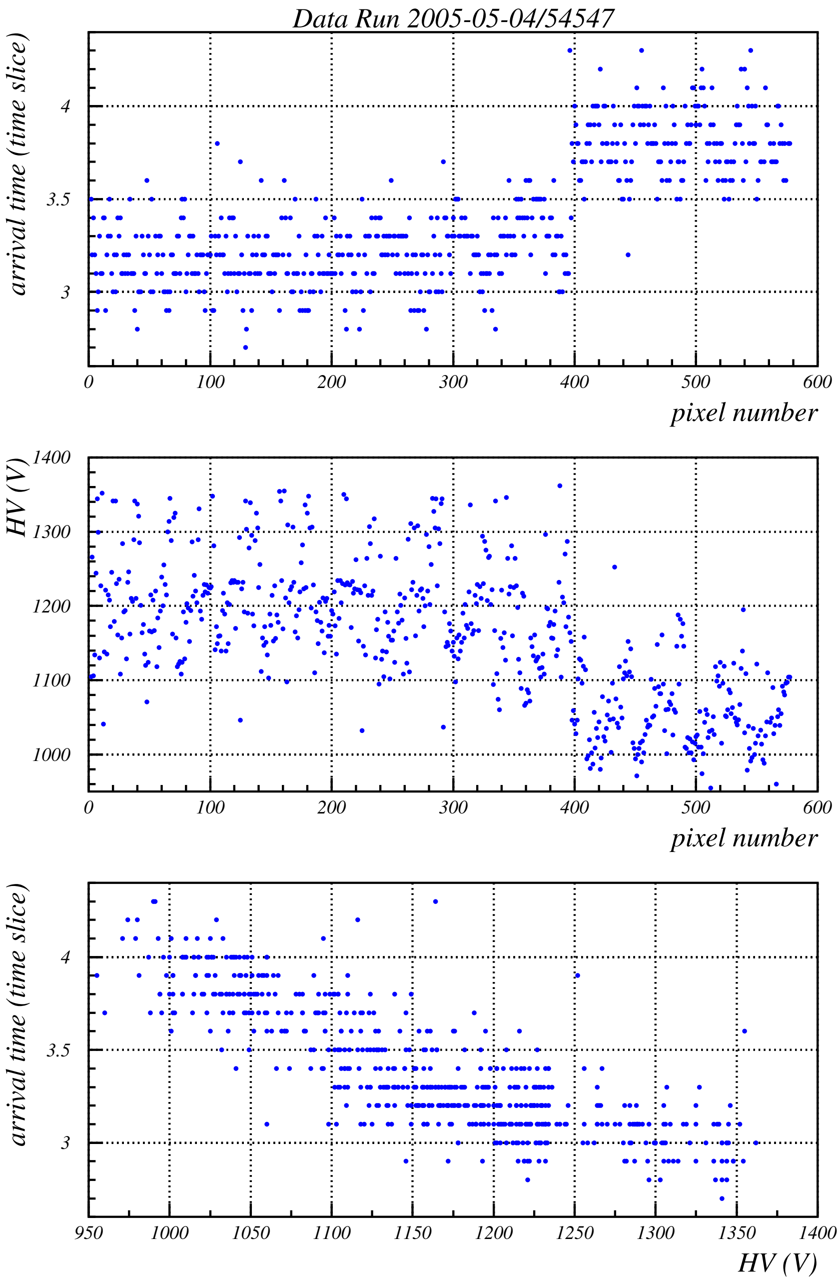

Figure 2.10: *Arrival time of interleaved calibration pulses (top) and pixel HV (center) as a function of pixel number. Bottom: arrival time as a function of the HV.*

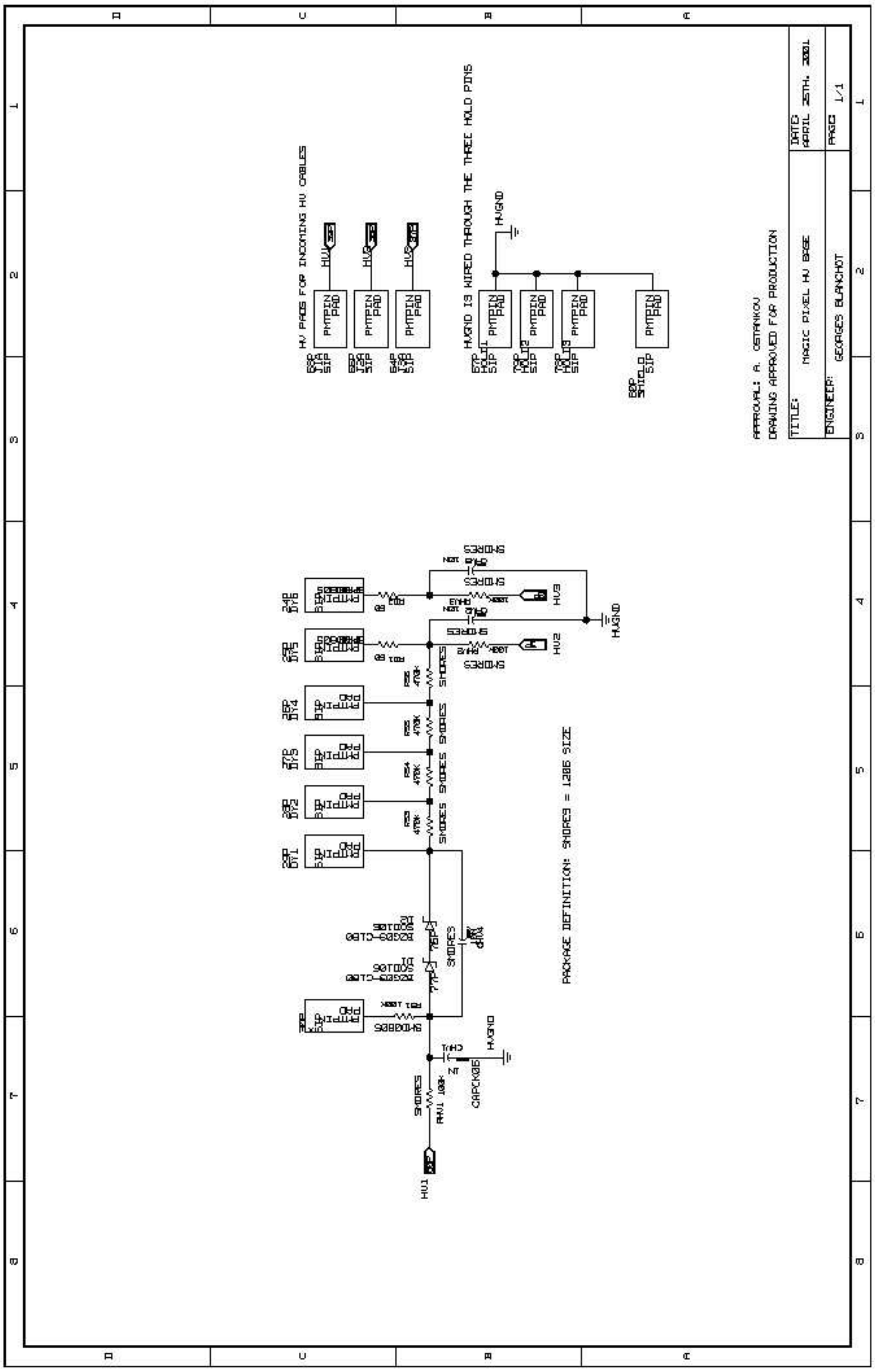

Figure 2.11: *Schematics of the HV distribution at the PMT base.*

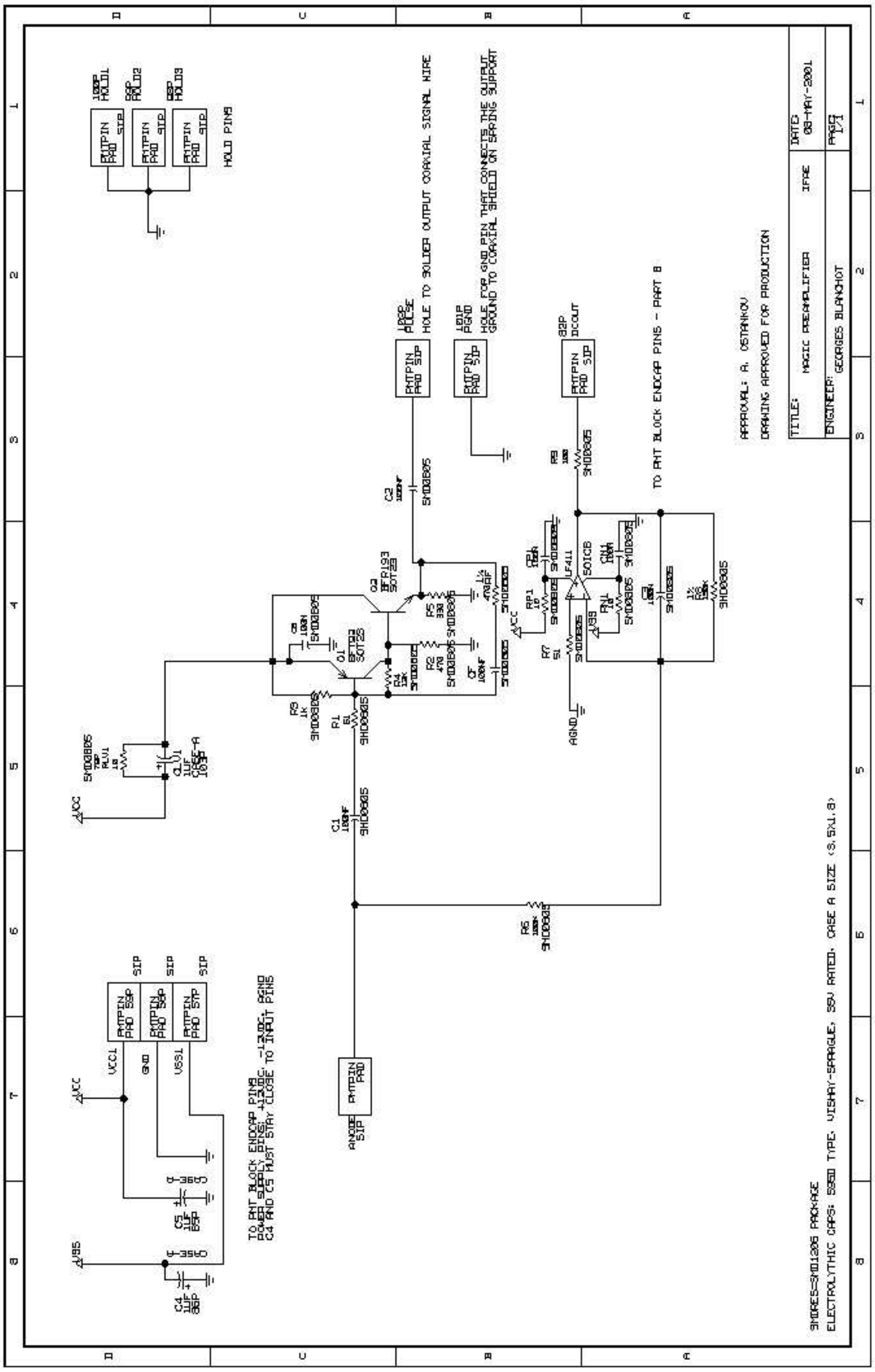

Figure 2.12: *Schematics of the preamplifier at the PMT base.*

Chapter 3

Pedestals

The pedestal of a FADC is the finite value which it outputs for zero input. Here we study the baseline in the line (pedestal mean) and its fluctuations (pedestal RMS) for different conditions of electronic noise and different levels of external light. The pedestal mean can be roughly regulated by software by the DAQ program. From April 2005 this pedestal mean is set to 15 counts per time slice so that small negative fluctuations on the signal line, due to night sky background noise, do not generate negative values in the FADC which are truncated to zero.

We make use of pedestal runs, that is, runs where all the events are triggered by a random signal and contain no Cherenkov pulses.

At the end of the chapter we provide a summary of the results that allows us to estimate the contribution of the different sources of noise.

3.1 HV, transmitters and receivers off

All the electronics except for the FADCs were switched off for pedestal run 13430 (20040128_13430_P_ReciversOff).

Figure 3.1 shows the distribution of charge in the first high gain slice for this run and pixels 66 (left) and 132 (right). The two-peak structure in pixel 132 is actually due to the so-called "AB noise" in the FADCs: the FADC baseline goes up and down every time slice with an amplitude that depends on the pixel. This AB noise is practically absent on pixel 66.

The easiest way to get rid of the AB noise is to always add up two consecutive time slices in order to calculate the pedestal RMS. Figure 3.2 shows the distribution of the summation of the first two slices for the same run and the same two pixels (66 on the left and 132 on the right). The spread of pixel 132 is still larger than for pixel 66 but there is no two-peak structure.

The mean and RMS of the summed charge in the first two high gain slices are plotted on figure 3.3 for all the pixels in the camera. The mean of the mean charges is 18.75 ADC counts, that corresponds to a typical FADC baseline of 9.4

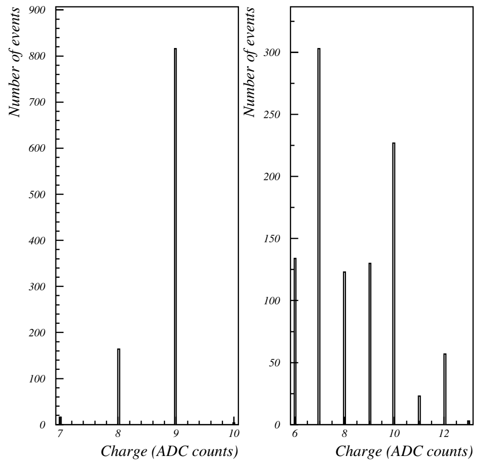

Figure 3.1: *Charge in the first high gain time slice for pixel 66 (left) and 132 (right) with all electronics turned off.*

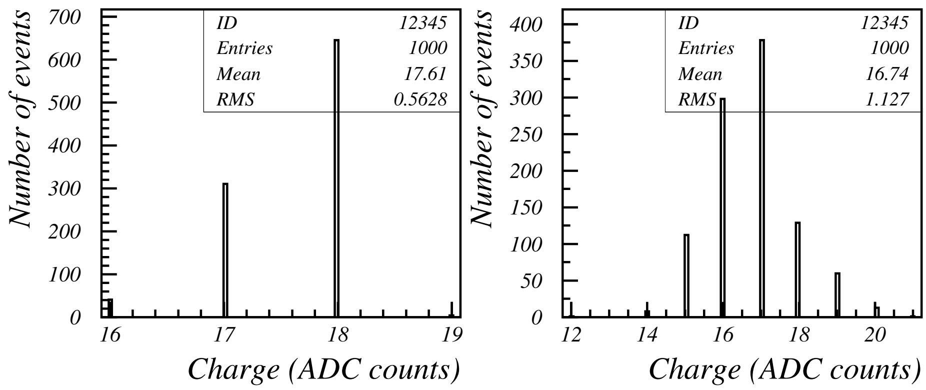

Figure 3.2: *Charge in the first slice plus charge in the second slice for pixel 66 (left) and 132 (right) with all electronics turned off.*

ADC counts per slice. The mean RMS is 0.88 ADC counts. This corresponds to a mean RMS of 0.62 ADC counts per slice in the absence of any electronic noise.

Figure 3.4 shows the same two distributions but for the charge added over the first 14 high gain slices. The charge RMS scales with the square root of the number of slices as expected if the noise in the slices is uncorrelated .

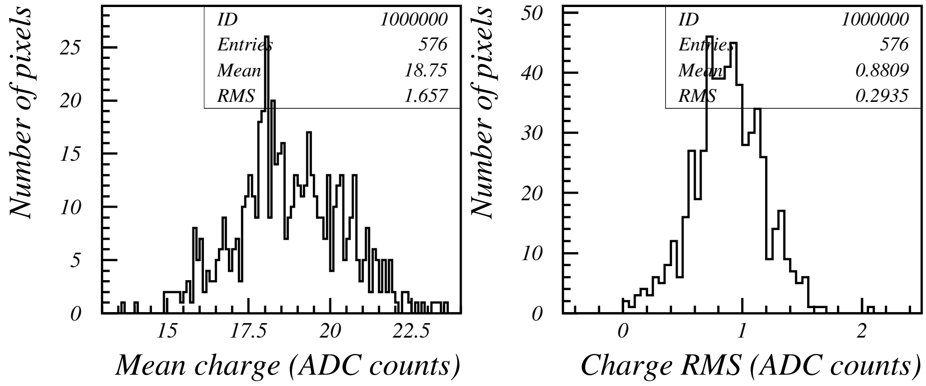

Figure 3.3: *Mean charge (left) and RMS (right) in the first two high gain slices for all the pixels in the camera with all electronics turned off.*

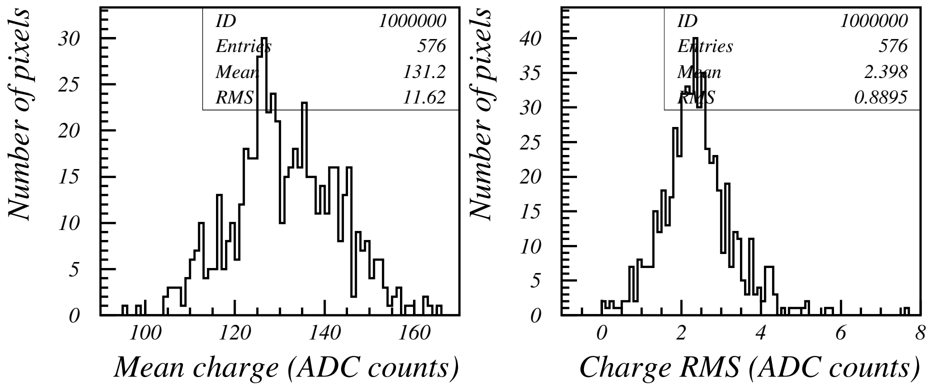

Figure 3.4: *Mean charge (left) and RMS (right) in the first FOURTEEN high gain slices for all the pixels in the camera*

3.2 HV and transmitters off, receivers on

The HV and transmitters were still off but the receivers were switched on for pedestal run 13428 (20040128_13428_P_ClosedLidsLVoff).

Figure 3.5 shows the distribution of the charge in the first two slices for this pedestal run and pixels 66 (on the left) and 132 (on the right). The RMS has increased while the charge remains constant.

The mean and RMS of the summed charge in the first two high gain slices are plotted on figure 3.6 for all the pixels in the camera. The mean of the mean charges is 18.87 ADC counts. This represents no significant change to the result when the receivers were off, that is, the baseline does not shift when the receivers are turned on. This is because the FADC modules have active compensation of any external DC level. In contrast the mean RMS is 1.13 ADC counts or 0.80 ADC counts per slice, i.e., the noise has increased by 30%.

Again we want to test if the RMS scales with the square root of number of slices and we plot the same two distributions for the charge integrated over the

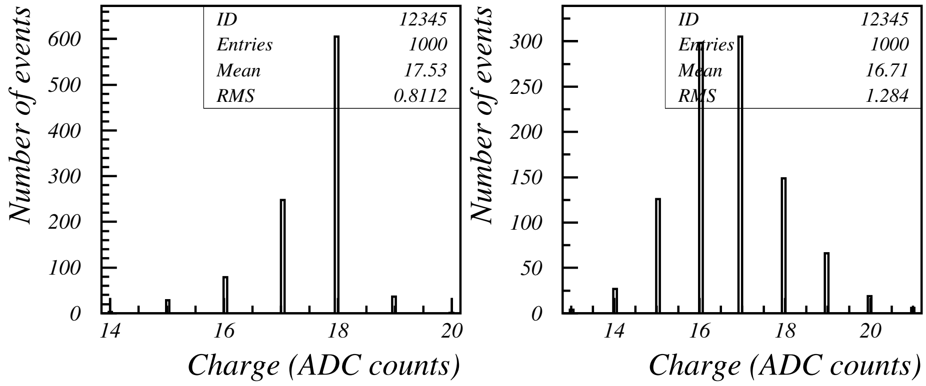

Figure 3.5: *Charge in the first two high gain time slices for pixel 66 (left) and 132 (right) with receivers switched on*

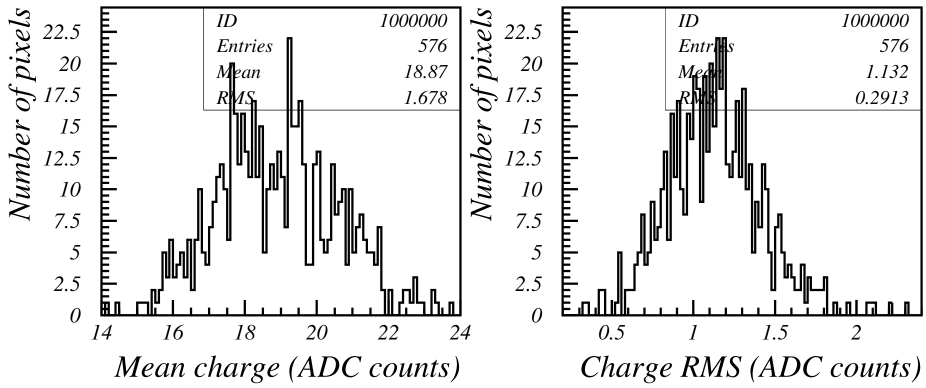

Figure 3.6: *Mean charge (left) and RMS (right) in the first two high gain slices for all the pixels in the camera with receivers switched on.*

first fourteen slices in figure 3.7. The mean RMS is 4.119 ADC counts, larger than 2.99 ADC counts expected from the increase in number of slices. This means that the noise in the different time slices that is introduced by the receivers is correlated.

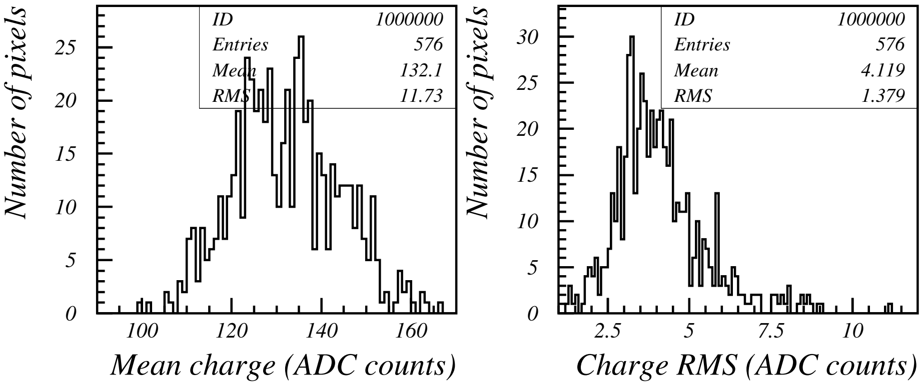

Figure 3.7: *Mean charge (left) and RMS (right) in the first FOURTEEN high gain slices for all the pixels in the camera with receivers switched on.*

3.3 HV off, transmitters and receivers on

The next step is to switch on the optical transmitters in the camera. The pixel HV is still off. This was done for pedestal run 13426 (20040128_13426_P_ClosedLidsHVoff). It must be said that the active loads (another possible source of noise) are switched on during this test but it has been checked that they introduce to additional noise.

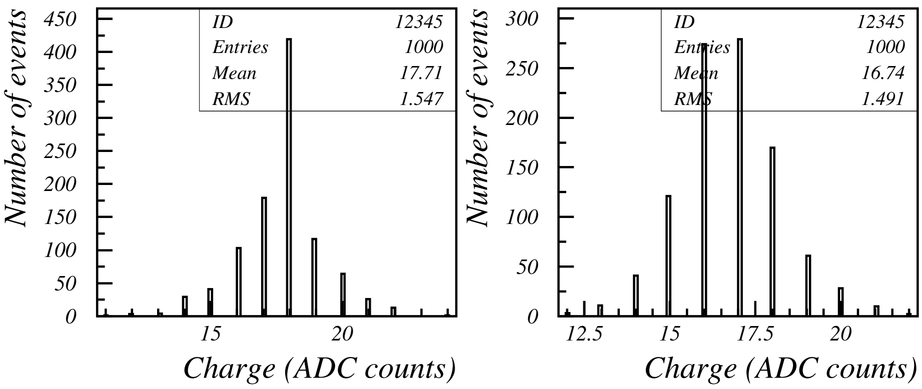

Figure 3.8: *Charge in the first two high gain time slices for pixel 66 (left) and 132 (right) with receivers switched on*

Figure 3.8 shows the distribution of the charge in the first two slices for this pedestal run and pixels 66 (on the left) and 132 (on the right).

The mean and RMS of the summed charge in the first two high gain slices are plotted on figure 3.9 for all the pixels in the camera. The mean of the mean charges is 19.3 ADC counts, so the baseline does not shift significantly when the transmitters are turned on. In contrast the mean RMS more than doubles to 2.36 ADC counts or 1.67 ADC counts per slice. The distribution of charge RMS also exhibits a longer tail to large values.

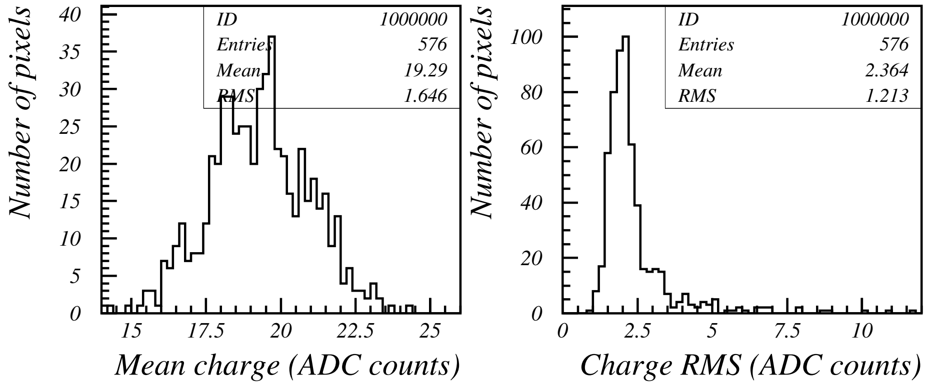

Figure 3.9: *Mean charge (left) and RMS (right) in the first two high gain slices for all the pixels in the camera with all electronics switched on except the pixel HV.*

3.4 Pixel HV, transmitters and receivers on, camera closed

Next we ramp up the pixel HV (HV settings 4timesFF13) but we keep the camera closed. All the electronics are switched on. The corresponding pedestal run is 13425 (20040128_13425_P_ClosedLidsHVon).

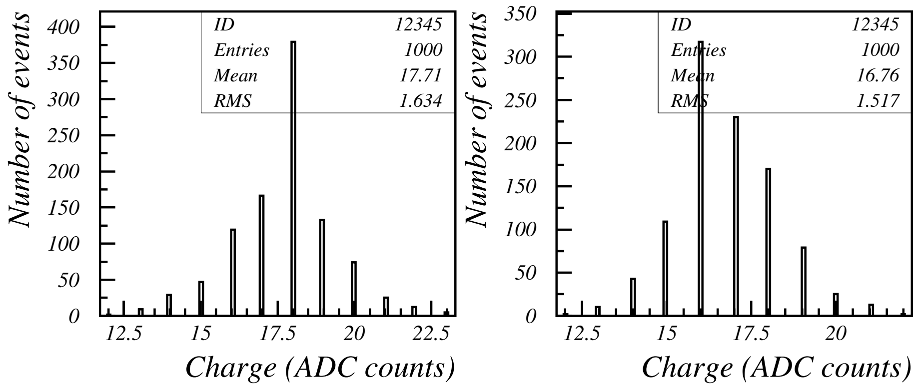

Figure 3.10: *Charge in the first two high gain time slices for pixel 66 (left) and 132 (right) with receivers and pixel HV switched on*

Figure 3.10 shows the distribution of the charge in the first two slices for this pedestal run and pixels 66 (on the left) and 132 (on the right). The pedestal RMS increases very slightly while the baseline stays constant. Both distribution have roughly gaussian shapes.

The mean and RMS of the summed charge in the first two high gain slices are plotted on figure 3.11 for all the pixels in the camera. Again we appreciate no shift in the baseline, and the mean RMS shows no significant increase, even if the tail gets somwehow longer.

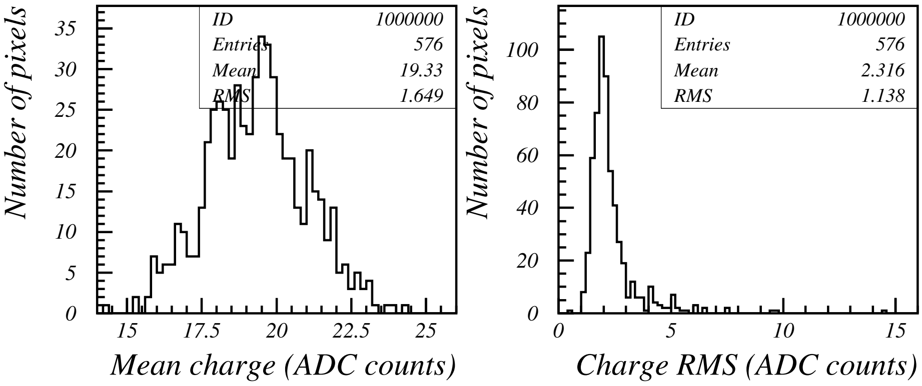

Figure 3.11: *Mean charge (left) and RMS (right) in the first two high gain slices for all the pixels in the camera with all electronics switched on including the pixel HV.*

3.5 Pixel HV, transmitters and receivers on, camera open, tracking extragalactic starfield

The last step is to open the camera while tracking an extragalactic position where no bright stars are present and the NSB are relatively low (the actual position is one of the standard OFF positions, OffMrk421-4). All the electronics are switched on (nominal datataking conditions) The corresponding pedestal run is 13435 (20040128_13435_P_OffMrk421-4).

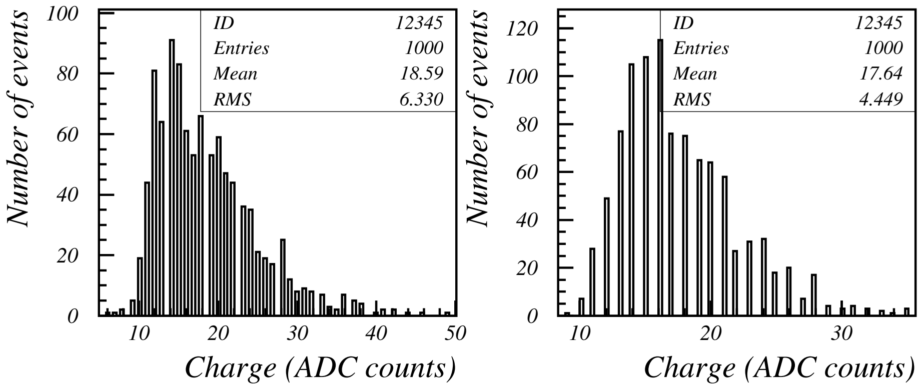

Figure 3.12: *Charge in the first two high gain time slices for pixel 66 (left) and 132 (right) with all electronics on, camera open and telescope tracking an extragalactic field of view.*

Figure 3.12 shows the distribution of the charge in the first two slices for this pedestal run and pixels 66 (on the left) and 132 (on the right). The pedestal RMS increases by a factor larger than 4, while the baseline stays roughly constant, as expected from the AC coupling. What has actually happened is actually more complex: the charge distribution is now the superposition of:

- The charge distribution with closed camera, what we may call the electronics pedestal. It is the same gaussian distribution that is displayed in figure 3.10 but has shifted to the left to compensate for the NSB tail. It is centered at ~13 ADC counts for pixel 66 while it was centered at 17.7 when the camera was closed; and it is around 14 ADC counts for pixel 132 while it was around 16.8 ADC counts before opening the camera.

- The poissonian distribution induced by the NSB, that shows up as a tail to the right of the electronics pedestal. The width of this tail is determined by the number of photoelectrons that are integrated in the 2-slice time window, approximately 0.8 for an extragalactic field of view.

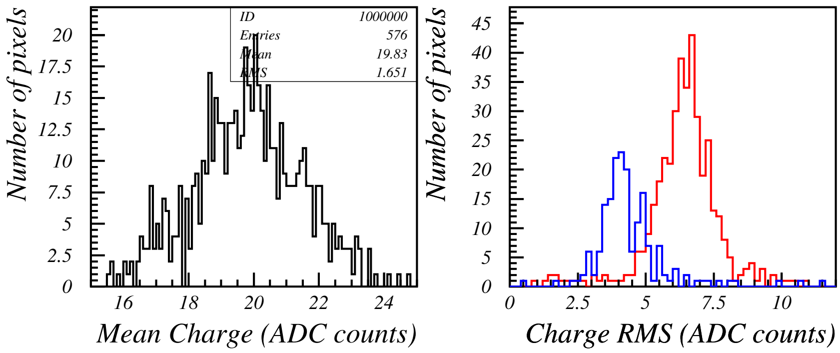

Figure 3.13: *Mean charge (left) and RMS (right) in the first two high gain slices for all the pixels in the camera with all electronics switched on, camera open and telescope tracking an extragalactic field of view. For the pedestal RMS the distribution has been split in inner pixels (red) and outer pixels (blue)*

The mean and RMS of the summed charge in the first two high gain slices are plotted on figure 3.13 for all the pixels in the camera. Again we appreciate no shift in the baseline. The mean RMS is almost three times larger than the RMS for closed camera.

The PMT gains have been flatfielded to obtain the same charge in ADC counts for all pixels in a calibration run. Since an outer pixel has a factor 4 larger collection area than an inner pixel, the same calibration light pulse must generate 4 times more photoelectrons in an outer pixel and the gain must be larger by roughly a factor 4 in the inner pixels. The fluctuation of the charge is proportional to the square root of the number of photoelectrons. After applying this factor to the pedestal RMS and taking into account the factor 4 difference in gain, one would expect a factor 2 smaller RMS in ADC counts for the outer pixels. However the mean pedestal RMS is 6.4 ADC counts and 4.5 ADC counts for respectively inner and outer pixels. If we substract the electronic noise, the ratio of the inner and outer pixels is ~1.55. A number of reasons have been suggested for this disagreement:

- The light collector on top of the PMT is less efficient for outer than for inner pixels.
- The light collector for outer pixels concentrates the photons on an area of the photocathode that has a lower QE.
- The outer PMTs are operating at a HV that is at the lower limit of their nominal operating range and this could lead to stronger fluctuations in the photoelectron collection in the dynode system.
- The camera is flatfielded for ultraviolet pulses while the pedestal RMS and the anode currents are due to star and NSB light that peaks at longer wavelengths. At these wavelengths both the collection efficiency and the QE in inner and outer pixels may differ.

In general it has to be said that the ratio of number of photoelectrons in calibration events in inner and outer pixels is not 4 either but rather 2.5, (see figure 2.9) and 1.55 is roughly $\sqrt{2.5}$. This points to the first item of the list above as the most possible explanation: the outer pixels have a poorer light collection efficiency.

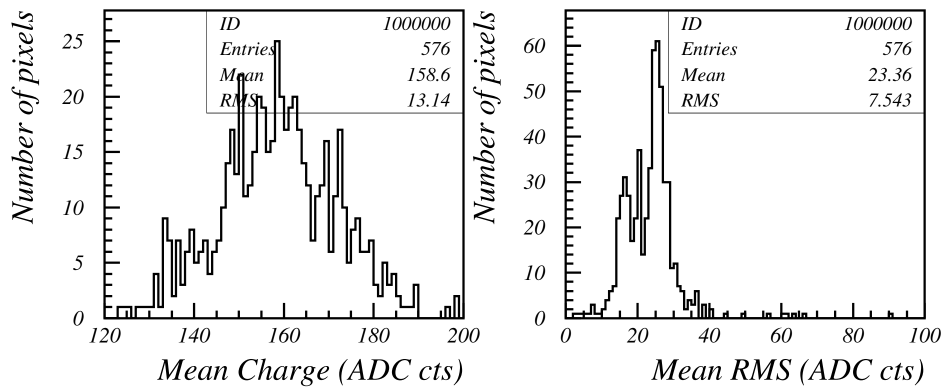

Figure 3.14: *Mean charge (left) and RMS (right) in the first FOURTEEN high gain slices for all the pixels in the camera with all electronics switched on, camera open and telescope tracking an extragalactic field of view.*

Figure 3.14 shows again the distribution of mean charge and charge RMS but this time for the integrated charge over the first fourteen high gain slices. The mean RMS is 50% larger than a simple extrapolation of the mean RMS for 2 slices with the square root of the number of slices. This indicates that the noise is correlated, probably because the pulses are stretched at the receivers over several slices.

Let us look in more detail into this correlation. Figure 3.15 illustrates for several pixels the dependence of the pedestal RMS on the number of slices where the charge is integrated. The data correspond to the pedestal run 41662, that

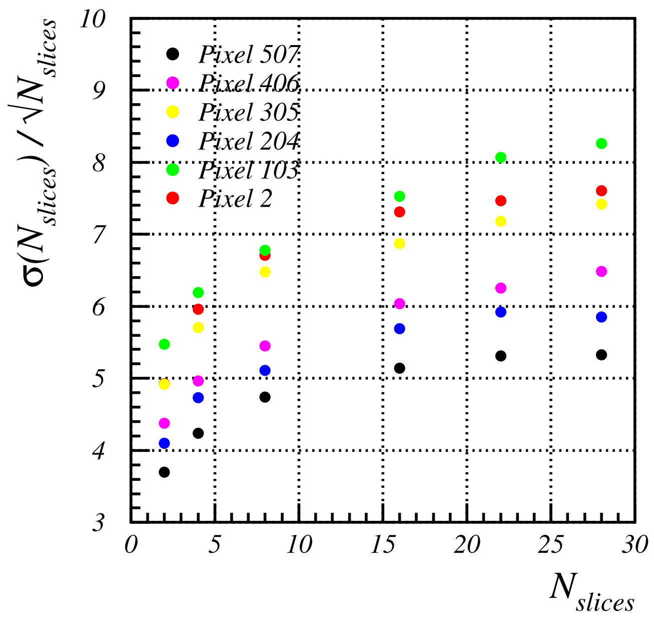

Figure 3.15: *Pedestal RMS calculated in a fixed window of a given number of slices N_{slices} divided by N_{slices}, as a function of N_{slices}, for several inner and outer pixels chosen at random. The data correspond to the pedestal run 41662, recorded on 2004_10_17 while pointing at an extragalactic object, 3c66a.*

were recorded with a fully furnished mirror on 2004_10_17. The pedestal RMS has been divided by the number of slices. The fact that this parameter reaches a plateau only at about 15 slices means that the fluctuations are correlated at shorter time scales. This is what we would expect if the correlation is due to the stretcher, which has a time constant of about 3 time slices.

The curve is slightly different for the five pixels. This may indicate that the corresponding stretchers have slightly different time constants.

3.6 Pixel HV, transmitters and receivers on, camera open, tracking Crab Nebula

We move now to Crab Nebula, a particularly bright galactic position. Crab is especially important because it is our standard calibration γ-ray source. The corresponding raw data file is 20040825_35353_P_CrabNebula_E.root. The data were taken after the August 2004 technical access to tune the active mirror control so the mirror spot size is nominal and a star image is mostly concentrated inside a single pixel. It must be stressed that the night sky background was particularly strong during the August observations (see chapter 7). Most of the Crab data are taken under lower NSB.

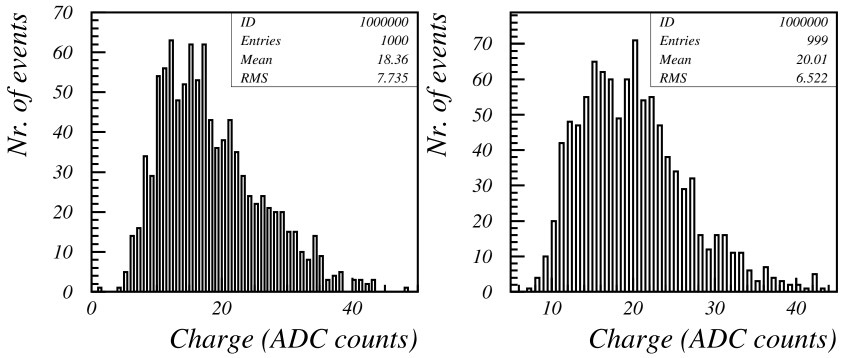

Figure 3.16: *Charge in the first two high gain time slices for pixel 66 (left) and 132 (right) with all electronics on, camera open, telescope tracking the Crab Nebula.*

Figure 3.16 shows the distribution of the charge in the first two slices for this pedestal run and pixels 66 (on the left) and 132 (on the right). The pedestal RMS has increased in ∼20-25% with respect to the values for the extragalactic position. It must be noted however that Crab's field of view is not flat, that is, there are numerous stars that increase the pedestal RMS for some pixels significantly above the average.

The mean and RMS of the summed charge in the first two high gain slices are plotted on figure 3.17 for inner and outer pixels separately. The mean charge stays constant around 20 ADC counts as expected using AC coupling. The mean pedestal RMS for all pixels is 7.6 ADC counts. There are quite some outlayers in the distribution, due to bright stars in the FOV like ζ Tauri. This pedestal RMS represents an increase of ∼30% with respect to the extragalactic field. As we shall see in the chapter devoted to anode currents, this is to be expected from the increase in star and galactic diffuse light. The mean pedestal RMS is 8.5 ADC counts for the inner pixels and 5.9 ADC counts for the outer pixels. This is again a factor 1.4 difference.

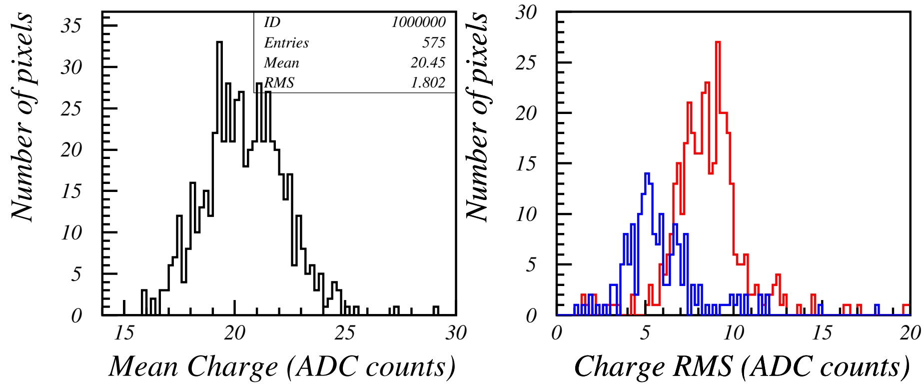

Figure 3.17: *Mean charge (left) and RMS (right) in the first two high gain slices for all the pixels in the camera with all electronics switched on, camera open, telescope tracking Crab Nebula. On the right panel, the red histogram corresponds to the inner pixels and the blue one corresponds to the outer.*

3.7 Pixel HV, transmitters and receivers on, camera open, tracking extragalactic starfield with moonlight

Here we track again an extragalactic position with no bright stars and nominal electronic conditions but under the presence of moonlight (half moon, about 90° away from the telescope pointing direction). The anode currents were very high: $\sim$6 μA to compare with 1 μA for moonless observations. The corresponding raw data file is 20041121_00045379_P_DarkPatch3-open_E.root.

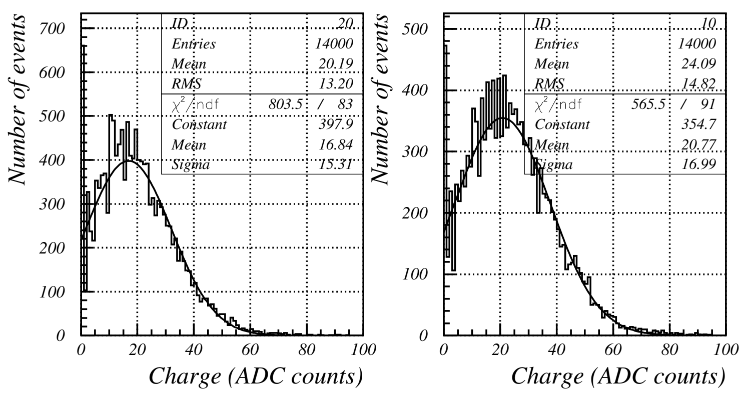

Figure 3.18: *Charge in the first two high gain time slices for pixel 66 (left) and 132 (right) with all electronics on, camera open, telescope tracking an extragalactic field of view under strong moonlight.*

Figure 3.18 shows the distribution of the charge in the first two slices for this pedestal run and pixels 66 (on the left) and 132 (on the right). The pedestal

RMS is a factor 2-3 larger than that for moonless conditions. It should be noted however that the distributions are truncated at 0 ADC counts, so the calculated RMS understimates the real fluctuation. We can apply a gaussian fit to the two distibutions to account for the part of the distribution missing at negative values. We obtain a width that is around 20% larger than the distribution RMS. The baseline (mean pedestal charge) reduces also by another 20% and now agrees very well with the baseline in any other condition, as expected from the AC coupling in the electronics.

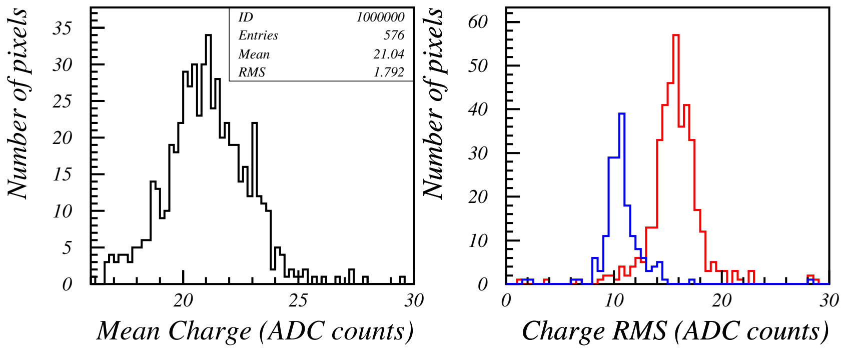

Figure 3.19: *Mean charge (left) and RMS (right) in the first two high gain slices for all the pixels in the camera with all electronics switched on, camera open, telescope tracking an extragalactic field of view under strong moonlight. On the right panel, the solid histogram correspond to the inner pixels and the hatched one correspond to the outer.*

The mean and RMS of the summed charge in the first two high gain slices are plotted on figure 3.19 for inner and outer pixels separately. It is worth mentioning that both the mean and the RMS are estimated from the distribution and not using the gaussian fit.

The RMS for outer pixels is again a factor $\sim$1.5 smaller than the RMS for inner pixels. The mean RMS for all pixels is 2-3 times larger than the RMS for a moonless extragalactic position. This is in good agreement with the factor 6 increase in DC, since the pedestal RMS grows with the square root of the light while the DC grows linearly. In a special chapter below we will study the correlation between anode DC and pedestal RMS more systematically.

3.8 Summary and discussion

Table 3.1 summarizes the results obtained in this chapter concerning pedestal mean charge and charge RMS. The values for 1 slice has been simply scaled from the results for 2 slices (the mean has been divided by two and the RMS divided by $\sqrt{2}$).

ADC counts, average over camera	closed HV off LV off rec off	closed HV off LV off rec on	closed HV off LV on rec on	closed HV on LV on rec on	extragal HV on LV on rec on
14 slices <Q>	131	132	135	135	159
14 slices σ_Q	2.4	4.1	9.8	9.1	23.36
2 slices <Q>	18.8	18.9	19.3	19.3	19.8
2 slices σ_Q	0.9	1.1	2.4	2.3	5.8
1 slice <Q>	9.4	9.45	9.65	9.65	9.9
1 slice σ_Q	0.6	0.8	1.7	1.6	4.1
$\sigma_Q(14)/\sigma_Q(2)$	2.7	3.7	4.1	4.0	4.0

Table 3.1: *Summary of mean charge and charge RMS over all pixels for difference noise conditions. The values for 14 and 2 slices have been measured while the ones for 1 slices are scaled down from those of 2 slices. The last row displays the ratio between the RMS calculated with 14 slices and that calculated with 2 slices. It would be* $\sqrt{14/2} = 2.7$ *if the noise in the slices were not correlated.*

Table 3.2 reviews the results that have been obtained for open camera (all electronics on) and very different noise conditions: from the smallest possible background noise (an extragalactic patch of the sky containing no bright stars) to a relatively strong moon illumination.

3.8.1 NSB estimation

Average over pixels	extragal no moon		Crab no moon		extragal moon	
	INNER	OUTER	INNER	OUTER	INNER	OUTER
14 slices σ_Q (ADC cts)	27.5	20.1	31.7	22.6	54.6	39.2
14 slices σ_Q^{NSB} (ADC cts)	26.0	17.9	30.4	20.7	53.8	38.1
14 slices σ_Q (phe)	2.5	4.2	3.0	4.9	5.2	9.0
14 slices N_{phe}	6.25	17.6	9.0	24	27	81
NSB rate (phe/ns)	0.14	0.38	0.19	0.52	0.59	1.75

Table 3.2: *Charge RMS in inner and outer pixels with all electronics on and the NSB of three different fiels-of-view: extragalactic (minimal NSB), Crab (high NSB) and extragalactic under relatively intense moonlight. We have substracted the electronic noise, converted the RMS into phe using the corresponding conversion factor and a correction for the excess noise factor (see text), estimated the number of phe which correspond to this fluctuation and the rate of phe per ns.*

We can estimate the rate of NSB photons using the pedestal RMS. To begin with we sustract the contribution of electronic noise from the pedestal RMS that is tabulated in Tab. 3.2. The electronic noise is given by the RMS that we measured with closed camera and all electronics on. Then we convert ADC counts into photoelectrons using the average conversion factors that have been obtained using the F-Factor method (adopted from [7]). We assume that 1 phe corresponds to 7.8 ADC counts for the inner pixels and 3.2 ADC counts for the outer. We calculate the number of photoelectrons taking into account the excess noise factor of the PMT:

$$\sigma_{ped} = F^2 \cdot \sqrt{N_{phe}} \tag{3.1}$$

with F^2=1.32. And we finally divide by 46.2 ns to determine the rate of NSB. The results can be found in table 3.2.

3.8.2 Influence of noise in shower charge determination

Let us now try to compare the noise in the pixels with the expected fluctuations of the charge in the showers. A Cherenkov pulse has a typical width (FWHM) of two slices. Let us assume that we estimate the charge of a pulse by integrating the 4 slices around the slice with the maximum charge. Of course we can use more sophisticated methods to measure the charge in the pulse but we do not think they will reduce the relative fluctuation in the charge by a substantial amount (this remark is meant to be controversial...). In the last row of table 3.2 we have multiplied the pedestal RMS measured for 2 slices by a factor $\sqrt{2}$ to estimate the pedestal RMS in 4 slices.

The resulting σ_{ped} in the inner pixels is 1.2 phe for the extragalactic dark patch, 1.5 phe for Crab and almost 3 phe under moonlight. For outer pixels it is a factor 1.7 larger. As we shall see in the chapter about single pixel rates, the individual channels trigger around 10 phe. This means that the minimal shower fluctuation $\sigma_{Cher,min}$ is $\sqrt{10}$ ~3 phe, that is, $\sigma^2_{Cher,min}$ is about 7 times larger than the inner pixel σ^2_{ped} due to extragalactic noise or 4.5 larger than σ^2_{ped} in the FOV of Crab. We can conclude that background noise does not signicantly add to the intrinsic fluctuations of the shower in the case of the inner pixels.

The outer pixels are not in the trigger so it does not make much sense to compare the trigger and the analysis thresholds. And since they do not trigger it is not straightforward to estimate the minimum amount of charge that is collected in an outer pixel either.

In the case of moonlight, table 3.2 shows that σ_{ped} is comparable to $\sigma_{Cher,min}$. But for moonlight we would have to increase the DTs (hence also the telescope trigger energy threshold) to reduce the accidental trigger rate and the shower fluctuations would again dominate over the background fluctuations. It must be noted however that the increase in DT is directly proportional to σ_{ped}. As $\sigma_{Cher,min}$ is directly proportional to the square root of the minimum shower charge, it turns out that:

$$\sigma_{Cher,min} \propto \sqrt{\sigma_{ped}} \tag{3.2}$$

This is to say that background noise eventually dominates over the minimum shower fluctuation. But for an extragalactic field of view and the inner pixels, this happens when the moon increases σ_{ped} by a factor 6.25, or the DC increases up to $\sim$40 μA. This DC is too high for our PMTs so again we arrive to the conclusion that background noise never dominates over the intrinsic fluctuations for the inner pixels, although its relative contribution to the total charge fluctuation grows with the moonlight intensity.

This conclusion would not hold true if we integrated the charge over a larger number of slices. For instance the extragalactic noise integrated over 14 slices is 4 phe, again larger than the intrinsic fluctuation of the smallest Cherenkov pulses. This stresses the importance of the signal extractor to minimize the effect of the noise.

3.9 Conclusions

The main conclusions are:

- The pedestal baseline stays constant, as expected from the AC coupling in the signal transmission line.
- The pedestal RMS increases as the different hardware elements in the line are switched on.
- The dominant component in the noise is the NSB (the corresponding σ^2 is more than a factor 4 larger than all the others together).
- The RMS does not increase with the square root of number of slices, except for the case when all the electronics are switched off and only the FADC noise is present.
- When the camera is open, the pedestal RMS in ADC cts is 1.4 times larger for the inner pixels. This does not agree with the expected value of 2.
- The background noise is always smaller than the poissonian fluctuations of the shower.

Chapter 4

Individual Pixel Rates

This chapter deals with individual pixel trigger rates (IPR). IPR are measured in scalers running at the L2T VME crate that were installed in May 2004. They are readout and subsequently sent over TCP/IP every second to Arehucas that in turn saves them every 10 seconds to the report file.

IPR of course depend on the discriminator thresholds (DT) that are set on the pixels. The DTs are set in and read from the receiver boards through a serial connection in the central control PC and measured in arbitrary "DAC units".

A utility in the Arehucas distribution (rates/scan_IPR.vi) also allows to scan the IPR in a range of DTs. These are the usually called "IPR scans". A full scan in the DT range of 0 to 250 DAC units in steps of 5 units takes about 10 minutes. This time is limited by the time it takes to set all the DTs through the serial connection.

We start by measuring the IPR in the all typical configurations of the telescope electronics to establish what is the factor dominating our accidental rate. Then we investigate the evolution of the IPR with time and we finally ask ourselves if it is possible to flatfield the pixel discriminator thresholds so that all the pixels have the same trigger response.

4.1 IPR for different electronic configurations

4.1.1 HV, transmitters and receivers off

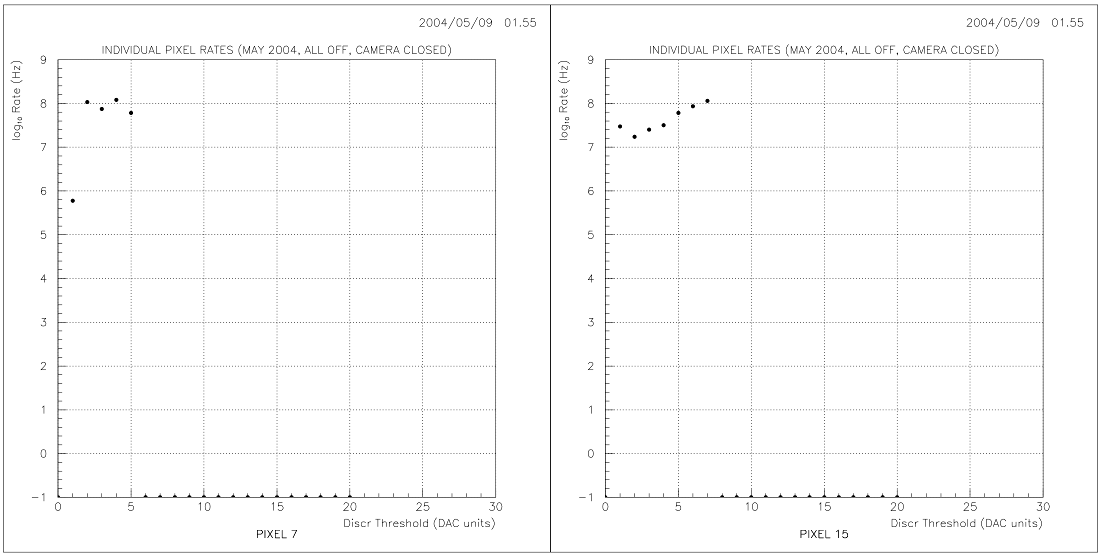

Figure 4.1: *IPR as a function of DT with all electronics turned off for pixel 7 (left) and pixel 15 (right).*

All the electronics except the FADCs were switched off for the data in file ipr_2004_05_09_closed_camera1_alloff.txt

Figure 4.1 displays an "IPR scan" in this configuration. The IPR is practically flat or even grows for the lowest DT in some pixels due to saturation in the IPR scalers close to 100 MHz: in reality it should always decrease exponentially. This is actually the case for DT$\sim$5 but it happens so fast that it cannot be seen for these hardware conditions (see plots next subsections for a more "standard" evolution of the IPR).

4.1.2 HV off, transmitters and receivers on

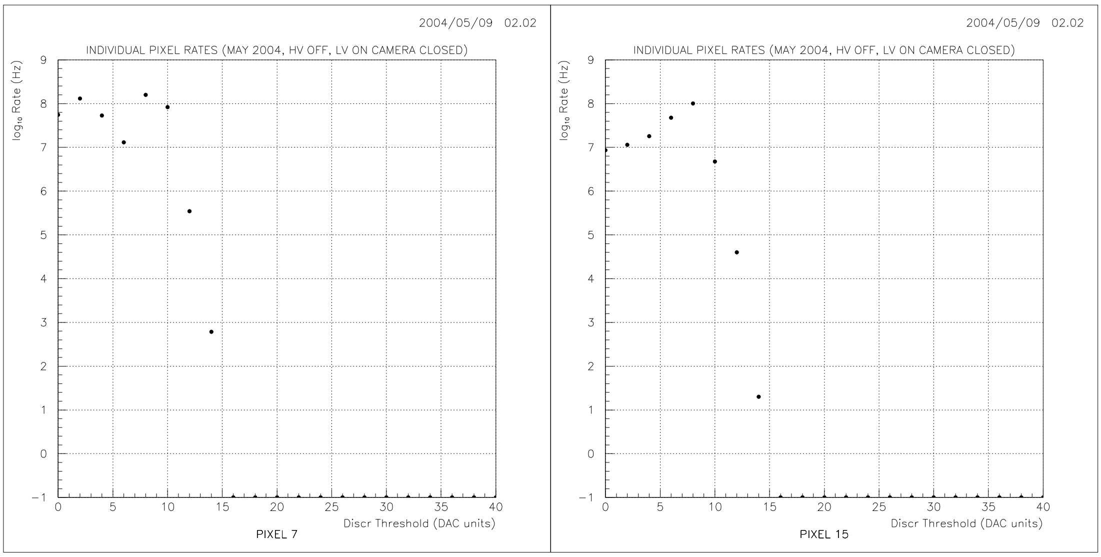

Figure 4.2: *IPR as a function of DT with pixel HV off, and trasmitters and receivers on for pixel 7 (left) and pixel 15 (right).*

We turn on the receivers and the transmitters. The pixel HV stays off. We make an IPR scan and save it to file ipr_2004_05_09_closed_camera1_hvoff_lvon.txt.

Figure 4.2 displays the corresponding IPR scan for the same two generic pixels. The IPR cuts off abruptly for DT$\sim$10.

4.1.3 Pixel HV, transmitters and receivers on, camera closed

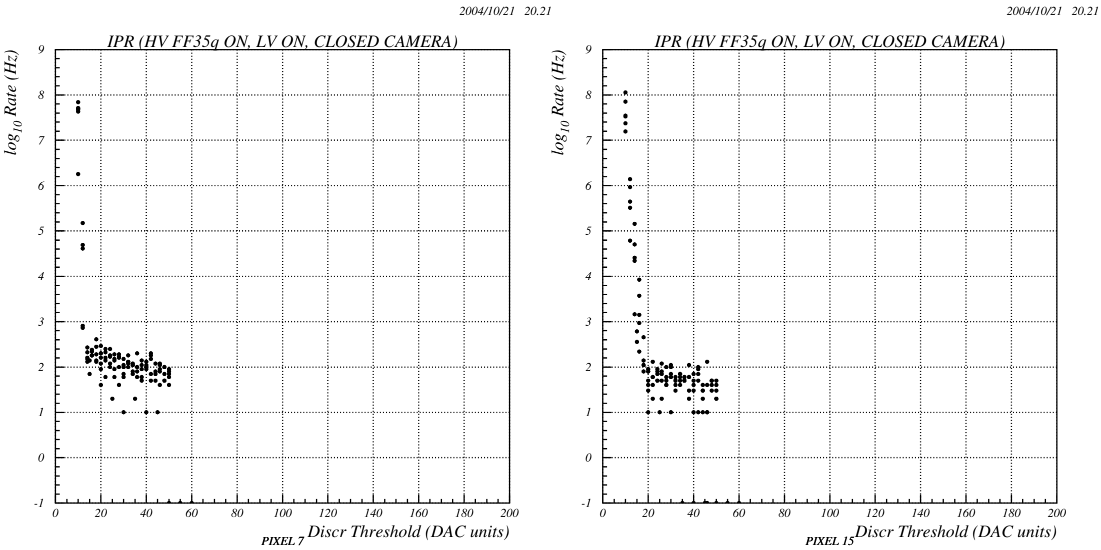

Figure 4.3: *IPR as a function of DT with pixel HV, trasmitters and receivers on for pixel 7 (left) and pixel 15 (right). Mind the change of scale as respect to the last plot.*

We ramp up the HV (HV settings FF35) and save an IPR scan to file ipr_2004_05_08_closed_camera_all_FF35q.txt.

Figure 4.3 displays the corresponding IPR scan for the same two generic pixels. There is no significant difference in the cutoff IPR. This was to be expected because the pedestal RMS does not increase when the pixel HV is switched on. All the nominal electronic noise is active for these conditions. The accidental coincidence rate for 4-fold coincidence is only a few Hz for IPR$\sim$500 kHz, so it would suffice to set the DTs at $\sim$15 to get rid of any accidental triggers in the absence of night sky background and starlight.

4.1.4 Pixel HV, transmitters and receivers on, tracking extragalactic starfield

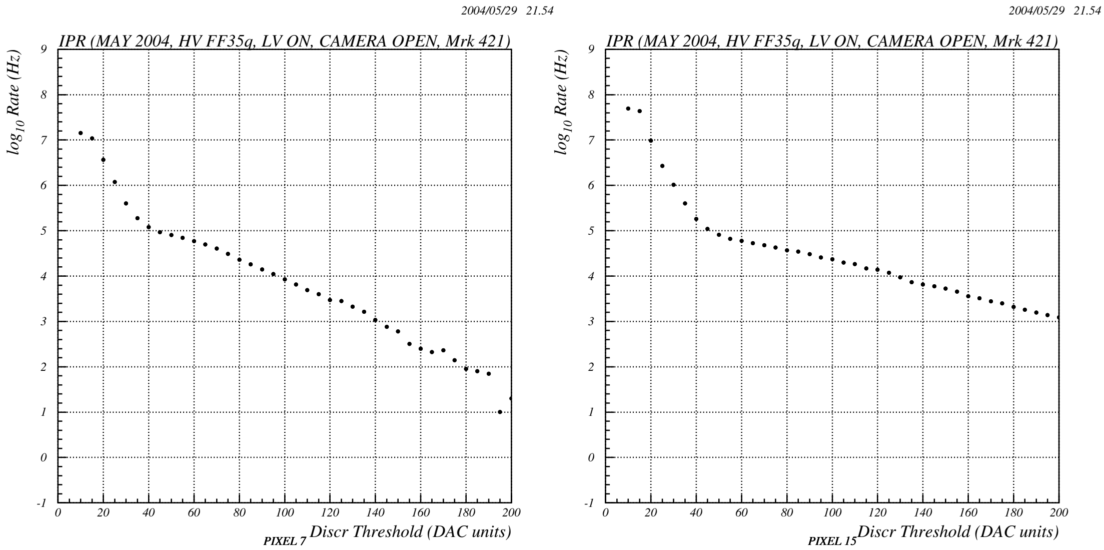

Figure 4.4: *IPR as a function of DT with all electronics on, camera open and tracking Mrk 421, for pixel 7 (left) and pixel 15 (right).*

Finally we open the camera while tracking an extragalactic starfield (Mrk 421). All the electronics are switched on. These are the nominal datataking conditions. An IPR scan was saved to file ipr_040512_scan_mkn421_opencamera.txt.

Figure 4.4 displays the corresponding IPR scan for the same two generic pixels. Under the presence of NSB and stars in the field of view, the cutoff IPR doubles and is now around 20. Two regions can be distinguished in the plot:

- Below DT=20 the predominant source of noise is "direct" photoelectrons produced at the PMT photocathode and amplified by the dynode system. The slope is very steep: the IPR falls almost one order of magnitude for every 10 DAC units in DT.

- Above DT=20 the IPR is produced by afterpulsing, i.e., by positive ions that are generated by photoelectrons at the first dynode, fly back to the cathode and generate a large amount of photoelectrons. These large pulses are still able to trigger the individual pixels for large DTs. The curve is much shallower in this range.

Only an IPR above 500 kHz-1 MHz generates a significant accidental rate for 4-fold coincidence. For each individual pixel, we can look for the DT for which the IPR reaches this critical rate. The critical DTs are plotted on figure 4.5 for IPR=1 MHz (left) and IPR=300 kHz (right) in an extragalactic position.

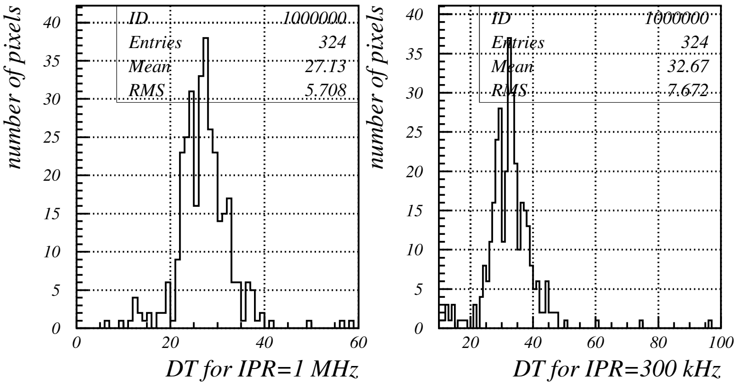

Figure 4.5: *Discriminator thresholds for which the IPR reaches 1 MHz (left) and 300 kHz (right). The telescope was tracking an extragalactic object, Mrk 421, during May 2004.*

The average value is 27 DAC units for 1 MHz and 33 DAC units for 300 kHz. The RMS of both distributions is around 20%. In general both points lie on the range where afterpulsing is negligible compared to direct photoelectrons. These numbers will be shift slightly upwards after the full mirror installation in July.

4.2 Time stability of IPR

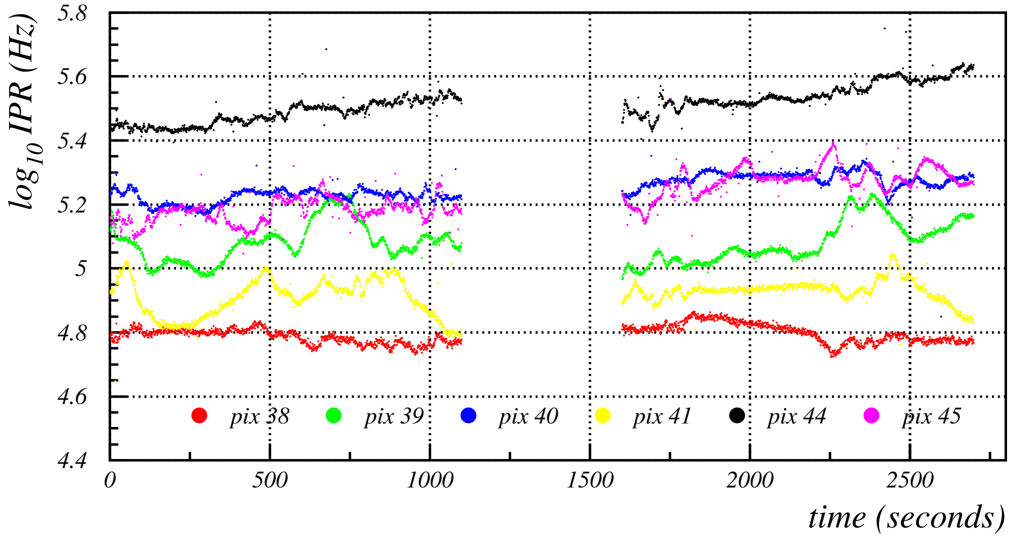

Figure 4.6: *Evolution of the IPR with time for a number of pixels chosen at random in the trigger area. The camera was closed in the time gap between 1200 and 1600 seconds to perform a laser adjust. The telescope was tracking a galactic field (the so-called OffCrab-5 position) on 2004-11-18. No bright stars were present on the field of view.*

The IPR are not stable with time. Figure 4.6 shows the time evolution of the IPR for some of the inner pixels selected at random. No bright stars were present on this galactic field of view. There are strong variations in the IPR with amplitudes up to around 0.2 in logarithmic scale (about 50% in linear scale) in time scales of 2-3 minutes. Given above-mentioned dependence of IPR on DT, these variations correspond to ~2-3 DAC units in the discriminator threshold.

Changes in the DT scale can be monitored more directly using IPR scans taken repeatedly one after the other. It must be noted however that scans are relatively slow (it takes around 5 minutes to complete one), so faster changes are hard to trace. Figure 4.7 compares two IPR scans that were performed one after the other. The left panel of the figure plots the DT for 1 MHz of one scan versus the other, while the right panel represents the difference of DT(1 MHz) in both scans. The average DT(1 MHz) increases by roughly 14% in the second scan, perhaps due to atmospheric conditions. But the dispersion of the distribution is anyway large: the relative RMS is around 10%, in absolute terms 3 DAC units.

Dim stars (say, below 4^m) are present in any field of view, so we may still claim that changes in the pixel IPR are due to changes in the star field resulting from rotation or oscillation of the PMT camera. That is why we performed a further test under more controlled noise conditions. We installed a sheet of plexiglass in front of the PMT camera and covered it with paper to eliminate the NSB

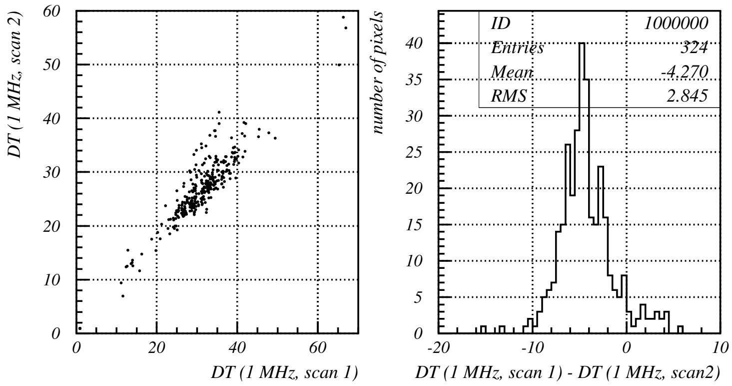

Figure 4.7: *The left panel compares the DT for which IPR reaches 1 MHz in two different scans performed one after the other. The right panel shows the difference in DT for the two scans. The telescope was tracking an extragalactic object, Mrk 421.*

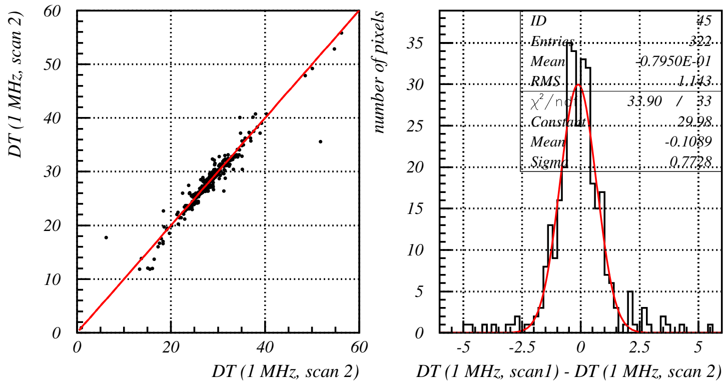

Figure 4.8: *The left panel compares the DT for which IPR reaches 1 MHz in two different scans performed one after the other. The right panel shows the difference in DT for the two scans. The telescope was at the access position and a screen of plexiglass with some paper covered the camera to eliminate the NSB.*

(standard paper was measured in the lab to have a transmission factor of roughly 0.1 for a LED very similar to the ones used in the calibration box). The camera was then illuminated with the maximum intensity of green-blue continuous light that is available in the calibration box. The average anode DC was around 1 μA, i.e., comparable to the typical DC for an extragalactic source, but the illumination was more homogeneous than any field-of-view in the sky.

We made two consecutive IPR scans under these conditions. Figure 4.8 compares the DT for IPR=1 MHz in the two scans. There is no noticeable change in the DT(1 MHz) averaged over the whole camera, as expected under these carefully controlled noise conditions, but the pixels show again a dispersion with RMS around 5% (1-2 DAC counts for 30 DAC counts mean).

We can conclude that stars cannot be held as responsible for the observed variations in IPR. The change in pixel DC in two consecutive IPR scan is negligible, so the PMT QE, collection efficiency or gain are not responsible either. We may still think that the effective discriminator threshold level is not stable with time, but this is hard to believe since we do not expect the hardware elements in the optical receivers to change in a time scale of minutes. The most plausible explanation for the variation is a change in gain in the optical trasmission line of amplitude 5-10%. This amplitude is compatible with the gain variations of the optical trasmission system that were measured in the lab [10].

All this boils down to saying that it is impossible to define a fixed discriminator threshold for each pixel so that we stay just above the noise. We must either fix the threshold ∼3-7 DAC units above its average critical value to allow for the maximum observed fluctuations or dynamically control it to adapt to these changing noise conditions.

4.3 Flatfielding of Discriminator Thresholds

Different channels show different IPR for a fixed DT. This could be simply due to the fact that the gain changes from channel to channel. But we would also like to investigate if the actual threshold level that is set on the receiver board when we program a given DT in DAC units depends on the channel. If this were the case, we would get different IPR for a fixed DT even if the camera were perfectly flatfielded.

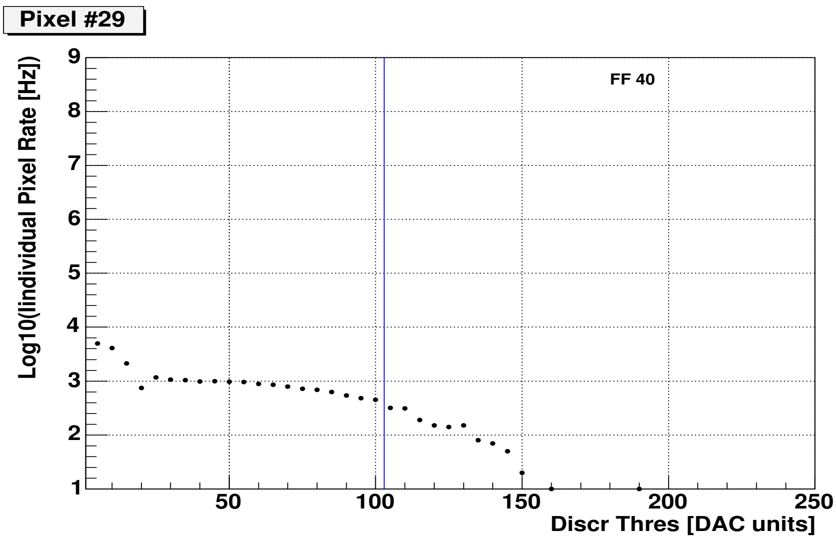

Figure 4.9: *IPR scan of pixel 29 while tracking an extragalactic source and flashing on the camera with 1Led_Green calibration pulses. The IPR counters were veto-ed to reduce the accidental IPR.*

We use a special setup for special “DT flatfielding”. Our goal was first to establish the correlation between the charge measured in ADC counts and the

DT in DAC units. We flashed standard calibration pulses (1Led_Green) on the camera at a rate of 1 kHz. Then we made an IPR scan: at low DT we expected the calibration pulses to always trigger the pixel, that is, we expected a plateau at a fixed value of 1 kHz. Above a critical DT the IPR was expected to fall down to 0.

The problem with the method was that the background light triggers the pixel at a rate above 1 kHz even for relatively high DT (see first section of this chapter). It was effectively impossible to separate the calibration rate from the accidental rate. To get rid of the accidentals, the units that measure the IPR were re-programmed to veto single pixel triggers outside a window of 100 ns centered on the calibration pulse.

The result of an IPR scan using the veto-ed IPR counters is illustrated in Fig. 4.9 for pixel 29. The accidental rate is reduced in several orders of magnitude and the plateau at 1 kHz is clear visible. Unfortunately the plateau falls down rather slowly for high DTs and there is not a very well defined DT cutoff.

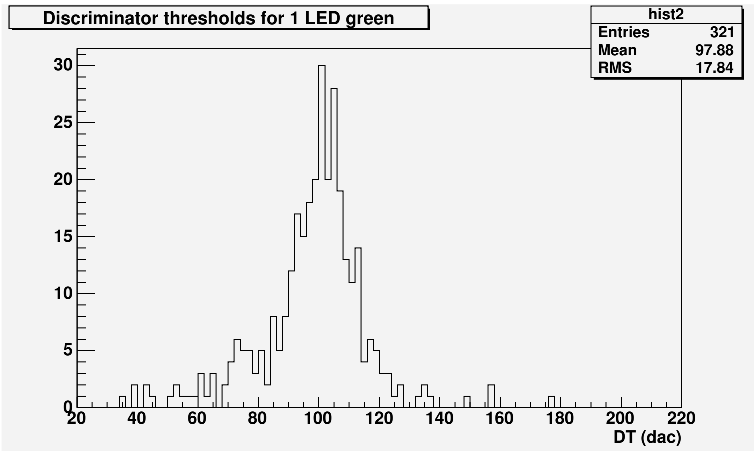

Figure 4.10: *Distribution of $DT_{1/2}$. Only pixels in the trigger area are displayed.*

For each pixel we looked for the point where the IPR falls down in a factor 2 ($\mathrm{DT}_{1/2}$, marked by the two blue lines in figure 4.9). This point would correspond to the average calibration pulse. The distribution of these DTs for all the pixels in the trigger is shown in figure 4.10. It is centered at 98 DAC units and has a large dispersion of 20% RMS.

The dispersion of $\mathrm{DT}_{1/2}$ could be due to the dispersion of the pixel gains. We can try to correct for this effect by dividing $\mathrm{DT}_{1/2}$ by the average charge of the calibration pulse Q_{cal} in ADC counts for the corresponding pixel using a calibration run that was taken right after the IPR scan. The distribution of this quantity is shown in figure 4.11. The mean of the distribution is **0.43 DAC units per ADC count integrated charge**. This is the average conversion factor between DAC units in the DT and integrated charge in the FADC. The

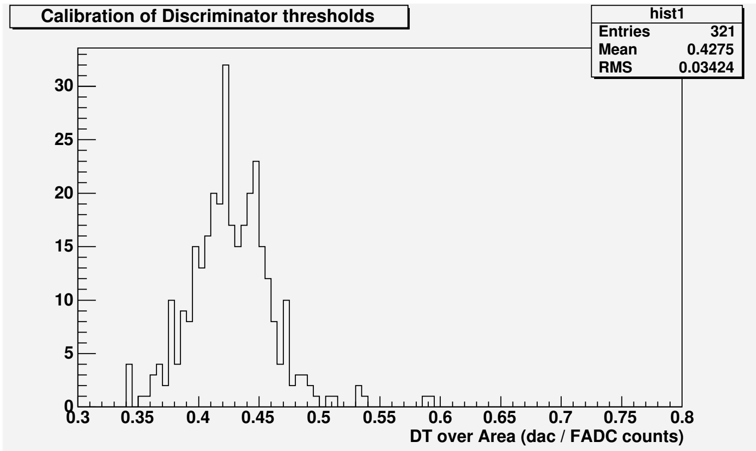

Figure 4.11: *Distribution of $DT_{1/2}$ divided by the charge of the corresponding calibration pulse in ADC counts.*

distribution shows a dispersion of 8%, so part of the dispersion in the distribution of $\mathrm{DT}_{1/e}$ was indeed due to the different channel gains. Instead of using the calibration pulse charge we can use its amplitude. The resulting distribution is centered on 1.14 DAC units per ADC count and has a similar dispersion.

At this point we may consider to use $\mathrm{DT}_{1/2}/\mathrm{Q}_{cal}$ to flatfield the DTs. We must be aware however that the obtained dispersion is not far from the fluctuations in DT(1 MHz) that were measured in the last section (about 3% RMS with the camera at access position and 5% RMS when tracking an extragalactic source). Part of the dispersion in figure 4.11 could be attributed to the fact that the calibration run was taken some minutes after the IPR scan. Actually the IPR scan itself lasts some 10 minutes so it is long enough for the pixel gains to change in a non-negligible way. For some of the pixels this is visible in the IPR scan. The plateau ends and then reappears at a higher DT, while for some others the plateau is simply not flat but a noticeably bumpy.

In conclusion there may be some room to flatfield the DTs by using the values of $\mathrm{DT}_{1/2}/\mathrm{Q}_{cal}$ that were obtained above, but the efficiency of the method is limited by the fluctations in the channel gains.

4.4 Discriminator thresholds in photoelectrons

In the last section we have found out that, in average over the whole camera, 0.43 DAC units in the DT correspond to 1 ADC count integrated charge or 0.38 ADC counts charge amplitude. Now we can use the conversion factor from ADC counts to photoelectrons that is obtained using the F-Factor method to estimate the DT in phe: we will use 7.8 ADC counts per phe like in chapter 3 (from [7]).

The conclusion is that:

1 DAC unit in DT
= 2.32 ADC counts in integrated charge
= 0.9 ADC counts in charge amplitude
= 0.30 phe in integrated charge

For an extragalactic source we are right now using DT$\sim$32 DAC units with 4 next-neighbour trigger multiplicity, which corresponds to 9.6 phe integrated charge. These DT were set so that the rate of accidental triggers produced by NSB is negligible (i.e. smaller than 10 Hz). For Crab we have to raise the DT to $\sim$40 DAC units on account of the brighter star field. This represents 12 phe integrated charge.

For an extragalactic field-of-view the IPR is around 300 kHz at DT$\sim$32 DAC units. This rate is in good agreement [8] with a simulation that have been performed using the program StarResponse (included in the camera simulation program, version 0.7). The signal induced by NSB was simulated in a time window of 100 μs. For the typical extragalactic NSB rate of 0.13 phe/ns/pixel, 20 accidental triggers were obtained, corresponding to an accidental IPR of 200 kHz. An extreme case of 0.26 phe/ns/pixel was also simulated resulting in 87 triggers or accidental trigger rate of 870 kHz.

Let us now consider how these DTs limit the telescope energy threshold. It is conventional wisdom at TeV energies that γ/hadron discrimination based on the use of Hillas parameters only works above 100 phe. This condition determines what we call the analysis threshold. Given that we require at least 4 pixels to trigger, the smallest shower size that triggers the telescope is 38 phe for an extragalactic source and 48 phe for Crab. To sum up the trigger threshold is 3 times smaller that the analysis threshold in the case of an extragalactic source and 2 times smaller in the case of Crab. Our current trigger is set comfortably below the analysis threshold and there is no need to reduce the discriminator thresholds: even if we were ready to accept an increased rate of accidental triggers, the γ-ray images would contain no useful information to discriminate it from the hadron background.

This of course does not apply for any analysis that is not based on Hillas discrimination, like for instance pulsar timing analysis. For sources for which this kind of special analyses can be applied we could still benefit from reducing the trigger threshold. But we must be aware that accidental triggers would substantially increase the background.

Chapter 5

Global trigger rates

This chapter deals with the global rate of the trigger system. We will examine how this rate depends on the discriminator threshold in the pixels, the NSB in the field of view, the telescope's zenith angle, the atmospheric conditions and the reflector's point spread function. We will try to establish if this rate has been stable for the last years of operation.

5.1 Dependence on the discriminator thresholds

In chapter 4 we have studied the dependence of the IPR on the DT. The IPR is completely dominated by NSB noise, either by direct NSB phe at a DT below $\sim$10 phe or by afterpulses above this DT. Triggers issued by the level 1 (L1) or level 2 (L2) trigger system are based on the coincidence of at least two neighbour pixels in a time window of about 3 ns. By requiring coincidence we strongly reduce triggers generated by NSB.

Figure 5.1 shows how the global L2 trigger rate depends on the DT for different multiplicities: 2, 3, 4 and 5 next-neighbour pixels. The rates were measured while pointing at a low zenith angle to an extragalactic dark patch in May 2004, that is, before the access in summer 2004 that completed the reflector mirror surface and optimized the PSF.

All curves exhibit two branches: a first branch up to about a DT of 40 DAC units where the rate has a steep slope and a second branch at larger DTs which is much less steep. The events in the first branch are accidental triggers due to the NSB. The second branch corresponds to cosmic events and follows a slope that is roughly that of the cosmic ray spectrum.

The DTs must be set to the minumim value for which the global trigger rate is below the maximum DAQ rate (currently about 600 Hz). This generally means that we must avoid high accidental rates. Besides setting the trigger at a point where the slope is steep makes the trigger rate very sensitive to small changes in the accidental rate. We typically set the DTs about 2-3 units above the point

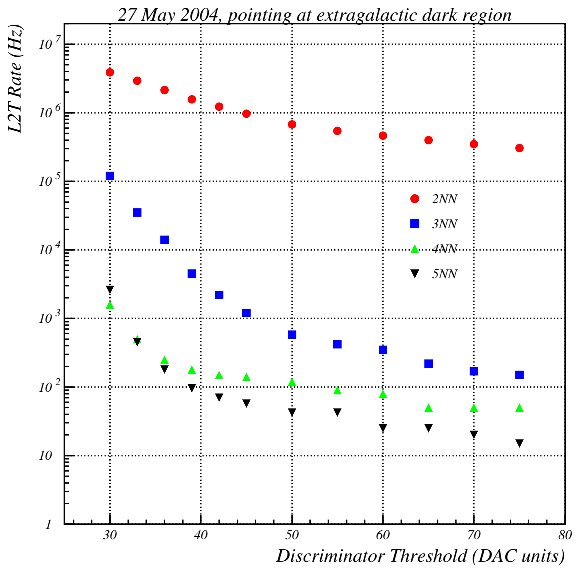

Figure 5.1: *Shown is the dependence of the global trigger rate on the discriminator threshold for different multiplicities of the next-neighbour trigger in May 2004.*

where the two branches join.

For a given DT the rate decreases with the multiplicity. Most of the events in the 2NN and 3NN multiplicities are accidentals, that is, the points in figure 5.1 all correspond to the first branch. The curves for 4NN and 5NN show the two branches: for both multiplicities the transition point is at about 35 DAC units. It has been recently found out that the 5NN was faulty for one of the macrocells. This causes the 5NN rate to increase above the 4NN rate below ∼33 DAC units. All in all only the 4NN curve was reliable at the time and the optimal DT was 35 units for extragalactic positions.

Figure 5.2 shows the L1T, L2T and accidental trigger rates for 4NN multiplicity as a function of the DT. The telescope was pointing to an extragalactic dark region at low zenith angle at a time (last November) when the reflector surface and PSF were already nominal. The smaller the PSF, the more compact the showers and the lower the energy that can trigger the telescope for a fixed DT. In addition a larger reflector means that a shower of a given energy generates more energy and has it easier to trigger. So both effects add up to increase the rate for a fixed DT and reduce the minimum DT. From figure 5.2 and additional tests, we concluded that the optimal value is 32 DAC units for extragalactic and 40 DAC units for galactic units.

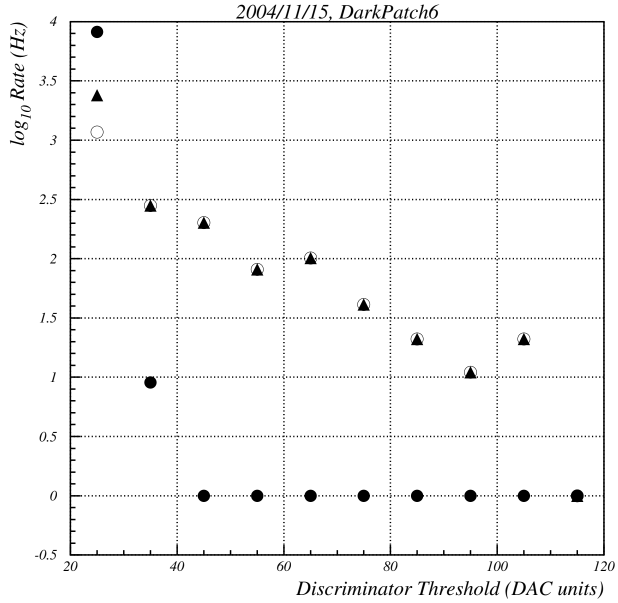

Figure 5.2: *The accidental rate (filled circles), L1T (triangle) and L2T (open circles) versus the discriminator threshold for 4NN multiplicity, as measured in November 2004 when pointing to an extragalactic dark region.*

5.2 Dependence on the zenith angle

In this and the next section we shall consider only the data runs in July 2005 (period 30) which were taken with nominal mirror Point Spread Function. The rates that we shall quote are always the so-called "average rates" in the *.run files. For each data run the rate is calculated as the number of events in the run divided by the run ontime. The ontime is simply the run duration with no correction for dead time. We have always substracted 50 Hz due to interleaved calibration events.

Figure 5.3 shows the average rate as a function of the zenith angle (ZA) for extragalactic sources in period 30. All extragalactic sources are observed with discriminator threshold equal to 32 DAC units. The rate decreases with $\cos^{0.5}$ ZA.

5.3 Stability of the trigger rate

We have studied the stability of the trigger rate for extragalactic sources in period 30. The result is plotted in figure 5.4 for zenith angle below 20°.

The rate is found to be stable within 10% for the whole month. The typical rate close to the zenith is 260 Hz.

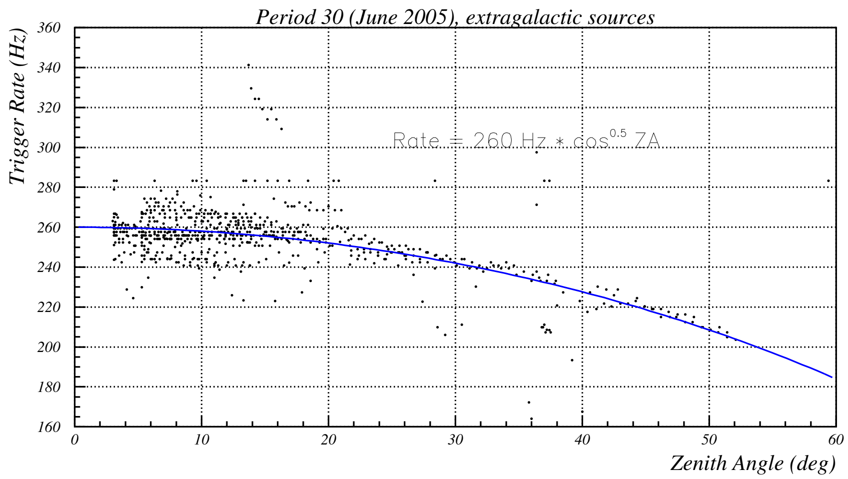

Figure 5.3: *The average rate as a function of the source zenith angle for extragalactic sources in period 30 (June 2005).*

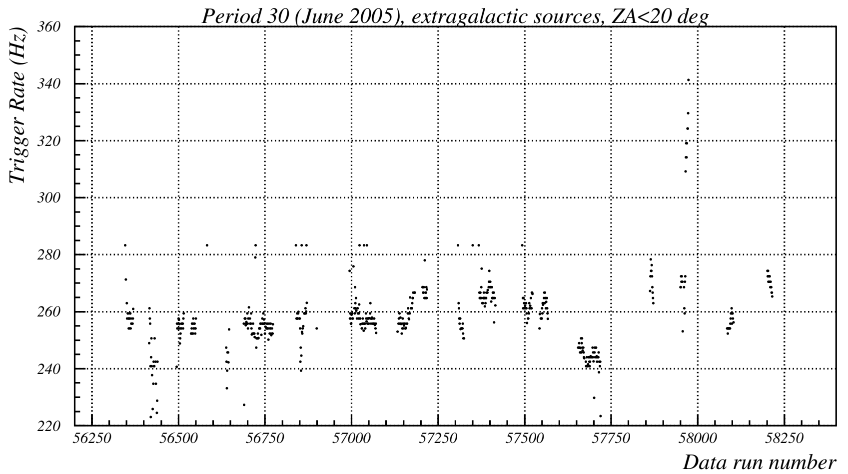

Figure 5.4: *The average rate versus run number for extragalactic sources in period 30 (June 2005) and zenith angle below 20°.*

5.4 Dependence on observation season

Chapter 6

Stability of the electronic gain

We have observed variations in the gain of the electronic chain at very different time scales. To begin with the gain of the optical links changes considerably (in as much as 10-15%) in a matter of minutes. These fluctuations are intrinsic to the lasers that are used for the optical transmission and cannot be reduced. Each individual channel is uncorrelated to the others so the global gain for the whole camera remains unaffected.

The gain of the links also changes in time scales of minutes to hours due to changes in the temperature of the optical transmitters inside the camera. This change is particularly fast at the beginning of the night when the operators switch on the camera shortly before taking data because the temperature inside the camera takes about two hours to reach its nominal value around 35°. Given the fact that the temperature is more or less the same for all the transmitters, the gain in the individual channels evolves coherently with the global gain.

Variations in the gain are also noticeable from night to night. We attribute these long term variations to changes in the voltage of two of the PMT amplification stages, namely the last two stages which are fed by the active load and the 175 V power supply. The output voltage of these two elements jumps in an unpredictable way after several hours or days, and these jumps in turn make the amplification gain of all the PMTs jump coherently.

As we shall see below the study of all these variations is made more difficult by the fact that the output of the calibration box is not stable with the ambient temperature. Since the ambient temperature varies in time scales of minutes to hours, we are forced to use parameters that are independent of the absolute intensity of the calibration pulses for these time scales. This effect affects all pixels equally, so we can average over the whole camera to get rid of it.

6.1 Short term individual pixel fluctuations

Last chapter has made us suspect that the gain in the electronic chain may fluctuate in time scales of a few minutes. We can monitor the stability of the gain directly by using calibration light pulses of a fixed intensity.

We have taken calibration pulses interlaced with cosmic events. The calibration was made with the calibration script "10Led_UV_train50Hz" that flashes 10 UV LEDs on the camera with 50 Hz frequency. The telescope was pointing at an extragalactic position (Mrk 421) at around 33-38 zenith angle. The corresponding data runs are 45472-45476. A pedestal run taken inmediately before these data runs was used to substract the pedestal for all the calibration events. These were separated from the cosmic events by requiring a large charge in most of the pixels.

We integrate the 14 first high gain FADC slices to calculate the charge of each event. Then we substract the pedestal mean that is calculated out of the pedestal run using the same number of slices. Every ten seconds (500 calibration events) we fit the distribution of charge in each pixel to a gaussian to calculate the mean and the sigma. We can calculate the mean number of photoelectrons using the so-called F-factor method:

$$N_{phe} = (1.15\cdot < Q > /\sigma_Q^{red})^2 \tag{6.1}$$

where <Q> is the mean charge and the sigma of the pedestal has been substracted quadratically from the sigma of the charge distribution to calculate the "reduced sigma" σ_Q^{red}.

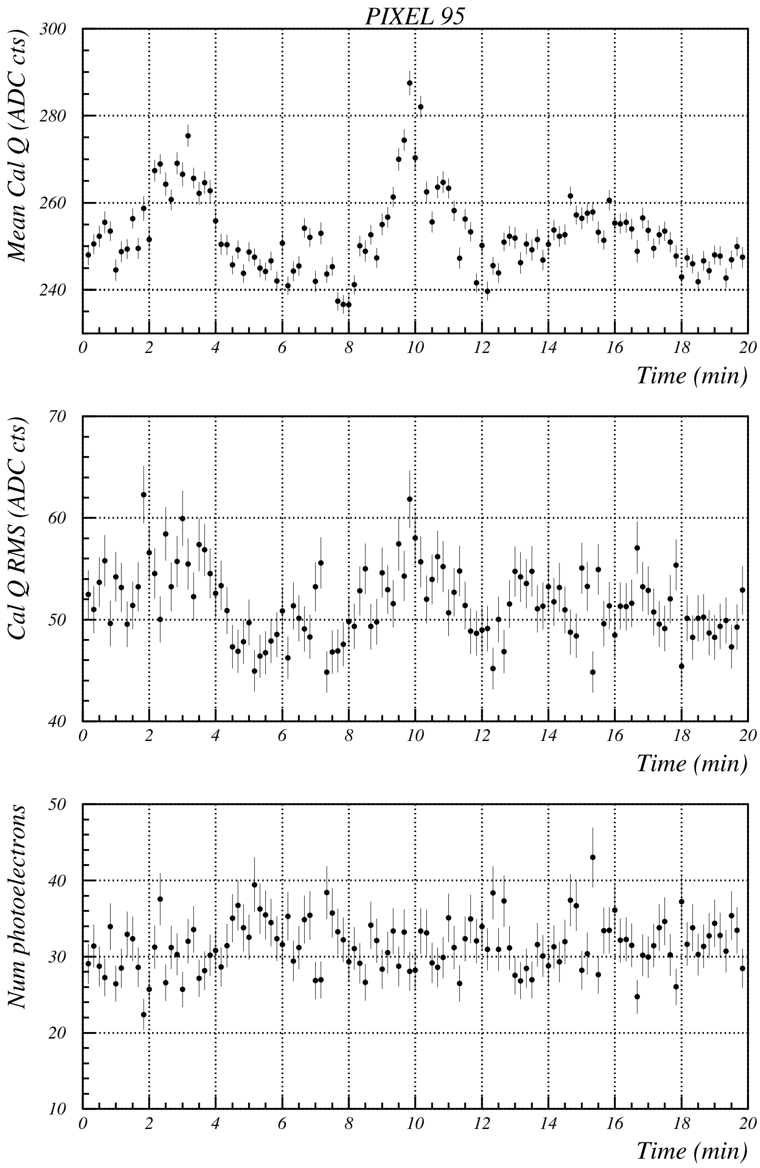

Figure 3.0: *Shown is the evolution of the mean calibration charge, the sigma of the charge distribution and the number of photoelectrons with time for runs 45472-45476 and pixel hw 95.*

Figure 3.0 shows the evolution of the mean charge, the sigma of the gaussian distribution and the number of photoelectrons with time for pixel 95. This pixel displays a behaviour that is common to most of the pixels in the camera: the mean charge drifts in a matter of 2-3 minutes in as much as a 10-20% while the number of photoelectrons stays constant within the errors.

Different pixels display different fluctuations. Figure 6.1 shows again the evolution of the mean calibration charge for other four pixels. The charge seems

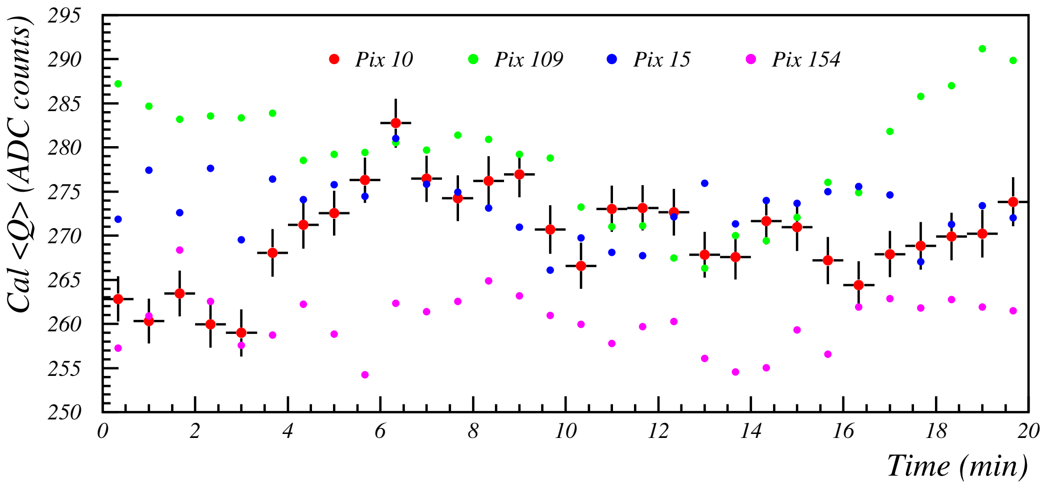

Figure 6.1: *Shown is the evolution of the mean calibration charge with time for several pixels selected at random. The error bars are only plotted for one of the pixels to avoid confusion. Their size is generic of the error in all the other pixels.*

to fluctuate independently in the different pixels, both for the pixels in the plot and for the others in the camera, but we have not looked systematically for correlations.

We have made twenty 1-min time bins with the full sample and made a distribution with the mean charges (<Q>) in each time bin. Figure 6.2 shows the RMS and peak-to-peak amplitude of this dfistribution for all the pixels in the camera (relative to the mean of the distribution). With the exception of a few pixels with large amplitudes, for most of the camera <Q> fluctuates at most in a 10% and the RMS is generally under 3%.

We can compare the evolution of the mean charge with the evolution of the individual pixel rate. This is done in figure 6.3 for the same pixel considered above. The shape of the curve is remarkably similar to the shape of the charge evolution. The same happens for all pixels in the camera: a change in the gain is always correlated to a change in the IPR. This agrees with the conclusions of the last chapter.

The IPR is not linearly correlated with the calibration mean charge though, or even with the logarithm of the mean charge. And the correlation depends on the pixel too: for instance an increase in the charge of 10% may be associated to an increase in IPR ranging from 25% (like in pixel 116) to 100% (in pixel 154).

The change is gain could be attributed to any element in the electronic chain, starting at the PMT amplification system, the preamplifier at the PMT base, the gain in the optical transmission system or the gain in the high gain branch amplifier.

We can use the PMT anode currents to check if the gain in the PMT has

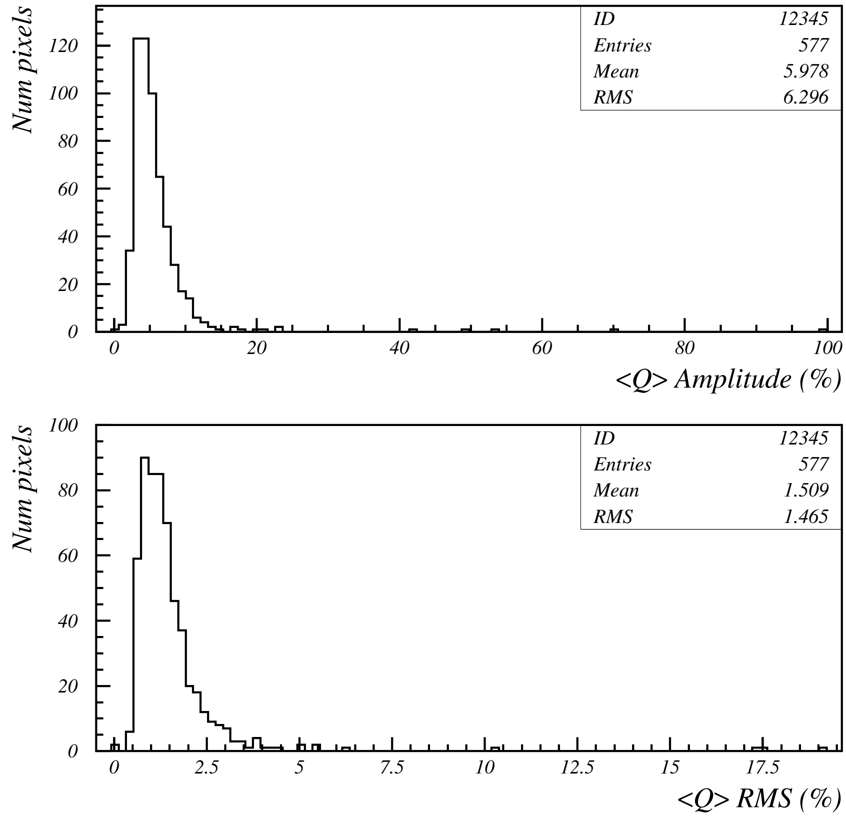

Figure 6.2: *Distribution of RMS and amplitude maximum fluctuation of* $<Q>$ *for runs 45472-45476 and all the pixels in the camera. Both are expressed relative to the mean* $<Q>$ *for the whole sample (in percentage).*

changed. Since each pixel is illuminated with a roughly constant level of light coming from the NSB (only affected in some pixels by dim stars in the field of view), we would expect that the anode current stays constant during the time period under study. but most of the pixels in the camera show the behaviour of pixel 95 in the bottom panel of figure 6.3: a constant decrease of ∼5%. The average DC over the whole camera follows the same trend, including the small "bumps" that are observed at minutes 5, 9 and 13. (This general decrease in DC must be caused by a factor external to the camera. It cannot be due to an increased light attenuation in the atmosphere due to an increase in the zenith angle since it in fact decreases during the observation period, but it could be easily caused by a fluctuation in the atmospheric conditions).

We can conclude that for a given pixel there is no correlation between the fluctuations in the calibration charge or the IPR and the anode currents, hence the fluctuations in global gain cannot be attributed to fluctuations in the PMT gain. Again we are forced to conclude that what varies is the gain in the optical transmission system.

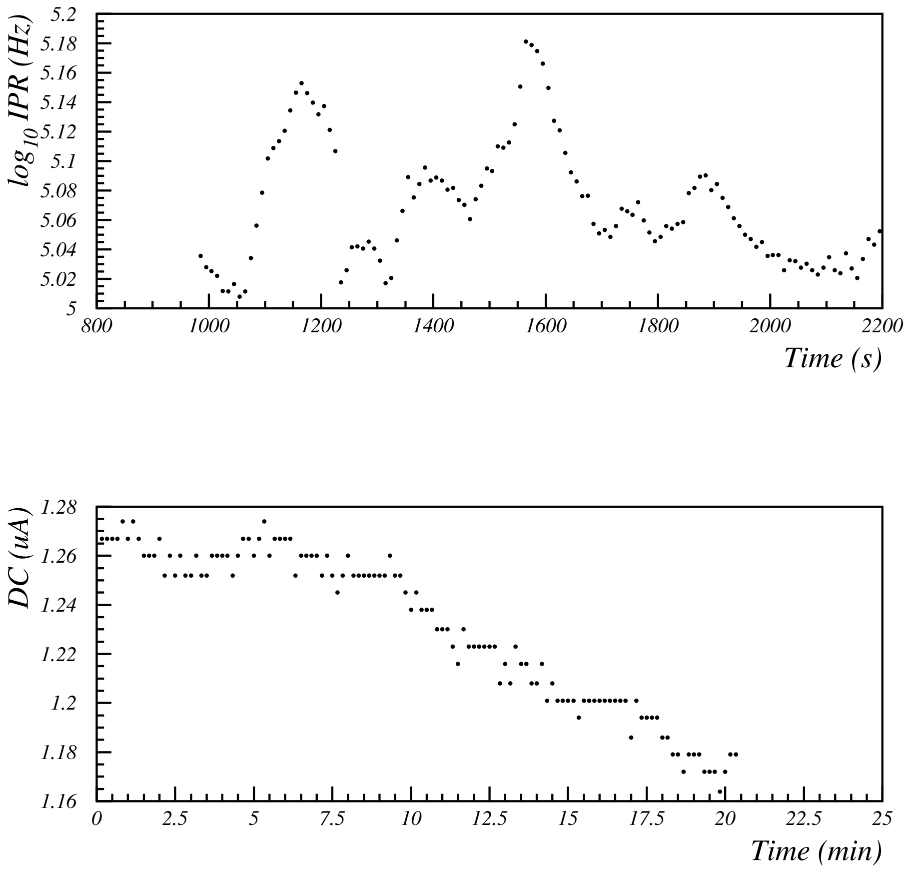

Figure 6.3: *Evolution of the individual pixel rate with time (top) and evolution of anode current with time (bottom) for pixel 95. The time range is the same as for the other figures.*

6.2 Effect of short term fluctuations on the rate and the shower images

As illustrated in last chapter's figure 4.6, the changes of IPR of the invididual pixels are uncorrelated. The average gain in the camera actually stays constant over time. This is obvious when we monitor the evolution with time of the average of the calibration charge in an event over the whole camera or the level 2 total trigger rate. The latter depends only on the zenith angle over the above considered time period.

What is not to say that showers are not affected. Since the pixel gains change in time scales of several minutes but right now we do not recalibrate our data so fast, the charge distribution in a shower is distorted by this effect and the Hillas parameters are affected. This is especially true at low energies where the number of pixels in a shower is small and the pixel gain fluctuations do not average out.

Since the discriminator thresholds stay at a constant level and the pixel gains change, the trigger sensitivity in the camera is also affected. Regions of the camera where the gain decreases will have a higher energy threshold and viceversa, so we can expect that the spatial distribution of showers in the camera fluctuates with time. This is probably a minor effect though, since we generally require at least four pixels to trigger our telescope and that averages out strong fluctuations, but may be relevant for smaller multiplicities.

We can extract a last conclusion regarding the use of interlaced calibration events. The last plot in figure 3.0 makes clear that it is not possible to calculate the number of photoelectrons using the F-factor method with only 500 events, the reason being that the relative error in the number of photoelectrons is roughly twice as large as the relative error in the sigma of the charge distribution and this error is almost 10% for this pulse intensity. That makes the relative error in the number of photoelectrons and the conversion factor from ADC counts to photoelectrons around 20%. It is not possible to group the events in longer time bins because the first plot of the same figure shows that gain fluctuations can be as fast as 10-20 seconds. Adding together events that come from charge distributions with different means distorts the global charge distribution and make the calculation of the sigma impossible. Hence the F-factor method cannot be used with a calibration event frequency of 50 Hz. This is however not a problem since we can still intercalibrate all pixels in time scales of 10-20 seconds using the charge means.

6.3 Stability of the calibration box

Let us now look into the stability of the light yield of the calibration box. Even if the gain in the individual pixels fluctuate, these fluctuations are expected to be uncorrelated. Let us assume that the global gain suffers from no other variations. The average charge over the whole camera or large fractions of the pixels is expected to be correlated with the light output of the calibration box.

In figure 6.4 we show the average charge in ADC counts for the inner and outer pixels as a function of the external temperature and all the data runs taken in May 2005. The charge was calculated from interleaved 10Led_UV calibration events. The external temperature is measured at the telescope site, far away from the camera. Please note that the readout of this temperature is sometimes wrong and results in a temperature that is too low by 30%. This explains why there are two "branches" in the correlation between both parameters, one of them with only a few points that mirrors the main branch.

The external temperature has been found to have the strongest effect on the

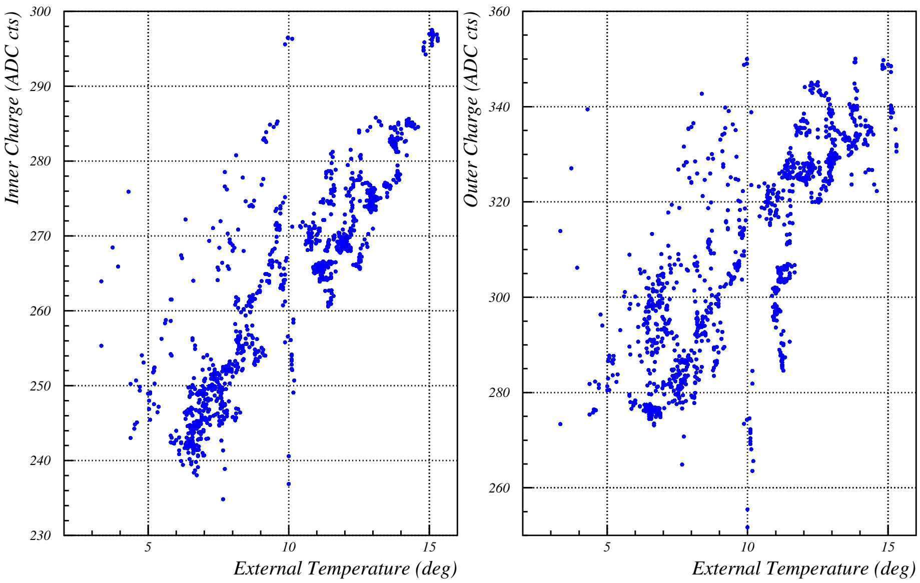

Figure 6.4: *The average charge in ADC counts for the inner (top) and outer pixels (bottom) as a function of the ambient temperature. The data correspond to May 2005.*

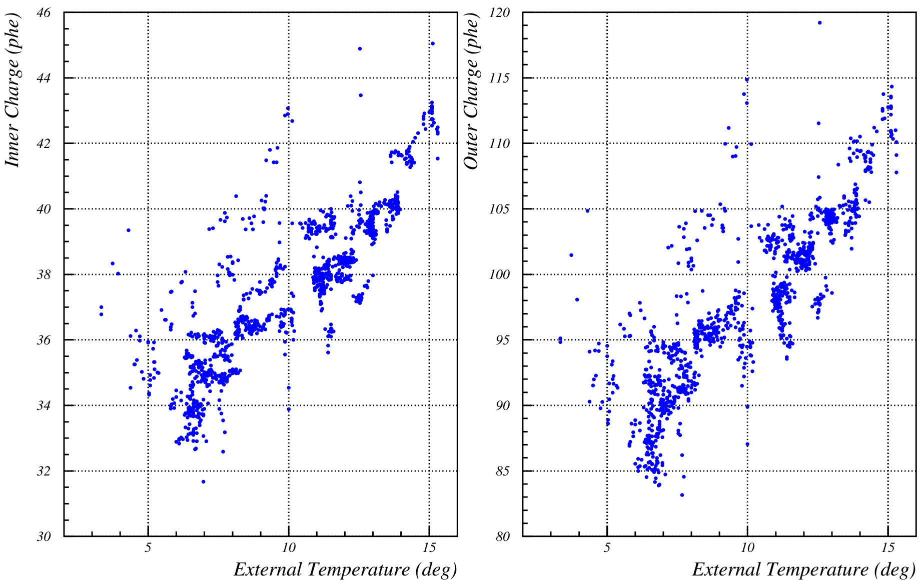

Figure 6.5: *The average charge in photoelectrons for the inner (top) and outer pixels (bottom) as a function of the ambient temperature. The data correspond to May 2005.*

light yield of the calibration box. The charge in the inner pixels grows from 240 to 295 ADC counts as the external temperature goes from 6° to 16°. This corresponds to an increase about 2.3% per degree. For the inner pixels the average charge increases from 275 to 355 ADC counts in the same range of temperatures, that is, 2.9% per degree. Within the uncertainties the increase per degree is the same for both inner and outer pixels.

The number of photoelectrons can be calculated using the F-Factor method (equation 6.1). They have been plotted as a function of the external temperature in figure 6.5. The number of photoelectrons increases from 33.5 phe to 43 phe in the inner camera as the temperature increases from 6° to 16°. This is 2.9% per degree. For the outer camera, the number of photoelectrons grows from 87 to 112 in the same range of temperatures, or 2.9% per degree. The increase per degree is the same for the inner and the outer camera, so we can conclude that the effect is due to a change in the amount of light that illuminates the camera and not to a change in the electronic gain.

The reason for this correlation with the external temperature remains unknown. In principle there should be no electronic component in the calibration box with such a strong dependence. The stability of the LEDs under temperature variations have been studied in [5]. The light yield was observed to **decrease** in less than 10% when reducing the temperature from 0° to 50°C, or less than 0.2% per degree.

6.4 Long term variation of the individual pixels

We are now interested on the gain variations of the different pixels over a period of days, that is, we would like to extend the study of first section of this chapter to longer time scales. Given the fact that the output of the calibration box is not stable over these scales, it is mandatory to normalize the charges in the pixels to the average charge over the inner or the outer camera.

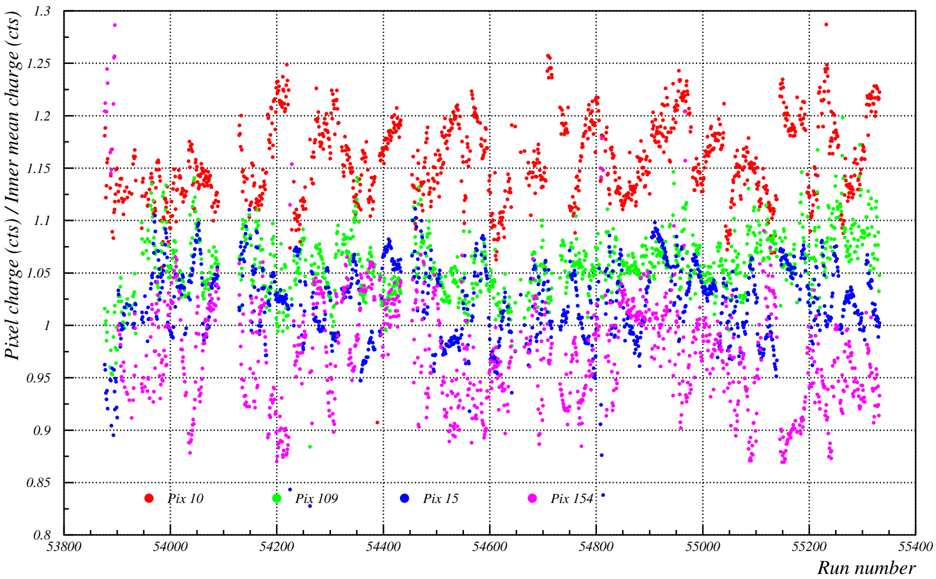

Figure 6.6: *Evolution of the average charge in ADC counts for some particular inner pixels. The charge has been normalized to the average charge in the run for the whole inner camera to suppress the variations of the calibration light. The charge of pixel 10 has been multiplied by 1.15 for clarity. The data runs stem from May 2005.*

Figure 6.6 illustrates the evolution of the charge for some particular pixels. The charge is calculated as the mean charge in the interleaved calibration events in a data run. It has been normalized by the average over the whole inner camera. The observed variations are similar to those described in section 6.1. Over one full month the gain fluctuates in as much as 15%. The fluctuations in the different pixels seem to be uncorrelated.

Figure 6.7 shows the same for some outer pixels. The pixels have been selected to cover a range of high voltages (pixels 400, 401, 402, 413 and 414 are set to respectively 1050 V, 1042 V, 1056 V, 990 V and 1009 V). The charges display somehow larger fluctuations, up to 20% over the whole month.

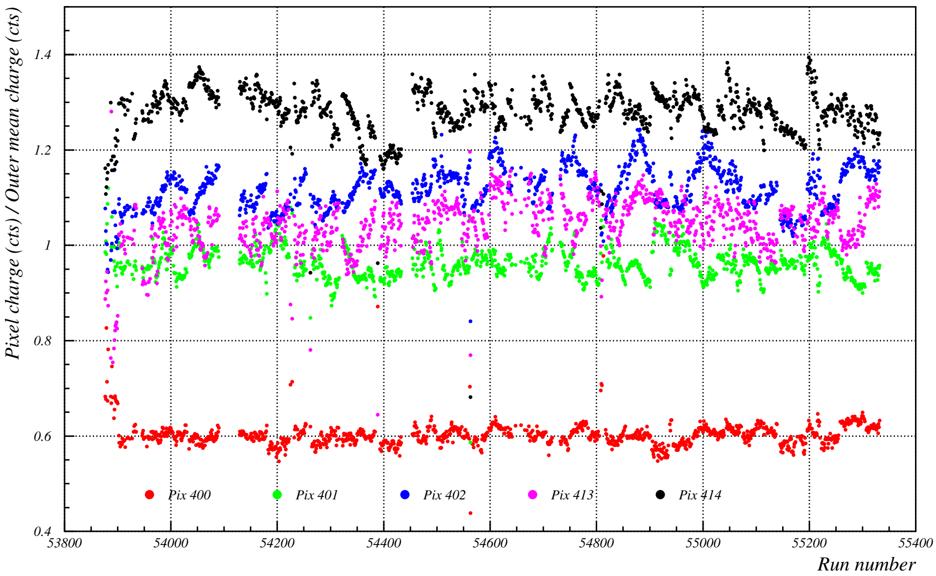

Figure 6.7: *Evolution of the average charge in ADC counts for some particular outer pixels. The charge has been normalized to the average charge in the run for the whole inner camera to suppress the variations of the calibration light. The data runs stem from May 2005.*

6.5 Dependence on the link temperature

One of the most obvious sources of variations in the global gain of the camera over periods of minutes to hours has been found to be the temperature at the optical links. It is known that a higher temperature results in a lower gain in VCSELs. This is what we also observe in the data.

Since the charge of the calibration events that we measure at the FADC depends on the output of the calibration box and we know that this changes, we need to look at the gain itself using the conversion factor from number of photoelectrons to ADC counts. We illustrate the behaviour of the conversion factor in the outer pixels and the temperature at the optical link along a typical night in figure 6.8. These data were taken on 2005_04_11, a night when the camera was switched on not long before starting datataking. The number of photoelectrons was obtained using the F-Factor method over interleaved 10Led_UV calibration events. Each point in the figure corresponds to a data run. The camera had not reached thermal equilibrium and the first runs were taken while the temperature was still increasing. As the temperature goes up until it stabilizes at 35° the gain in the outer pixels goes down by 20%.

The average conversion factor is plotted in figure 6.9 for inner and outer

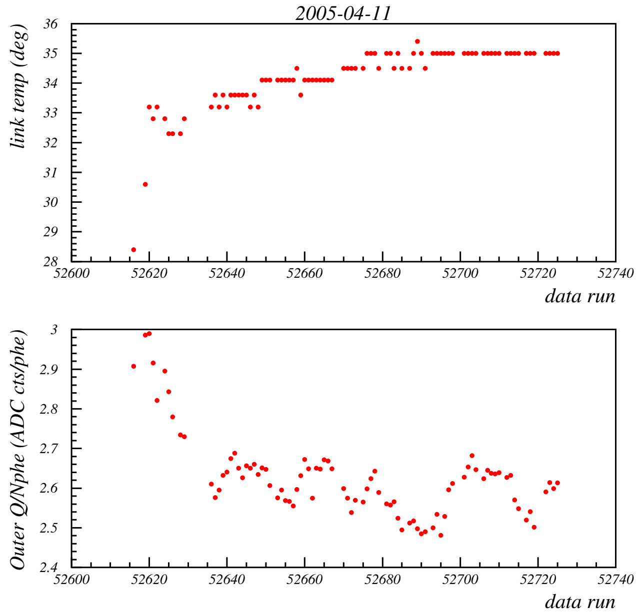

Figure 6.8: *Top: Temperature at the optical links versus data run number. Bottom: Ratio of charge in ADC counts and number of photoelectrons (as determined using the F-Factor method) for the outer pixels also versus data run number. The data corresponds to the night of 2005_04_11.*

pixels separately as a function of the temperature at the optical transmitters, for another night with a similar behaviour (2005_04_08). The correlation with the temperature is clear over the whole range for both types of pixels. The gain decreases in 12% in a range of 12°, what is to say, in about 1.0% per degree. Since the effect is common to all the pixels in the camera and the gain in the VCSELs is expected to behave in a similar way, we adscribe this effect to the optical transmission system. This also agrees with the fact that no comparable change is observed in the anode currents, i.e., in the PMT gains.

Figure 6.9 corresponds to a night when the camera was switched on only half an hour before datataking. Since the day was cold and the camera had been in thermal equilibrium with its external environment, this means that it took around two hours for its temperature to reach a stable level when all the electronics were switched on. As a consequence the data were taken in a rather wide range of temperatures. In addition the temperature increased rather fast during the first one-two hours and that made the gain also change very fast. This is generally not the case when the camera is switched on two hours before datataking. In this event the temperature inside the camera during the datataking period drifts slowly in a maximum range of about 5° for the whole night, so the maximum expected variation in the gain is about 6% in 8 to 10 hours.

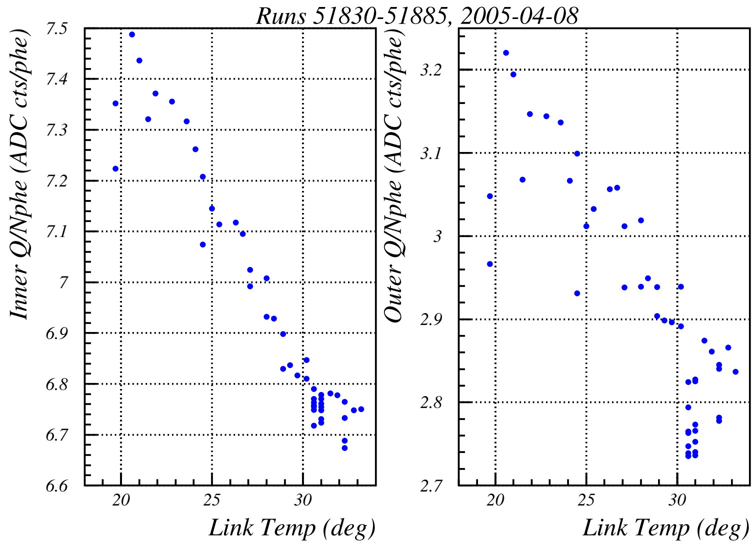

Figure 6.9: *Ratio of charge in ADC counts and number of photoelectrons (as determined using the F-Factor method) for inner (left) and outer (right) pixels, plotted as a function of the temperature at the optical links. Each point correspond to a data run taken during the night of 2005_04_08.*

However it has to be noted that the range of exact temperatures depends on the ambient temperature, because the camera is not perfectly isolated. The average camera temperature can change in as much as 5° from a cold to a warm night. This introduces unavoidable drifts in the global gain of the order of 5% from night to night which can only be reduced by stabilizing the camera to a constant temperature along the whole year.

6.6 Dependence on the active load and 175V power supply voltages

Long term variations in the gain are not only associated to changes in the external temperature or the temperature at the optical links. Another parameter that influences the gain is the voltage at the different amplification stages of the PMT (see chapter 2 for a description of the HV system at the base of the PMT). In particular we have found out that tha gain is very sensitive to the voltage that is applied between dynode 5 (D5) and dynode 6 (D6). This voltage is controlled by the so-called active load which sets the voltage between D5 and the anode and a 175V power supply which sets the voltage between D6 and the anode.

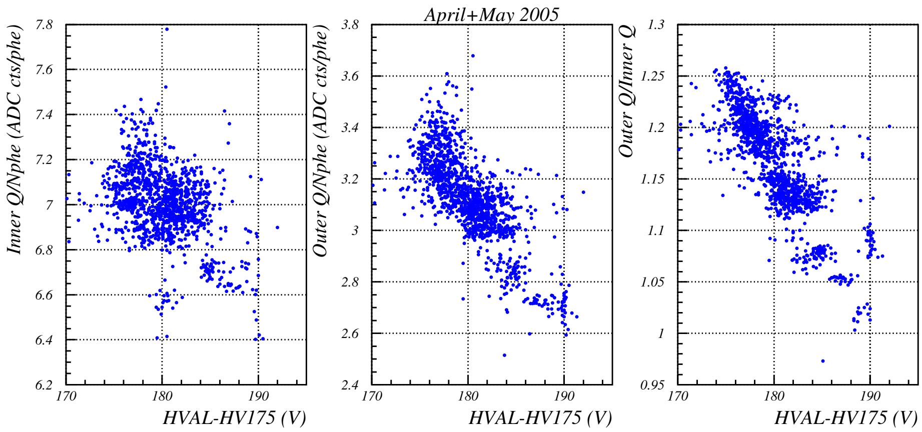

Figure 6.10: *Ratio of charge in ADC counts and number of photoelectrons for inner (left panel) and outer (central panel) pixels, plotted as a function of the voltage drop between D5 and D6. This voltage drop is determined by the voltage at the active load (HVAL) and the voltage at the 175V power supply (HV175). The rightmost panel shows the ratio of the mean calibration charge in the outer and the inner pixels as a function of the same voltage. Each point correspond to a data run in April or May 2005.*

Figure 6.10 shows the conversion factor from charge in the FADC to number of phe, that is the system gain, for inner and outer pixels as a function of the voltage drop between D5 and D6. Only a small dependence is visible for the inner pixels, while the gain in the outer decreases by about 20% as voltage grows in 15 V. This means that the ratio of the charge in the inner and the outer pixels also decreases by 20% in the same range of voltages.

Since the source of the variations is the PMT, the anode currents (DC) must change coherently. However the DCs depend strongly on the zenith angle, atmospheric transmission and star field (that is, the external light background is difficult to use as a calibration source because it is strongly variable). The first

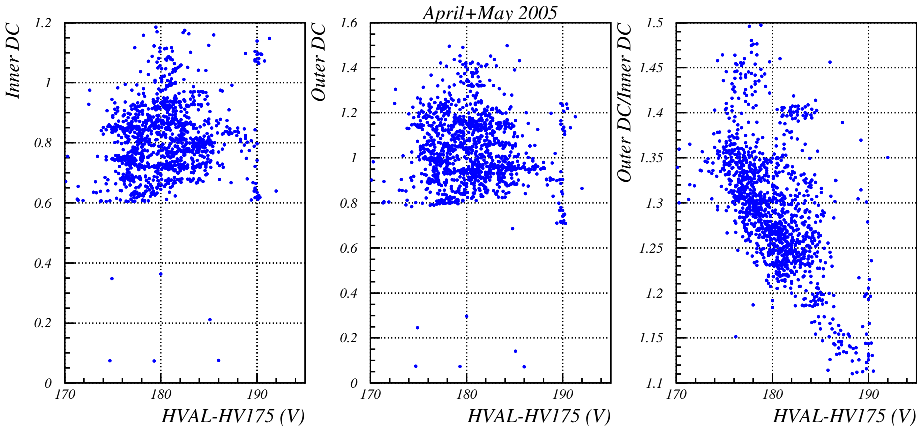

Figure 6.11: *DC in the inner (left panel) and outer (central panel) pixels, plotted as a function of the voltage drop between D5 and D6. The rightmost panel shows the ratio of the mean DC in the outer and the inner pixels as a function of the same voltage. Each point correspond to a data run in April or May 2005.*

two effects are global to all the pixels in the camera, so we can expect that the ratio of the DC in the inner and outer pixels still depends on the voltage drop between D5 and D6. This is indeed the case, as illustrated in figure 6.11. Whereas the DCs themselves do not show any correlation with the voltage, the ratio of the DCs does, in the same amount as the ratio of charges. The correlation is not as good as for the charges because the starlight can still bias the ratio of DCs. For instance the inner pixels may have in the average a higher DC than the outer due to some star in the outer camera.

Actually we can represent the ratio of DC as a function of the ratio of calibration charges to test if the variations are indeed correlated run by run. Figure 6.12 shows that this is the case, even if the correlation is not very tight probably due to inhomogenities in the starfields. Anyway the correlation strengthens the case that the effect stems from the PMTs and not from the optical transmission system.

The fact that this effect mostly affects the inner pixels and these are the only pixels in the trigger area explains why we do not observe a strong variation in the trigger rate.

It is difficult to understand this effect. To begin with, the change in gain is about 20% for a change in voltage of only ∼10%. In addition the gain decreases when the voltage increases, contrary to what we would expect: an increased voltage should increase the amplification gain in the corresponding stage almost linearly. Furthermore we have also found out that the gain does not depend on the voltage drop between D6 and the anode, that is set directly using the 175V power supply. We would expect a similar dependence of the gain on this voltage

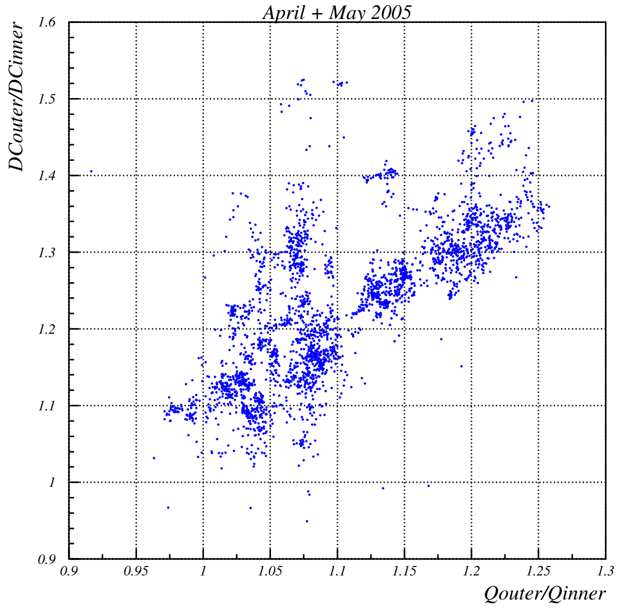

Figure 6.12: *Ratio of DC in the inner and outer pixels as a function of ratio of calibration charges. Each point correspond to a data run in April or May 2005.*

drop.

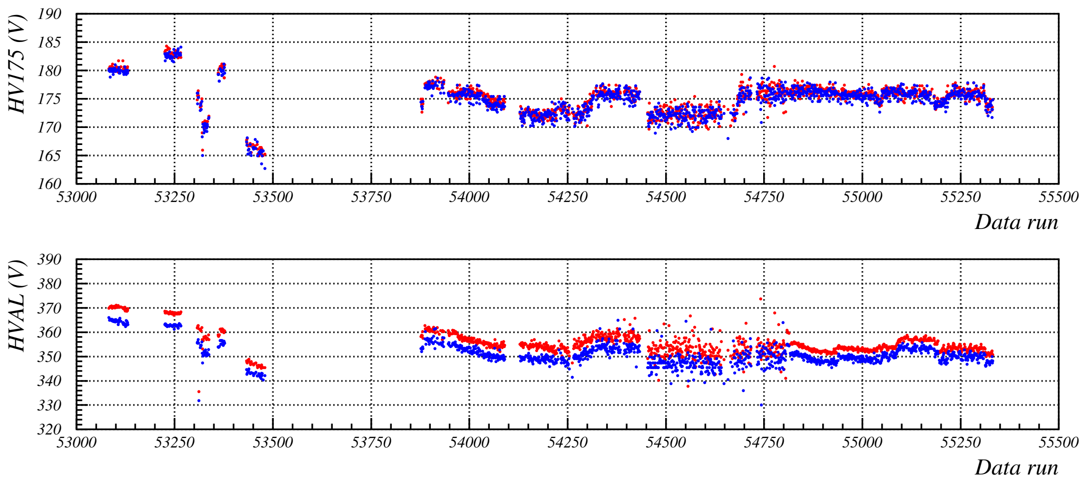

Figure 6.13: *Evolution of the voltage at the 175V power supply (top) and the active load (bottom). Red corresponds to side A of the camera and blue to side B.*

Notwithstanding its cause this effect remains as one of the most important at long time scales. Figure 6.13 shows how the voltage at the active load and at the 175V power supply evolved with time during April and May 2005. The voltage is displayed separately for the two sides of the camera (see chapter 2 for a definition of side A and B). The voltage can jump rather fast (in a matter of seconds) in as much as 5 V for the 175V power supply and 10 V for the active load. Both sides of the camera are correlated, while the active load and the 175V supply are not. Every time the voltage jumps the gain of the outer PMTs jumps too, by as much as 5 to 10%. These jumps are unpredictable. We have found no correlation with any other parameter, like ambient temperature, humidity or current/voltage in the main HV power supply. The HV provided by the main supply is particulary stable.

Chapter 7

Anode currents (DC)

In this chapter we study the PMT anode currents (from now on “DC”). During normal datataking the pixels are exposed to photons coming from the sky, either diffuse photons (Night Sky Background) or photons originating on particular stars in the camera FOV. These photons constitute the main background for the detection of atmpsheric showers, so the DCs are a useful tool to understand the background. Our intention is firstly to intercalibrate the DCs in the pixels as a first step to produce photon flux maps of the camera starfield, and secondly to investigate the correlation between the DC and the pedestal RMS to understand if both observables provide comparable estimates of the background.

For each pixel the DC is measured directly at the base of the PMT using an ADC in an integration window of a few μs. It is sampled with $\sim$3 Hz frequency and saved to a control ascii file regularly during data taking.

7.1 DCs for typical fields of view

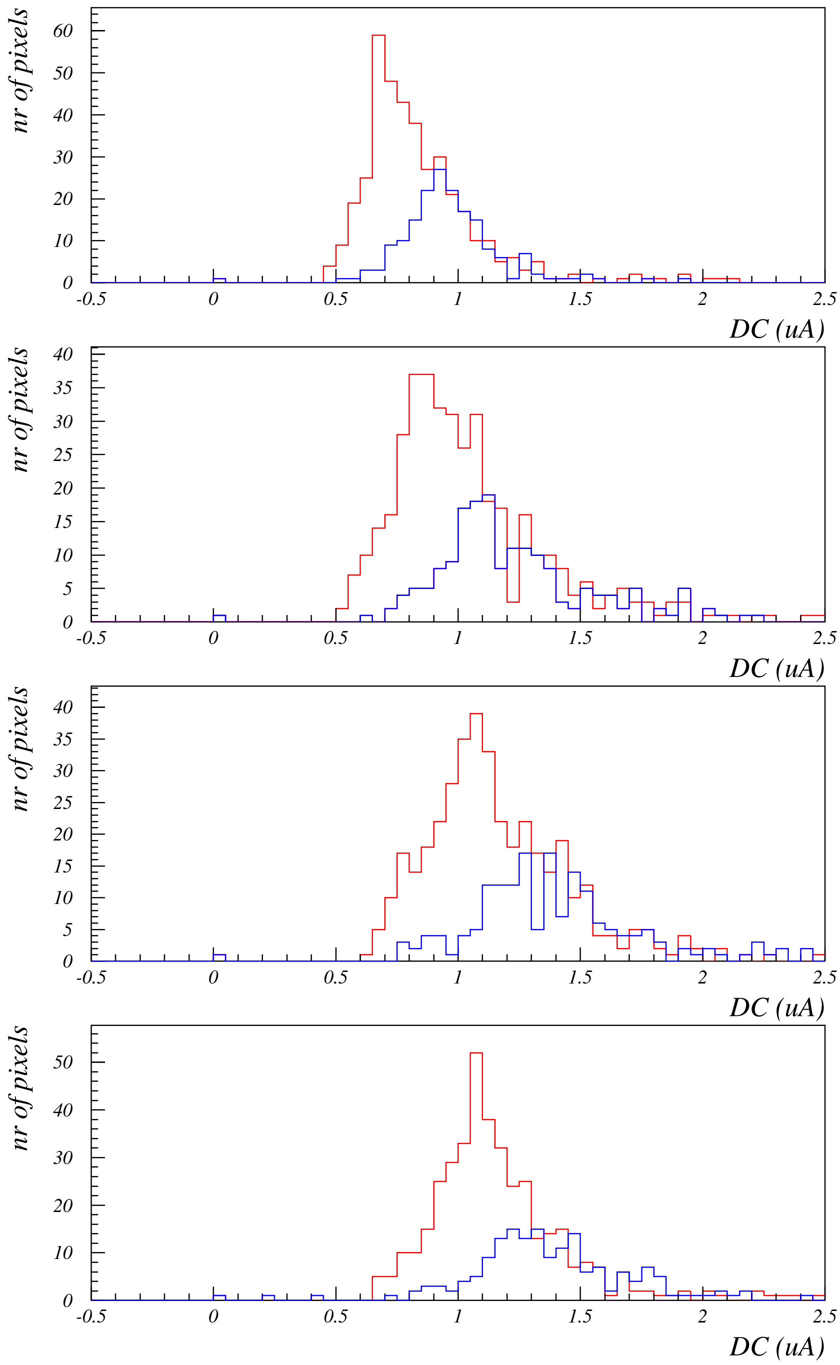

Figure 4.0: *DCs for four fields of view in inner (red) and outer (blue) pixel, all of them at low zenith angle. The first panel corresponds to an extragalactic source, 3C66a. The other three are galactic positions: the second is 3EG 2033 (unidentified HEGRA source in the Cygnus region), the third is PSR 1951 and the fourth is the Crab Nebula.*

Figure 4.0 shows the distribution of DCs for several fields of view that have been observed with the telescope. The first plot correspond to a typical extragalactic position with no bright stars. The DCs are typically under 1 μA in the inner pixels and slightly higher in the outer camera. They rarely exceed 1.5 μA.

The last three plots correspond to galactic positions. The background light is always higher but changes strongly from field to field, mostly depending on galactic latitude. It can range from an average over the whole camera around 1.0 μA for a relatively dark field of view like 3EG 2033 to around 1.3 μA for a bright field of view like Crab. The latter is about 50% higher than the typical value for an extragalactic source. As we will see below, the DC is directly proportional to the square of the pedestal RMS, so a source like Crab is expected to exhibit about 20% higher pedestal RMS than an extragalactic source.

7.2 Pixel intercalibration

The DC is given by:

$$DC = I(photons) \cdot CE_{WC} \cdot QE \cdot CE_{PMT} \cdot G_{PMT} = N_{phe}/s \cdot G_{PMT} \qquad (7.1)$$

where I is the photon intensity on top of the winston cone, CE_{WC} is the photon collection efficiency of the winston cone, QE is the PMT quantum efficiency, CE_{PMT} is the photoelectron collection efficiency, G_{PMT} is the amplification in the PMT dynode system and Nphe/s are the number of photoelectrons that are collected every second in the first dynode.

Assuming a constant illumination on all the pixels, the difference from pixel to pixel obeys to a difference in the last 4 factors, normally dominated by the PMT gain.

The first plot in Fig. 0.0 corresponds to an extragalactic source where the distribution of background light is expected to be rather flat. If we assume that all the pixels are indeed exposed to a constant intensity, the differences in gain are in the order of 30% RMS.

We have to correct for these strong variations if we want to extract a map of the background light. We can do so by using the continuous light (CL) source in the calibration box. The CL source allows to illuminate the camera homogeneously in a range of light intensities (0 to 255 in arbitrary units). The color of the CL can also be selected: ambar, red, green-blue and UV LEDs are available. For this test we have used the green-blue LED. We have pointed the telescope 5° below the horizon level in the direction of the Roque, that is, some 15° below the actual horizon. The camera is however not completely dark because in this position the pixels look directly into the sky (the light is not reflected on the mirror), but we expect the background light intensity to be lower and more homogeneous.

Then we have measured the DCs for five different intensities of CL and for no CL.

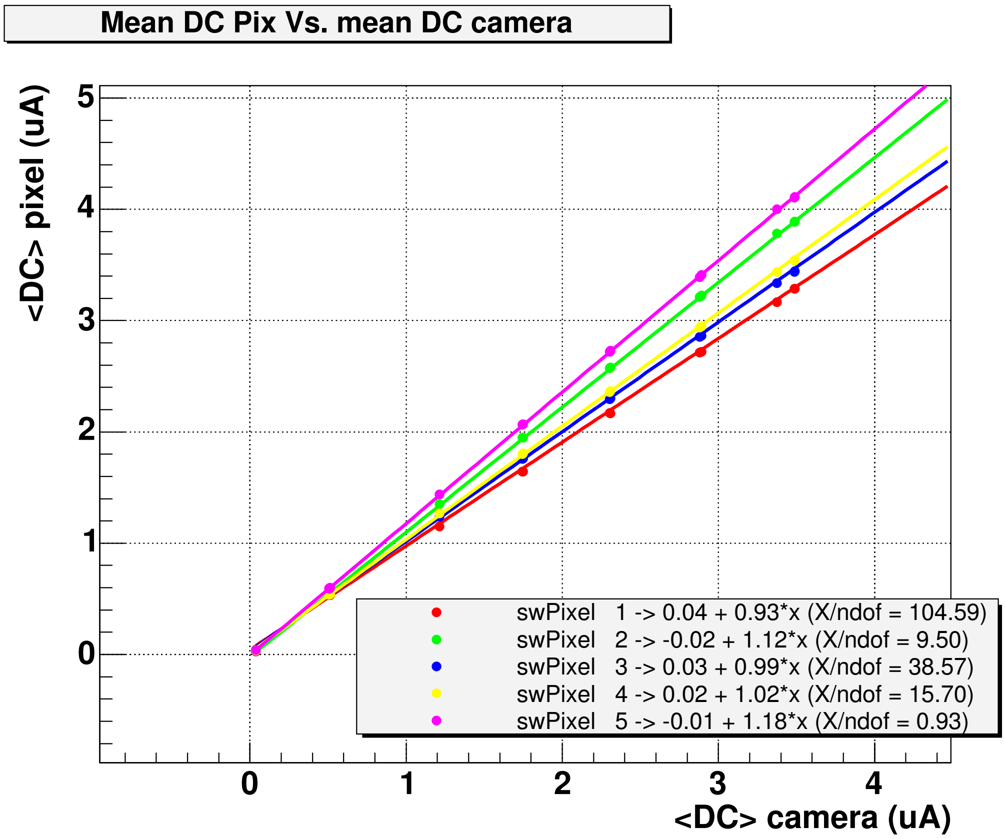

Figure 7.1: *Pixel DC as a function of the mean DC in the whole camera in the first five pixels (hw 2 to 6) for six levels of CL, CL switched off and closed camera.*

The result of the measurements for the first five inner pixels is shown in figure 7.1. The camera was under CL illumination with six different light levels. The CL was switched off (<DC>$\sim$0.5 μA, due to light coming directly from the sky) and then the camera was closed (points close to 0 DC).

All the points could be fitted to a straight line that generally goes through the origin but whose slope depends on the pixel. The fact that the fit is succesful is interesting by itself because the measurements were made in a sequence that lasted for some minutes: we can conclude that, contrary to the behaviour optical links, the PMT response is stable over this time range. We will come back to this issue later in this chapter.

The distribution of slopes for all the pixels is plotted in figure 7.2. The slopes show a spread of 30%, consistent with what we obtained before for the extragalactic field of view. The fit slope can be used to intercalibrate the pixels and obtain a flat DC distribution. The same calibration factor can then be applied to any field of view to extract a map of the background light.

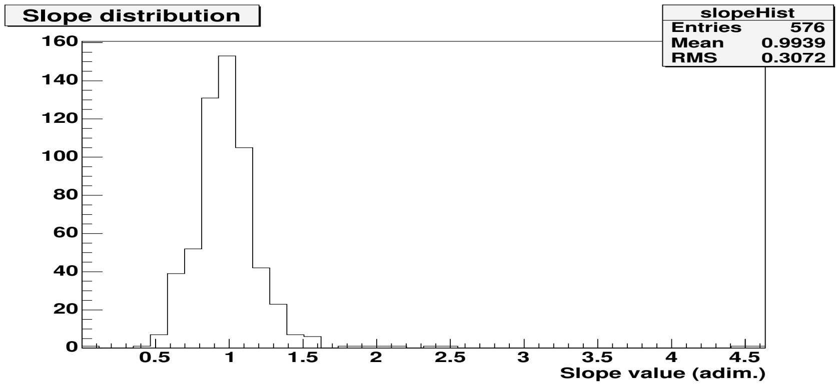

Figure 7.2: *Distribution of slopes obtained in the fit to the pixel DC vs average DC plot illustrated in figure 7.1.*

7.3 Correlation with pedestal RMS

In the first chapter we saw that the NSB and the sta field are the dominant factors in the fluctuation of the pedestal signal registered in the FADCs. The fluctuation of the pedestal (measured with the pedestal RMS) is basically proportional to the fluctuation in the number of photoelectrons N_{phe}. The charge per unit of time that is measured at the FADCs $Q/$s is:

$$Q/s \propto N_{phe}/s \cdot G_{PMT} \cdot G_{preamp} \cdot G_{link} \tag{7.2}$$

where G_{preamp} is the gain of the preamplifier in the PMT base and G_{link} is the gain of the optical transmission system. From this equation and eq. 7.1, we conclude that the pedestal RMS is proportional to the square root of the DC. The proportionality factor however depends on the pixel, and more precisely on G_{link}.

The correlation between pedestal RMS and the square root of the DC is illustrated for five pixels in figure 7.3. The points correspond to pedestal runs that were taken for the different levels of CL that we described in the last section. The CL was increased and subsequently decreased, so we could measure the pedestal RMS and DC while going up and down in the cycle, at slightly different times. Both points are represented in the plot and it is evident that the pedestal RMS does not stay constant while the DC does. This is again due to the fluctuations of the optical link gain, that enter the pedestal RMS but not the DC. The additional point close to the origin was taken with closed camera and agrees nicely with the extrapolation of the other five points.

The slope of the fit depends on the gain of the optical transmission system. The slope distribution for all the pixels in the inner and outer camera is shown in figure 7.4. The slope is noticeably smaller in the outer camera. This is because the pixels and the number of photoelectrons are larger for the same light density in the outer pixels. More photoelectrons mean a smaller relative fluctuation by a

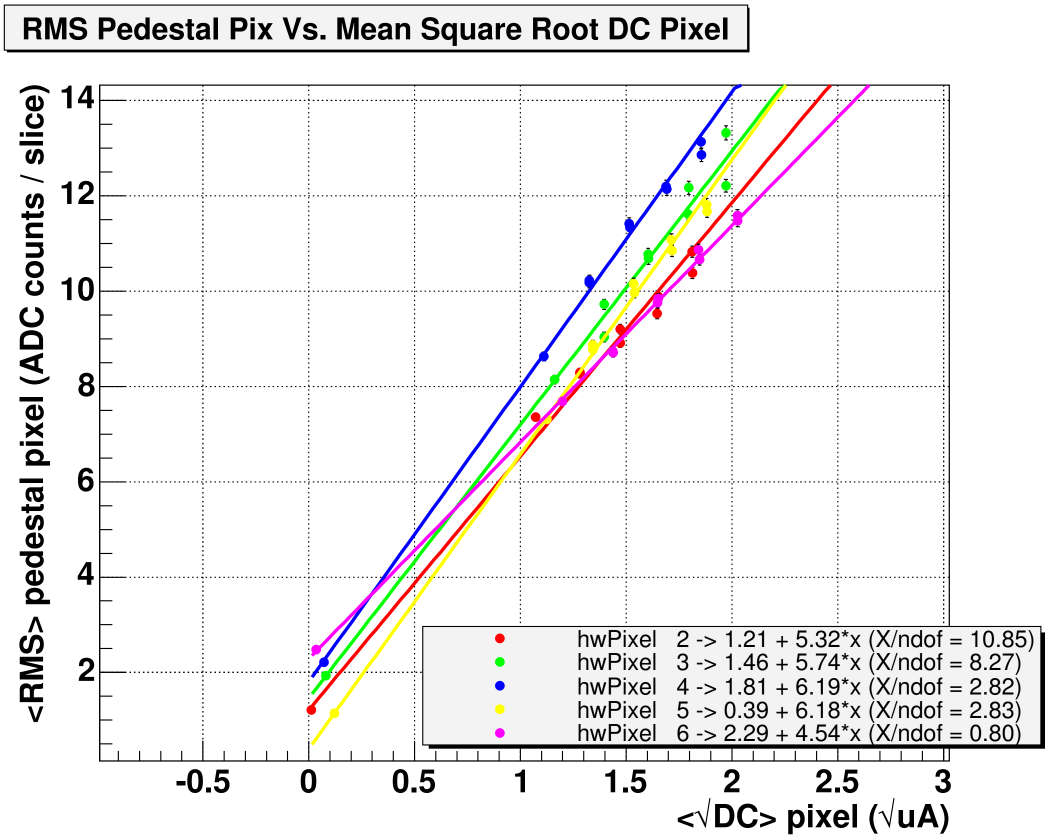

Figure 7.3: *Pedestal RMS vs DC for the first five pixels in the camera and the CL levels discussed in the text.*

factor square root of the pixel area. The pixels are flatfielded to provide the same charge (or DC), so a pixel with more photoelectrons shows a smaller pedestal RMS for the same DC or equivalently a smaller slope in figure 7.3. Outer pixels have a factor 2 smaller slope because their area is a factor 4 larger.

The relative sigma of the distribution of inner and outer slopes is approximately 10%. Since calculating the slope is equivalent to normalizing by the DC, that is, to removing the effect of different PMT QE and amplification gains, the dispersion of slope can only be due to a dispersion of gains in the optical transmission system.

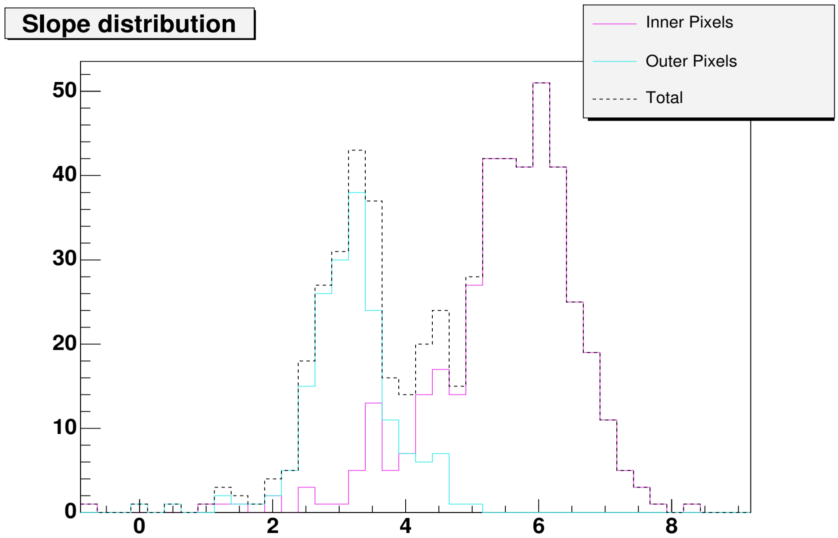

Figure 7.4: *Distribution of the slopes obtained in the fit to the curve pedestal RMS vs* $\sqrt{DC}$.

7.4 Dependence of DC on zenith angle and long term evolution

7.4.1 Sources of NSB

As we said above, the DC in a given pixel is directly proportional to the NSB and the starlight that is integrated in the pixel FOV. The starlight strongly depends on the galactic latitude and longitude, while the main sources of diffuse NSB[1, 4] are:

- **Air glow**: light emitted by atoms and molecules in the upper atmosphere (above 90 km height) which are excited by solar UV radiation during the day. For our wavelength range, the emitters are mostly O_2 and OH. Air glow increases with ZA following the so-called *van Rhijn function* (see [4] and discussion below). It strongly depends on the solar cycle: it increases by roughly a factor 2 during the solar maximum.

- **Zodiacal light**: in our wavelengths it is sunlight scattered by interplanetary dust. It is strongly dependent on the angular distance to the sun (by more than an order of magnitude) and the ecliptic latitude (it decreases a factor 2 from 0 to 60° latitude and then stays practically constant).

- **Scattered light**: this is light that scatters in the troposphere (below 12 km height). The primary source of light is in turn starlight, air glow or zodiacal light, so it is in general a secondary effect, but may make an important contribution for observatory sites close to inhabited areas (not the case at

La Palma) or in case the density of scattering particles is especially high (mist or Sahara dust during the summer).

7.4.2 Dependence on ZA

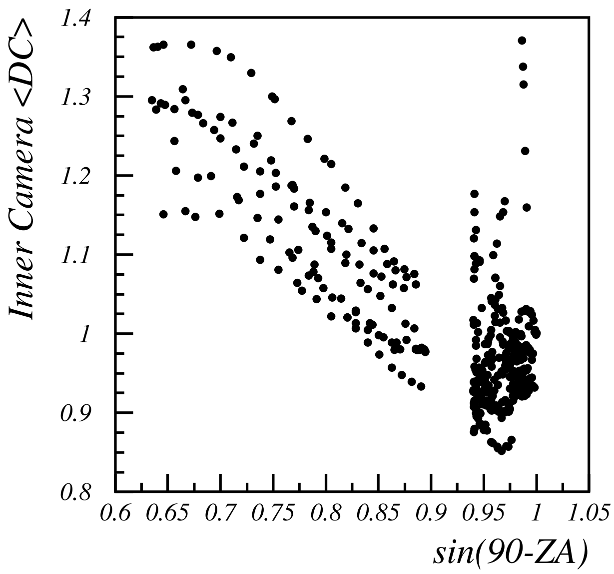

Figure 7.5: *Dependence of the mean DC in the inner camera on the zenith angle (in degrees) for different observation periods.*

The Crab data of January 2005 covers the whole range from 0 to 90° ZA. In figure 7.5, we have plotted <DC> as a function of sin(90-ZA) for this source and period. The data points follow distinct "trajectories". Each trajectory corresponds to a data taking night. We believe that the global shift between the different trajectories (up to 10%) can be attributed to changing atmospheric conditions.

We have plotted the data as a function of sin(90-ZA) because we have found that this is the simplest functional dependence (although <DC> seems to saturate at high ZA (above 70°). Starlight is attenuated in the atmosphere, so the increase of <DC> must arise from a different source. The dependence with ZA fits well with what is expected for air glow[4].

Air glow is expected to increase by almost a factor 3 from 0 to 70°. Since we observe an increase of 0.2 μA, we estimate that the air glow contribution at low ZA is $\sim$0.07 μA.

7.4.3 Long term evolution

For this study we have restricted ourselves to the data taken after the Summer 2004 access to complete the mirror and improve the PSF, so that the telescope is in its nominal condition.

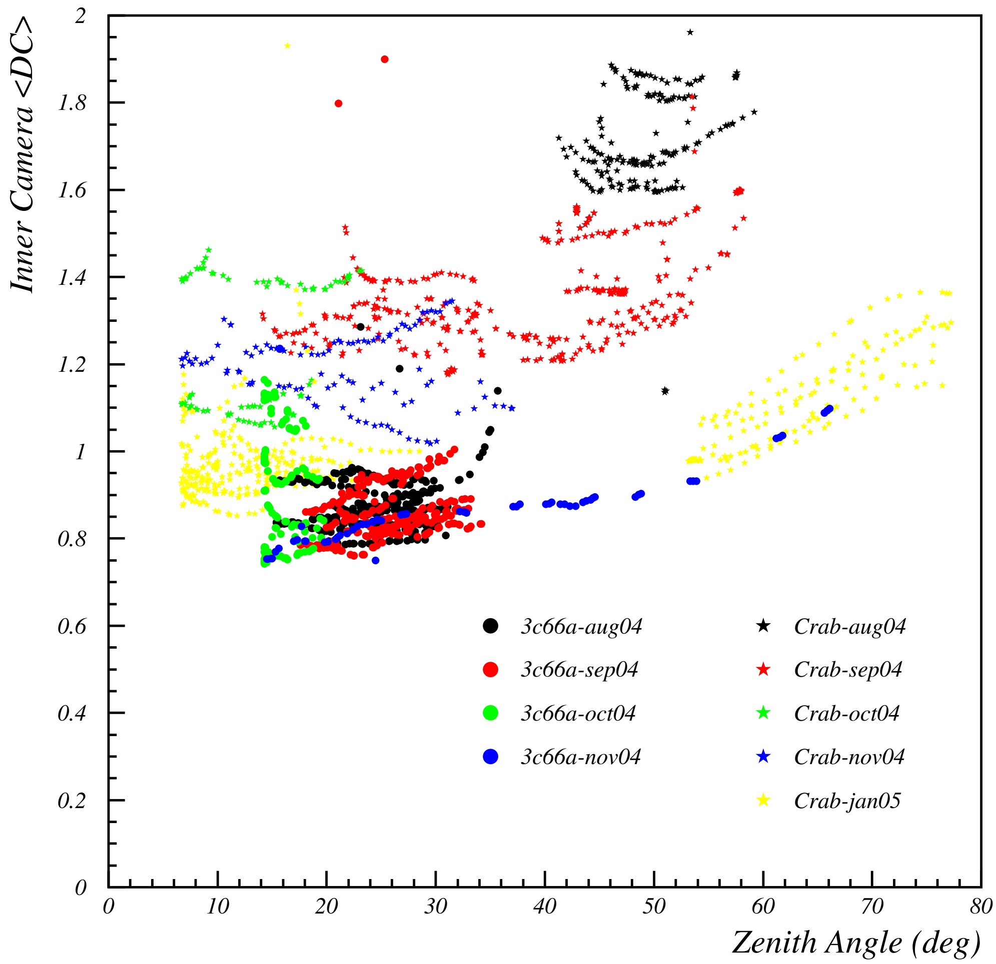

Figure 7.6: *Dependence of the mean DC in the inner camera on the zenith angle (in degrees) for different observation periods.*

Unfortunately only two sources have been observed for more than two months in a row: a galactic source, Crab Nebula, and an extragalactic source, 3c66a. Figure 7.6 shows the average DC in the inner camera as a function of the ZA for August-November 2004 and January 2005. Since the measurements were not made systematically, the data points are clustered in restricted ranges of ZA for each observation period and 3c66a is very much restricted to low ZA.

The increase of <DC> with ZA is consistently observed for all observation periods in figure 7.6. What is striking in this figure is that, while the DC stays practically constant for 3c66a, there are substantial global shifts from one period to another for Crab. For instance the DC shifts down from approximately 1.8 μA in August to 1.0 μA in January. This can hardly be attributed to changing atmospheric conditions or hardware changes since it does not happen for 3c66a.

Name	RA	DEC	ZA	lat_{eclip}	$dist_{sun}$	$long_{eclip}$	DC (μA)
ZL75eclt00	07:00:00	22:33:17	75°	0°	38°	38°	2.5
ZL75eclt10	06:39:05	32:49:49	75°	10°	34°	32°	2.3
ZL75eclt30	05:41:45	52:24:06	75°	30°	35°	18°	1.6
ZL75eclt60	03:14:34	72:13:53	75°	60°	50°	0°	1.3
ZL60eclt00	08:16:26	19:41:56	60°	0°	56°	56°	1.6
ZL60eclt10	07:52:43	31:34:08	60°	10°	49°	49°	1.6
ZL60eclt30	07:26:36	53:33:40	60°	30°	48°	38°	1.14
ZL60eclt60	07:18:57	81:24:00	60°	60°	63°	20°	0.96
ZL40eclt00	09:54:13	12:44:15	40°	0°	83°	83°	1.04
ZL40eclt10	09:33:00	25:28:22	40°	10°	72°	71°	1.02
ZL40eclt30	09:33:21	47:35:26	40°	30°	67°	60°	0.85
ZL40eclt60	12:58:21	69:08:21	40°	60°	82°	56°	0.68

Table 7.1: *Average DC in the inner camera for different positions in the sky in the night of 2005_05_29 around 21:30 UTC.* lat_{eclip} *and* $long_{eclip}$ *are the ecliptic latitude and longitude respectively.* $dist_{sun}$ *is the angular distance to the Sun.*

A possible explanation may be zodiacal light. Crab is in the ecliptical plane so it is particularly sensitive to this effect when it comes close to the Sun. The August data points were taken when Crab was only 60-70° away from the Sun, so the effect of zodical light was probably strong. The next observation periods were less affected: the angular distance was 85° in September, 120° in October, and more than 150° in November.

Conversely 3c66a is far from the ecliptical plane and is never affected by zodiacal light so there is no dependence on the observation period.

Unfortunately no other sources near the ecliptical plane have been observed at small angular distances to the Sun. The galactic center is analogous to Crab (it is at the crossing point of the galactic plane and the ecliptical plane) but was only observed more than 100° away from the Sun.

The increase in DC for Crab in August is substantial. For a fixed ZA the pedestal RMS increases in August as respect to January in the order of 35%, so it was worth to perform some additional test. This test was performed on 2005_05_29 and consisted on the observation of 12 sky positions at different ecliptic longitudes and latitudes (the sources can be found in the magic_test.edb catalogue).

The results of the test are summarized on table 7.1. Figure 7.7 shows the evolution of the mean DC in the inner camera with the galactic longitude for several ecliptic latitudes. There is an evident increase in the DC towards small ecliptic latitudes and longitudes. It must be noted however that the measured DC is the sum of zodiacal light and other sources of NSB, and we know that the remaining NSB depends on the zenith angle. The dependence on latitude and

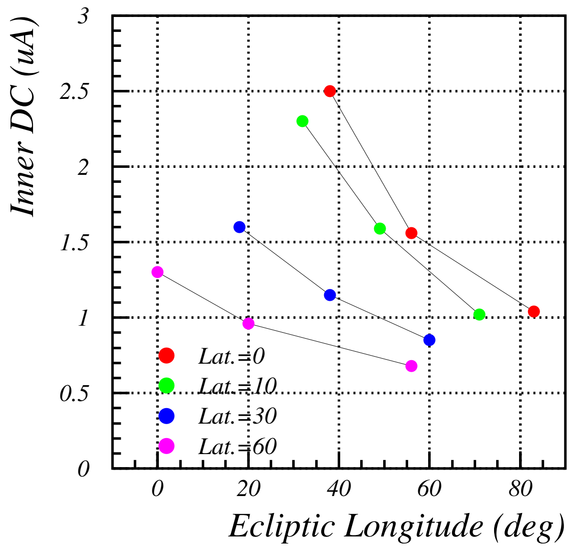

Figure 7.7: *Dependence of the mean DC in the inner camera on the ecliptic longitude for different ecliptic latitudes. The lines are only meant to guide the reader's eye. Mind that the DC is not only due to zodiacal light and the other sources of light depend on zenith angle and not on ecliptic latitude or longitude.*

longitude is compatible with the results of [4] and can explain the increase of DC for the Crab in August and September.

We can conclude that the contribution of zodiacal light is not negligible at all, but is restricted to small distances to the Sun and mostly in the ecliptic plane. Special attention must be paid never to schedule sources close to the ecliptic plane when they are less than 60° away from the Sun. This happens when scheduling these sources (at high zenith angle!) when they rise less than two hours before dawn and when they set less than two hours after sunset.

7.5 Moon observations

In this section we want to characterize the effect of moonlight on our telescope in terms of noise and discriminator thresholds. Moonlight increases the noise in the pixels and the rate of accidentals. For an accidental rate above 100 Hz, we are forced to increase the DT and hence the telescope trigger threshold. Estimating the DT that must be set for a given moon phase and position in the sky is instrumental to establish if the observation of a given source is feasible.

We have measured the average DC, the minimum DT we can set in the receivers with a sustainable accidental rate (DT$_{min}$, and the accidental rate for this DT$_{min}$ for different moon phases and angular distances to the moon. The results can be found in table 7.2. The data were obtained during observation period 25 (december 2004 - january 2005). The first set of measurements (four days after full moon) actually correspond to the second night when datataking was possible after full moon (second night of the observation period, in this particular case 2004_12_30), so the moon was still very bright. The last day corresponds to 3 days before new moon, when the moon is already very dim.

7.5.1 Dependence of DC on moon phase and angular distance

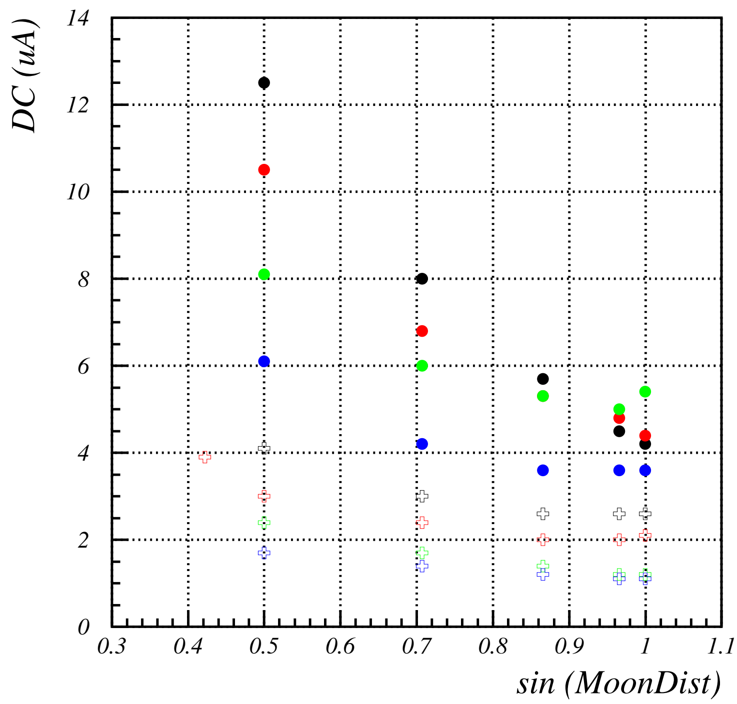

Figure 7.8: *Anode current as a function of the sine of the angular distance to the moon (in degrees) for different moon phases. From the highest to the lowest DC the points correspond to 4, 5, 7, 8, 9, 10, 11 and 12 days after full moon (mind the gap between 5 and 7 days.)*

Figure 7.8 shows the evolution of the DC with the angular distance to the moon. What is actually plotted in the horizontal axis is the sine of the angular distance because we found out that the DC depends almost linearly on this parameter.

Even for the first day under consideration the DC is always below 15 μA at an angular distance as short as 30°. When the telescope points perpendicular to the moon (sin(MoonDist) = 1 in the figure) the DC is always below 5 μA. The DC for the last day is not much higher than the NSB.

7.5.2 Dependence of DT on DC

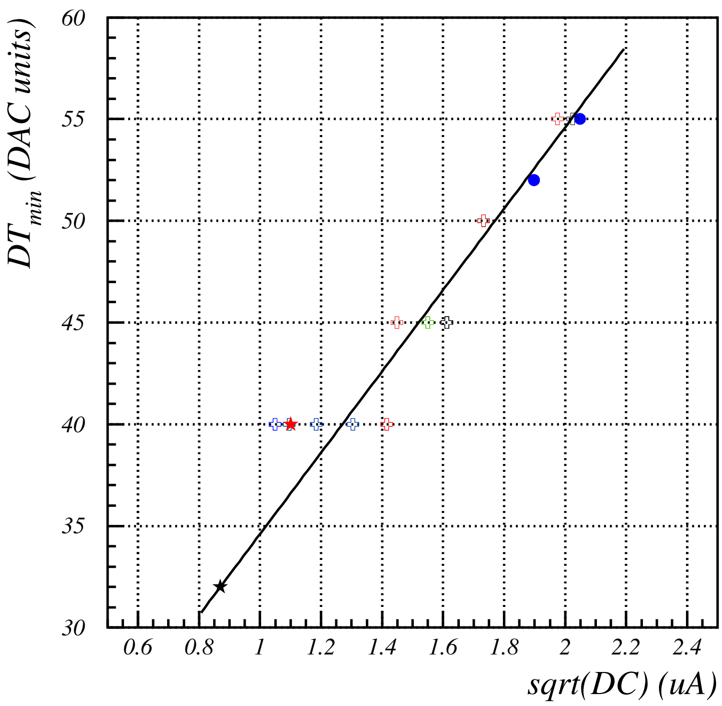

Figure 7.9: *DT_{min} as a function of the square root of DC for the days when the DT_{min} was measured. We have added a red star that corresponds to moonless Crab and a black star for a moonless extragalactic source. The black line is a rough fit to all the points (see text for fit parameters).*

For some days we also measured the DT_{min} that had to be set to limit the accidental rate below ~100 Hz. The dependence of this parameter on the square root of DC is displayed on figure 7.9. We have added two more points that correspond to the standard Crab and extragalactic observation conditions. DT_{min} is plotted versus $\sqrt{DC}$ because we expect it to scale with the pedestal RMS that in turn depends on $\sqrt{DC}$ (see above in this chapter). The points show indeed a roughly linear dependence. Note that the DTs are normally selected in steps of 5 to make the test shorter, so DT_{min} has an error of about 2-3 units. We have made a rough fit to the points and obtained the following law **that also holds valid for moonless observations**:

$$DT_{min}(DAC\ units) = 20 \cdot \sqrt{DC(\mu A)} + 14.6 \tag{7.3}$$

Unfortunately we do not have points for the first nights when the moon was brighter so there are no points for DC>5 μA. But we can use the law above to predict the DT_{min} that we must set for a given moon phase and angular distance to the moon. For the highest DC that we measured (12.5 μA for four days after full moon and 30° angular distance) we would have to set the DT to 85 DAC units. This is a factor $\sim$3 higher than our standard for extragalactic observations.

The telescope trigger threshold depends almost linearly on DT_{min}, so we can conclude that the trigger threshold will increase at most by a factor $\sim$3 when observing close to the moon in the second night of the observation period. Of course this only applies to the trigger threshold. We have not studied the effect of the increased noise in the determination of the shower parameters and our ability to discriminate gammas and hadrons. It may well be that the analysis threshold increases and that our sensitivity is worse for moon observations.

Phase (days)	θ_{moon} (°)	<I> (μA)	DT_{min}	$Rate_{acc}$ (Hz)
4	90	4.2	-	-
4	75	4.5	-	-
4	60	5.7	-	-
4	45	8.0	-	-
4	30	12.5	-	-
5	90	4.4	-	-
5	75	4.8	-	-
5	60	5.3	-	-
5	45	6.8	-	-
5	30	10.5	-	-
7	90	5.4	-	-
7	75	5.0	-	-
7	60	5.3	-	-
7	45	6.0	-	-
7	30	8.1	-	-
8	90	3.6	52	-
8	75	3.6	52	-
8	60	3.6	52	-
8	45	4.2	55	-
8	30	6.1	-	-
9	90	2.6	45	180
9	75	2.6	45	150
9	60	2.6	45	190
9	45	3.0	50	67
9	30	4.1	55	130
10	90	2.1	45	46
10	75	2.0	40	110
10	60	2.0	40	210
10	45	2.4	45	65
10	30	3.0	50	54
10	25	3.9	55	69
11	90	1.2	40	1.8
11	75	1.2	40	1.3
11	60	1.4	40	32
11	45	1.7	40	8.5
11	30	2.4	45	42
12	90	1.1	40	74
12	75	1.1	40	1.4
12	60	1.2	40	1.7
12	45	1.4	40	7.8
12	30	1.7	40	5.7

Table 7.2: *Phase of the moon (days after first day of full moon), angular distance to the moon θ_{moon}, mean camera DC, minimum DT that can be set DT_{min} and accidental rate $Rate_{acc}$. The DT_{min} and the accidental rate $Rate_{acc}$ were not measured for some of the moon phases.*

Bibliography

[1] C. R. Benn and S. L. Ellison, "La Palma night-sky brightness", 1998, La Palma Technical Note 115, Isaac Newton Group.

[2] Electron Tubes web page http://www.electrontubes.com/pmt/sensitivity.html and brochure "Understanding photomultipliers".

[3] F. Goebel, J. A. Coarasa, R. Stiehler and S. Volkov, proceedings 28th ICRC, Tsukuba, 2003, page 2939.

[4] Ch. Leinert et al., Astron. Astrophys. Suppl. Ser. **127** (1998) 1-99.

[5] B. K. Lubsandorzhiev, Y. E. Vyatchin, "Stability studies of nanosecond light sources based on blue ultra bright LEDs", physics/0403018

[6] M. Martínez, private communication.

[7] A. Moralejo, "Monte Carlo estimate of flux sensitivity of MAGIC for point-like sources", MAGIC-TDAS 04-04, 7 December 2004.

[8] A. Moralejo, private communication, January 2005.

[9] D. Paneque, et al., "A method to enhance the sensitivity of photomultipliers for Air Cherenkov Telescopes", Nuclear Instr. and Meth. A, in press.

[10] D. Paneque, PhD Thesis, Ludwig-Maximilian-Universität, Munich 2004.

[11] "Photomultiplier Tubes, Principles and Applications", Philips Photonics.

[12] A. Ostankov et al, "A study of the new hemispherical 6-dynode PMTs of Electron Tubes", Nuclear Instr. and Meth. A, **442** (2000) 117-123.